Department of Physics and Astronomy

University of Heidelberg

Diploma Thesis

in Physics

submitted by

Christopher Dietl

born in Tübingen

December 2012

Calibration and Setup of a Capacitance Dilatometer for Studies on CeFeAsO and $LiMn_{0.95}Ni_{0.05}PO_4$

This diploma thesis has been carried out by Christopher Dietl

at the

Kirchhoff-Institute for Physics

under the supervision of

Prof. Dr. Rüdiger Klingeler

Zusammenfassung

Kalibration und Aufbau eines Kapazitätsdilatometers für Messungen an CeFeAsO und $LiMn_{0.95}Ni_{0.05}PO_4$: Die vorliegende Arbeit befasst sich mit Aufbau und Kalibration eines hochauflösenden Kapazitätsdilatometers zur Messung der thermischen Ausdehnung. Eine Temperaturstabilität von 1 mK bei 5 K und 10 mK während des linearen Temperaturduchlaufs von 5 K bis 300 K konnte mit Hilfe eines Heliumgasfluss-kryostaten realisiert werden. Systematische Fehler werden im Detail analysiert. Kalibrationsmessungen zeigen eine Genaugikeit von $1 \cdot 10^{-5}$ in der relativen Längenänderung und $1 \cdot 10^{-7}\,\mathrm{K}^{-1}$ im thermischen Ausdehnungkoeffizienten α. Ein nicht reproduzierbarer Zelleffekt wurde festgestellt und analysiert. Die thermische Ausdehnung von einkristallinem $LiMn_{0.95}Ni_{0.05}PO_4$ wurde untersucht. Zwei positive Anomalien in der a- und c-Achse bei $T_\mathrm{N} = 32{,}5\,\mathrm{K}$ wurden in α festgestellt, die mit dem Einsetzen der antiferromagnetischen Ordnung verbunden sind, während die uniaxiale Druckabhängigkeit dT_N/db klein ist. Eine weitere Anomalie bei $T_\mathrm{tr} = 14{,}7(5)\,\mathrm{K}$ wurde beobachtet. Messungen an $CeFeAsF_xO_{1-x}$ zeigen die Dotierungsabhängigkeiten des strukturellen und magnetischen Phasenübergangs in dieser Substanzklasse. Die Übergangstemperaturen für die undotierte Muttersubstanz betragen für den strukturellen Phasenübergang $T_\mathrm{S} = 151{,}4{+}1{-}0{,}5\,\mathrm{K}$ und für den magnetischen Übergang $T_\mathrm{N} = 137{,}0(5)\,\mathrm{K}$. Für $x = 0{,}05$ wurde $T_\mathrm{S} = 121{,}7(5)\,\mathrm{K}$ bestimmt, während die Anomalie in der thermischen Ausdehnung bei $x = 0{,}04$ nicht beobachtbar ist.

Abstract

Calibration and Setup of a Capacitance Dilatometer for Studies on CeFeAsO and $LiMn_{0.95}Ni_{0.05}PO_4$: This thesis describes the setup and calibration of an experiment to measure thermal expansion using a high-resolution capacitive dilatometer. A temperature stability of 1 mK at 5 K and 10 mK during a linear temperature sweep from 5 K to 300 K was achieved using a helium gas-flow cryostat. Systematic errors are discussed in detail. Calibration measurements show an accuracy of 1×10^{-5} in relative length change and $1 \times 10^{-7}\,\mathrm{K}^{-1}$ in the thermal expansion coefficient α. A non-reproducible cell effect was noticed and investigated. Thermal expansion measurements of single-crystalline $LiMn_{0.95}Ni_{0.05}PO_4$ were performed. The thermal expansion coefficient exhibited two positive anomalies at $T_\mathrm{N} = 32.5\,\mathrm{K}$ in the a- and c-axis, which are linked to antiferromagnetic ordering. An additional feature was noticed at $T_\mathrm{tr} = 14.7(5)\,\mathrm{K}$. Measurements of the thermal expansion of $CeFeAsF_xO_{1-x}$ show the influence of doping on the structural and magnetic phase transitions. For the undoped parent compound ($x = 0$), the temperature of the structural transition was determined to be $T_\mathrm{S} = 151.4{+}1{-}0.5\,\mathrm{K}$ and for the magnetic transition $T_\mathrm{N} = 137.0(5)\,\mathrm{K}$. An analysis for $x = 0.02$ yielded $T_\mathrm{S} = 121.7(5)\,\mathrm{K}$, whereas no anomalies of the thermal expansion coefficient were found for $x = 0.04$.

Online version with corrections of minor mishaps
March 2013

Contents

1 Introduction

The phenomenon of thermal expansion has always been a companion of scientific endeavor. Long before the mathematical description via thermodynamics and statistical mechanics was developed, it has been noticed that substances expand during heat input. Galileo Galilei (1564-1642) constructed an apparatus to measure heat based on the expansion of air. Scientific progress ultimately led to the development of thermometers based on the thermal expansion of liquids. The first mercury-in-glass thermometer by G.B. Fahrenheit allowed measuring temperatures with an unprecedented resolution creating an impetus for quantitative thermal sciences. Exhibiting effects orders of magnitude less, it was not until 1719 that the thermal expansion of a solid was discovered. W. J. Gravesande described his observation that a heated brass sphere could not passage a ring which it could passage easily before heating–an experiment, which survived to today's physics introductory courses. The construction of pendulum clocks stimulated systematic, quantitative research on thermal expansion, since the expansion of the pendulum led to imprecision of the clock. The first mechanical dilatometers emerged to quantify the phenomenon. At the end of the 19th and the beginning of the 20th century the transition from a purely phenomenological description of thermodynamics to a comprehensive well-founded theory was under way. Statistical mechanics provided now tools to link thermoelastic effects to microscopic properties of a solid. Mie and Grüneisen [1, 2, 3] developed the theoretical framework reasoning that thermal expansion is the result of a volume dependence of the atomic vibrational eigenmodes or, put differently, of the anharmonicity of the interatomic potential. Grüneisen's work culminated in the finding that the ratio of the thermal expansion coefficient to the specific heat forms a constant, the so called Grüneisen-parameter.

To measure thermal expansion an abundance of techniques has been developed. Using interferometric methods it was now possible to detect length changes in the order of the wavelength of light. However, the measurement of the thermal expansion coefficient α at low temperatures still posed a problem. Since α constitutes the derivative of the relative length change, high resolutions are needed in order to yield a good accuracy at low temperatures where materials expand the least. As a remedy the use of a capacitor to measure length changes was employed. The first published use of a capacitive dilatometer was by Prytherch in 1932 [4]. However, only the combination with the three-terminal

method suggested by Thompson [5] allowed White to measure relative length changes in metals with a resolution of 1×10^{-9} [6] and thus to obtain α for the first time down to liquid helium temperatures (4.2 K).

Statistical mechanics reveals that the thermal expansion coefficient α resembles the pressure dependence of the entropy $(\partial S/\partial p)_T$. Thus, α represents a thermodynamical response function for every pressure-dependent entropy change. In a nutshell, interactions within materials are caused by the overlap of electronic wavefunctions. Depending on its compressibility, the interatomic distance in a crystal and thus the overlap can be changed by applying pressure. Order phenomena occur at the brink to a new interaction scale and can therefore be sensitive to pressure. Since an ordering is closely connected to the entropy, α resembles a probe for such phenomena making capacitive dilatometry with its high sensitivity a tool of choice to investigate phase transitions.

The aim of this work is the setup of an experiment to measure the thermal expansion in the temperature range 5 K to 300 K via means of capacitive dilatometry. During this process, two materials were analyzed, which are currently in the focus of research: Firstly, single-crystalline $LiMn_{0.95}Ni_{0.05}PO_4$ from the family of olivine lithium-phosphates which emerge as the next-generation battery material and show intriguing magnetic effects such as a strong magnetoelectrical effect and ferrotoroidal domain ordering. Secondly, fluorine-doped CeFeAsO, an iron-based superconductor, a new class of superconductors found in 2008.

The work is structured as follows:

In chapter 2, the theoretical background based on thermodynamics and statistical mechanics is laid out. An introduction to magnetoelastic coupling is given and the knowledge of phase transitions and their implication on α is refreshed.

The experimental method and devices used within the setup are presented in detail in chapter 3. An emphasis is given on the propagation of uncertainties arising from each device to the resulting measurand, the relative length change.

Chapter 4 discusses the influence of systematic errors and effects noticed during measuring which limit the accuracy of the device. An evaluation of the magnitude of each error is presented and underlying processes are displayed.

The results of calibration measurements are summarized in chapter 5. A comparison with well-known reference materials is presented in order to prove the accuracy and the high resolution of the device.

The following chapters 6 and 7 present thermal expansion studies of $LiMn_{0.95}, Ni_{0.05}PO_4$ and $CeFeAsO_{1-x}F_x$ in terms of thermal expansion. Armed with the tools given in chapter 2, the phase transitions occurring in both materials are analyzed.

Chapter 8 concludes by summarizing the findings of this work and presents an outlook.

2 Theory

2.1 Thermodynamic Potentials

The most important insight of thermodynamics consists in the fact that the behavior of a system can be described by a few macroscopic variables such as energy, entropy etc. Together with statistical mechanics, it makes an elegant tool to investigate material properties. To underline its power, it is often compared with the ab-initio approach, i.e. solving 10^{19} to 10^{23} coupled Schrödinger equations, which would be a gigantic task requiring enormous computational power. The finding of thermodynamics related to this work are summarized in this chapter. The definition of the internal energy E and entropy S form the first and second law of thermodynamics

$$dE = \delta Q + \delta W = TdS - PdV \tag{2.1}$$

$$dS = \frac{\delta Q}{T} \geq 0. \tag{2.2}$$

This means a change in E can be divided in a change in heat in- or output δQ and work δW done by or on the system. Eq. 2.2 defines δQ as the energy that is used to increase the entropy. They are so called state functions, i.e. functions which are fully determined by the current state of the system and do not depend on the path leading to its state. The notation δ denotes that there is no integral of Q and W which is is a state function. This is also called inexact derivative.

For practical reasons, it is often useful to use different combinations of these quantities[1]:

$$\begin{array}{lll} \text{Free Energy} & F = E - TS & dF = -SdT - PdV + \mu dN \\ \text{Enthalpy} & H = E + PV & dH = \ \ TdS + VdP + \mu dN \\ \text{Gibbs Potential} & G = E - TS + PV & dG = -SdT + VdP + \mu dN \end{array} \tag{2.3}$$

The quantities above are called thermodynamic potentials since they have a similar function like other potentials in physics, e.g. gravitational potential or electromagnetic potential. State variables like V, P etc. can be conveniently obtained by simply deriving these

[1] It is, for example, easier to measure an isobaric enthalpy change, since $(dH)_p = \delta Q$.

quantities. In this work, equations are regularly simplified by assuming that there is no particle exchange, i.e. $dN = 0$. If one of these variables is of interest, they are explicitly introduced.

2.2 Response Functions

Response functions are thermodynamic variables which describe how the system responses to an external pertubation. They correspond to the second derivates of potentials which makes them suitable to analyze phase transitions (see section 2.5). The heat capacity for constant pressure is the most encountered one:

$$c_p = \left(\frac{\delta Q}{dT}\right)_P = T\left(\frac{\partial S}{\partial T}\right)_P - T\left(\frac{\partial^2 G}{\partial T^2}\right)_P \tag{2.4}$$

It describes the change in temperature during a heat input. The specific heat can also be defined for a constant volume as c_V, but it is literally impossible to measure and the difference to c_p is often negligible [7]. The term expressing the response of the volume to a pressure stimulus is called the compressibility:

$$\kappa_T = -\frac{1}{V}\left(\frac{\partial V}{\partial P}\right)_T = -\frac{1}{V}\left(\frac{\partial^2 G}{\partial P^2}\right)_T \tag{2.5}$$

Essential for this work is the volumetric thermal expansion coefficient

$$\beta(T) = \frac{1}{V}\left(\frac{\partial V}{\partial T}\right)_P = -\frac{1}{V}\left(\frac{\partial S}{\partial P}\right)_T = \frac{1}{V}\frac{\partial}{\partial P}\left(\left(\frac{\partial G}{\partial T}\right)_P\right)_T. \tag{2.6}$$

The corresponding quantity for changes in one direction is the linear thermal expansion coefficient:

$$\alpha(T) = \frac{1}{L}\left(\frac{\partial L}{\partial T}\right)_P, \tag{2.7}$$

where L is the measured length. This is the variable measured in this experiment to probe the thermodynamic behavior of the system. If the expansion is isotropic, β can be written as

$$\beta = 3\alpha \tag{2.8}$$

2.3 Thermal Expansion

Commonly, an introduction into lattice vibrations starts with a harmonic model such as the 1D-chains of atoms sitting in a potential well which is quadratically proportional to the distance of the ions. However a simple gedankenexperiment shows that thermal expansion cannot occur in such a system: An ion within a harmonic potential does not change its

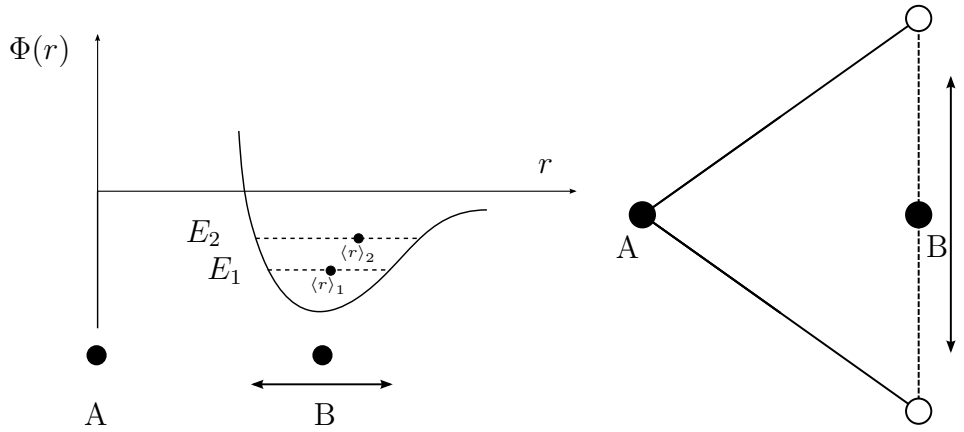

Figure 2.1: From [8]. Left: Ions in an anharmonic potential. The mean distance increases with increasing amplitude of B thus leading to a positive thermal expansion. Right: Tension mechanism leading to negative thermal expansion. A larger amplitude of B's transverse vibration results in a mean attraction.

mean position when increasing or decreasing the energy, since the potential is symmetric. An anharmonic potentials however can intuitively explain a higher mean distance with increased thermal energy of the ions. Negative thermal expansion (=contraction) is also observed in some materials such as silicon [9]. This can be explained by transverse vibrations. Fig. 2.1 shows a basic picture of the two main processes leading to positive and negative thermal expansion.

In the next section, a mathematical criterion for when thermal expansion occurs will be derived . The derivations follows mainly [10] which is highly recommended for further details. One starts by basically expanding the linear chain model to a 3D Bravais crystal (one single atom per unit cell). Its total free energy F can be written as [11]:

$$F = F_{eq}(V) + \sum_k \left[\frac{\hbar\omega_k}{2} + kT \log\left(1 - \mathrm{e}^{-\hbar\omega_k/kT}\right) \right], \tag{2.9}$$

where $k = (\mathbf{k}, \lambda)$ is a variable denoting the wave number vector $\mathbf{k}$ and phonon branch λ, so the sum goes over all possible phonon states. F_{eq} represents the free energy of the equilibrium configuration of the ions. The following terms are the ground-state energy $\hbar\omega_k/2$ and the excited energy levels following a Bose-Einstein distribution, since phonons can be treated as bosons. The pressure can be obtained via deriving with respect to the volume V (eq. 2.3):

$$P = -\left(\frac{\partial F}{\partial V}\right)_T = -\frac{\partial F_{eq}}{\partial V} - \sum_k \hbar\omega_k \left(\frac{1}{2} + \frac{1}{\mathrm{e}^{\hbar\omega_k/kT} - 1}\right) \frac{\partial \log \omega_k}{\partial V} \tag{2.10}$$

The term $\partial \log \omega_k / V$ can be written as

$$\frac{\partial \log \omega_k}{\partial V} = \frac{1}{V} \frac{\partial \log \omega_k}{\partial \log V} = -\gamma_k \frac{1}{V}, \tag{2.11}$$

where γ_k is called Grüneisen parameter. It quantifies the normal mode frequency behavior of phonons under volume change. Using the relation

$$\left(\frac{\partial V}{\partial T}\right)_P = -\left(\frac{\partial P}{\partial T}\right)_V \left(\frac{\partial V}{\partial P}\right)_T \tag{2.12}$$

one can write

$$\alpha(T) = \frac{1}{3}\frac{1}{V}\left(\frac{\partial V}{\partial T}\right)_P = -\frac{1}{3}\kappa_T \left(\frac{\partial P}{\partial T}\right)_V = -\frac{1}{3}\kappa_T \sum_k \gamma_k \frac{\partial}{\partial T}\frac{\hbar\omega_k}{V}\left(\frac{1}{\mathrm{e}^{\frac{\hbar\omega_k}{kT}} - 1}\right). \tag{2.13}$$

The term within the sum can be identified as the phononic specific heat

$$c_V = \sum_k \gamma_k \frac{\partial}{\partial T}\frac{\hbar\omega_k}{V}\left(\frac{1}{\mathrm{e}^{\frac{\hbar\omega_k}{kT}} - 1}\right), \tag{2.14}$$

the total change in phononic energy with temperature. With the definition of an overall weighted Grüneisen coefficient,

$$\gamma = \frac{\sum_k \gamma_k c_V(\omega_k, T)}{\sum_k c_V(\omega_k, T)} \tag{2.15}$$

one arrives at a concise expression for the linear thermal expansion coefficient:

$$\alpha = \frac{1}{3} c_V \gamma \kappa_T \tag{2.16}$$

In general, γ is temperature-dependent. If one defines a Debye-Temperature Θ_D as the energy scale of phonons, it follows from eq. 2.15, however, that γ becomes constant for $T \to 0$ and $T \gg \Theta_D$, since $c_V(\omega_k) \to const$ for both cases. Experiments show that κ_T is only weakly dependent on temperature [10]. Thus one can infer that α converges to a constant at $T \gg \Theta_D$. Based on Nernst's theorem, α is zero for $T = 0$ [11].

If one assumes a Debye-model, all $\omega_k \propto \omega_D$, every γ_k is equal and thus γ temperature independent. So within this approximation α follows c_V in temperature, thus alltogether:

$$\begin{aligned} &\alpha = 0 && T = 0 \\ &\alpha \propto T^3 && T \to 0 \\ &\alpha \propto const && T \gg \Theta_D. \end{aligned} \tag{2.17}$$

This gives a correct description for simple insulators [12].

Eq. 2.11 shows that thermal expansion only occurs if the phononic normal mode frequencies change during a change of the equilibrium volume. The Grüneisen coefficient is thus a quantity measuring the anharmonicity of a crystal lattice. The statement from the beginning that harmonic crystal do not show thermal expansion can now be understood

from a mathematical point of view. For example, the dispersion relation for a harmonic 1D-linear chain model with a lattice constant a is

$$\omega(k) = 2\sqrt{\frac{K}{M}}\left|\sin\frac{1}{2}ka\right|, \tag{2.18}$$

where K is the spring constant quantifying the coupling between atoms and $k = \frac{2\pi}{a}\frac{n}{N}$ is defined via the periodic boundary condition. $\omega(k)$ is independent of $L = Na$ and thus no thermal expansion occurs.

Since it was started with a harmonic approximation, but the results are applied to anharmonic crystals as well, this approximation is also called quasiharmonic approximation.

The free electron gas in metals has an additional pressure contribution in (eq. 2.10) resulting in an additional specific heat term. Taking it into account leads to [10]

$$\alpha = \frac{1}{3}\kappa_T\left(\gamma c_V + \frac{2}{3}c_{el}\right) \tag{2.19}$$

For simple metals this adds a linear term in α for low temperature, since $c_{el} \propto T$. This theoretical prediction is also proven by experiments [13].

The Grüneisen coefficient can be used to investigate the pressure dependence of the dominant energy scale. First, one starts by assuming that the entropy has the form

$$S(T) = f\left(\frac{T}{T^\star}\right), \tag{2.20}$$

where $T^\star$ is the dominating energy scale in a given temperature regime, e.g. the Debye temperature in a purely phononic system. Using the definitions of β and c_p one can deduce the following ratio [14, 15][2]:

$$\gamma = \frac{V\beta}{\kappa_T c_V} = \frac{V\beta}{\kappa_S c_p} = \frac{1}{\kappa_T}\frac{\partial \ln T^\star}{\partial P} \tag{2.21}$$

If there is a dominating energy scale present, γ is then temperature-independent and quantifying the pressure dependence of $T^\star$.

2.4 Magnetostriction and Magnetoelastic Coupling

Ferromagnetic materials change their dimensions within a magnetic field H. This phenomenon is called Magnetostriction. Similar to the thermal expansion coefficient α, this

[2]There seems to be no agreement on whether to include the compressibility in the ratio. However, $\kappa_S \approx$ const and $\kappa_T \approx$ const [10]

volume change can be quantified as

$$\lambda = \frac{1}{V}\left(\frac{\partial V}{\partial H}\right)_{T,p}. \tag{2.22}$$

From a thermodynamical standpoint, the effect can be explained by adding the magnetic energy contribution to the internal energy (eq. 2.3) yielding

$$dE = TdS - pdV + V\vec{B}d\vec{M}, \tag{2.23}$$

where B represents the external magnetic field and M the magnetization. Using Maxwell relations one can obtain λ via

$$\lambda = -\left(\frac{\partial M}{\partial p}\right)_{H,T}. \tag{2.24}$$

This shows, that magnetostriction reflects the pressure dependence of the magnetization. If a solid is compressed, the lattice is distorted. Electrons are coupled to the orbital momentum via spin-orbit-coupling, which in turn couples them to the lattice ions. The magnetic interactions are based on the overlap of electronic orbitals, which is influenced by pressure through these couplings, which explains one basic mechanism which leads to a pressure dependence of the magnetization. The inverse effect is also true: Magnetization changes prompt elastic effects within a crystal, which is called magnetoelastic coupling. This explains why magnetic effects can also be seen in the thermal expansion coefficient.

Magnetostriction does not only occur in ferro- or antiferromagnets, but also in diamagnets [16] and paramagnets [17]. However, since their susceptibility is orders of magnitude smaller, the magnetostriction $\Delta l/l$ lies usually in the range 1×10^{-8} to 1×10^{-6}. One interesting phenomenon is the oscillatory magnetostriction in these compounds. This can be explained by the De Haas-van Alphen effect, which is the oscillatory behavior of the magnetization of a free electron gas within a magnetic field. This effect became a powerful tool to investigate Fermi surfaces, since the periodicity in $1/B$ can be related to the extremal cross-sections of the fermi surface in the direction of the B-field via [18]

$$\Delta\left(\frac{1}{B}\right) = \frac{2\pi e}{\hbar c S}, \tag{2.25}$$

where the surface of the cross-section of the fermi surface in momentum space is denoted by S. Rotating a single crystal within a magnetic field, it is then possible to construct a fermi surface based an the values of S.

2.5 Phase Transitions

A thermodynamic phase is defined as a homogeneous domain of a macroscopic system, which is in equilibrium [19, 20]. Different Phases are characterized by different macroscopic

quantities as for example magnetization (e.g. para-, ferro- or antiferromagnet), crystal structure (e.g. bcc or fcc) or electrial conductivity (e.g. insulator, metal, superconductor). By altering variables such as temperature, pressure and magnetic field H a transition from one phase to another can be triggered. Common everyday observations are, for example, the transitions between gas, fluid and solid for water. Research within the last century found additional "super" states of matter namely superconductivity and superfluidity. Even in cosmology phase transitions play a crucial part as there might have been a different vacuum phase in the early universe. All these transitions have in common that they can be described as a discontinuous or continuous transition. This classification was first postulated by Ehrenfest in 1933 [21]. According to his scheme, a phase transition is named a "phase transition of n-th order" if the first $(n-1)$ partial derivates of G

$$\left(\frac{\partial^n G}{\partial x^n}\right)_y \tag{2.26}$$

in its natural variables x are continuous, whereas at least one of the n-th order derivates shows a discontinuity at the phase boundary. Based on the behavior of S, first-order transitions are also called discontinuous and second-order transitions continuous. Higher-order transitions (third etc.) are usually bunched together with second-order transitions.

However, the Ehrenfest classification scheme received criticism since it cannot describe some second-order transitions correctly (see section 2.5.2). Since at least its nomenclature is still widely used, the terms "discontinuous" and "first-order phase transition" and "continuous" and "second-order phase transitions" are used interchangeably in this work.

Phase transitions are often associated with the phenomenon of symmetry breaking. A ferromagnet is a typical example: Once ordered, it loses its rotational symmetry. Different symmetries always belong to different phases. However, the contrary, is not true. The gas-to-liquid transition of water, for example, involves no reduction in symmetry [22].

2.5.1 Discontinuous Phase Transitions

Discontinuous phase transitions show a continuous G having a kink at the phase boundary and thus having a sudden change in its first derivates, e.g. V or S. The jump in S yields a so called latent heat $\Delta Q = T_C \Delta S$, an energy which is either required or released when driving a phase transformation (see fig. 2.2).

A characteristic phenomenon of first-order phase transitions is metastability: E.g. a phase can be prevented from undergoing a thermal transition, although it is below the critical temperature T_C. This can be explained by an energy penalty for the system by creating a surface between the two phases, thus making it unfavorable for the material to transform to another phase until a certain extent in temperature or pressure.

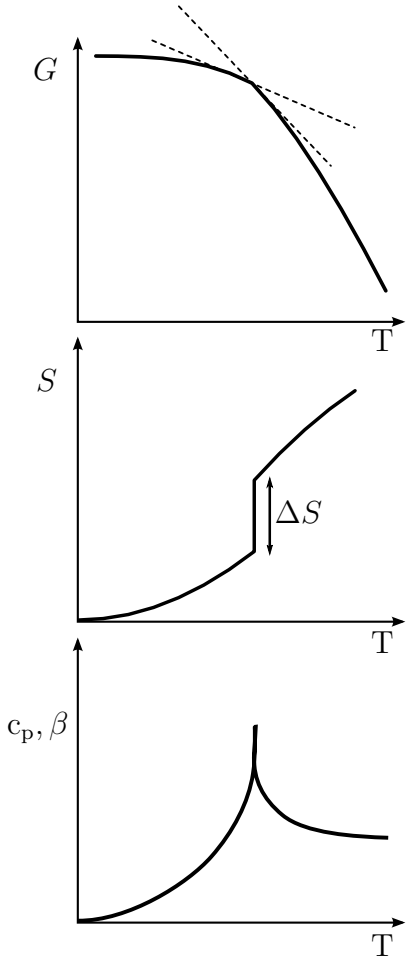

Figure 2.2: Gibbs potential G, entropy $S = -(\partial G/\partial T)_P$ and $c_p = T(\partial S/\partial T)_P$ or thermal expansion $\beta = 1/V(\partial S/\partial p)_T$ during a first-order phase transition. The dashed lines within the plot showing G represent the supercooled or superheated metastable phases.

However, such a supercooling or superheating only works usually in very clean materials, since impurities create nucleation sites and new boundaries which reduce the necessary surface tension. Sethna [23] gives a more detailed view on this process. Examples for first-order phase transitions are phase changes of water or the magnetically induced superconducting phase transition. Remarkably, metastable phase are also observed in the latter [20].

Clausius-Clapeyron-Equation

At the phase boundary, both phases are in equilibrium, which means that there is no heat, no volume and no particle exchange on average, i.e.

$$T_\alpha = T_\beta \quad P_\beta = P_\alpha \quad \mu_\alpha = \mu_\beta \tag{2.27}$$

Following the derivation from [11], both sides of $\mu_\alpha = \mu_\beta$ are derived with respect to T yielding

$$\left(\frac{\partial \mu_\alpha}{\partial T}\right)_P + \left(\frac{\partial \mu_\alpha}{\partial P}\right)_T \frac{dP}{dT} = \left(\frac{\partial \mu_\beta}{\partial T}\right)_P + \left(\frac{\partial \mu_\beta}{\partial P}\right)_T \frac{dP}{dT} \tag{2.28}$$

Using the Gibbs-Duhem-relation $G = \mu N$ and the differential dG (eq. 2.3) one arrives at

$$\frac{dP_V}{dT} = \frac{\Delta S}{\Delta V} \qquad \text{or conversely} \qquad \frac{dT_c}{dP} = \frac{\Delta V}{\Delta S}, \tag{2.29}$$

where $\Delta S = S_\alpha - S_\beta$ and $\Delta V = V_\alpha - V_\beta$. This is the so-called Clausius-Clapeyron-Equation. It relates the pressure dependence of the vapor pressure P_V or the temperature dependence of the critical temperature T_C with the ratio of the latent heat ΔS and the volume change ΔV.

2.5.2 Continuous Phase Transitions

In the Ehrenfest classification, a second-order phase transition consequently follows the logic of the first-order kind: While G is smooth and continuous, one of its first derivates (e.g. V, S or M) shows a kink and thus its derivative (e.g. c_p) a jump. However, this behavior is not realized in all transitions which involve a continuous first derivative of G (see fig. 2.3).

While the Ehrenfest classification holds perfectly, for example, in a thermal normal-superconducting transition, the lambda-transition of liquid He_4 shows a logarithmic singularity instead of a jump thus rendering the classification not correct or at least not complete [24]. Thus one treats all non-first-order transitions as second-order transitions or continuous phase transitions.

Ehrenfest-Equation

It is also possible to derive an equivalent of (eq. 2.29) for second order phase transitions, obtaining a relation for the pressure dependence of the critical temperature T_C. The following holds for second order transitions:

$$S_\alpha(T,p) = S_\beta(T,p) \qquad V_\alpha(T,p) = V_\beta(T,p) \tag{2.30}$$

$$dS_\alpha = dS_\beta \qquad dV_\alpha = dV_\beta \tag{2.31}$$

One can write dS and dV as a sum of the differentials of p and T

$$dS = \left(\frac{\partial S}{\partial T}\right)_p \mathrm{d}T + \left(\frac{\partial S}{\partial p}\right)_T \mathrm{d}p \tag{2.32}$$

$$dV = \left(\frac{\partial V}{\partial T}\right)_p \mathrm{d}T + \left(\frac{\partial V}{\partial p}\right)_T \mathrm{d}p \tag{2.33}$$

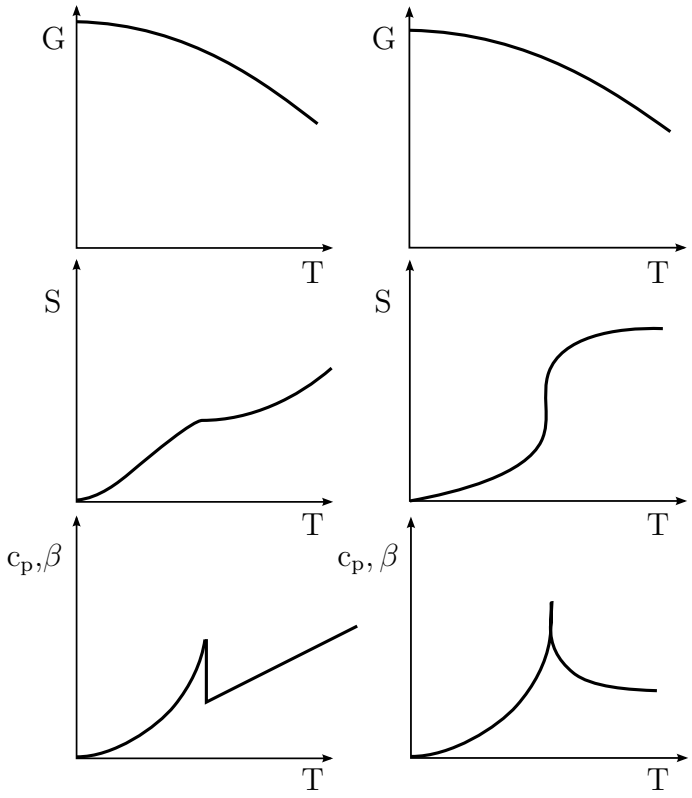

Figure 2.3: Gibbs potential G, entropy $S = -(\partial G/\partial T)_P$ and heat capacity $c_p = 1/T(\partial S/\partial T)$ or thermal expansion $\beta = 1/V(\partial S/\partial p)_T$ for two different cases of a continuous phase transition. The figures on the left correspond to a superconducting-normal conducting transition, a classical Ehrenfest transition, whereas the figures on the left correspond to a transition similar to the lambda-transition in He_4.

and with the help of Maxwell-relations one yields [25]

$$\frac{dT_C}{dp} = TV\frac{\beta^\alpha - \beta^\beta}{c_p^\alpha - c_p^\beta}, \tag{2.34}$$

which is called the Ehrenfest-Equation. Together with the knowledge of the jump in specific heat Δc_p, it is then possible to make predictions about the pressure dependence of T_C. This finding is regularly used for the superconducting transition as in [26].

3 Experimental Methods and Devices

3.1 Thermal Expansion Measurement Techniques

The thermal expansion α is experimentally accessed by measuring the length changes [8]

$$\Delta l/l = \frac{l(T) - l(T_0)}{l(T_{RT})} \tag{3.1}$$

relative to length at the starting temperature of the experiment T_0 divided by the length at room-temperature T_{RT}. This quantity is then numerically differentiated with respect to T to obtain α. This leads to a thermal expansion coefficient different to the one defined in eq. 2.7

$$\alpha(T) = \alpha_{\mathrm{theory}} \left(1 + \frac{l(T) - l_{\mathrm{RT}}}{l_{\mathrm{RT}}}\right), \tag{3.2}$$

however, the length changes during the experiments conducted in this work are of the order of 1×10^{-3} and thus the error is in the permille range and negligible. The relative length change can be approximated by

$$\frac{\Delta l}{l} \approx \left(\frac{\partial}{\partial T}\frac{\Delta l}{l}\right)\Delta T + \frac{1}{2}\left(\frac{\partial^2}{\partial T^2}\frac{\Delta l}{l}\right)\Delta T^2 = \alpha \Delta T + \left(\frac{\partial}{\partial T}\alpha\right)\Delta T^2. \tag{3.3}$$

Thus, if one defines the experimental thermal expansion coefficient as $\alpha^\star = 1/\Delta T(\Delta l/l)$, the relative error caused by finite temperature step in α is then

$$\frac{\alpha^\star - \alpha}{\alpha} = (\frac{1}{2}\frac{\partial \alpha}{\partial T}\Delta T)/\alpha \tag{3.4}$$

If α is approximated by polynomials, this yields in first order

$$\frac{\alpha^\star - \alpha}{\alpha} \approx \frac{\Delta T}{T} \tag{3.5}$$

If an accuracy of 1 % is desired, at least 100 mK steps are then required at low temperatures ($T \approx 10\,\mathrm{K}$). Since α is typically in the range of $1 \times 10^{-8}\,\mathrm{K}^{-1}$ at these temperatures, a resolution of 1×10^{-9} in $\Delta l/l$ is then needed. At lower temperatures, this resolution is already required just to resolve a length change ($\alpha(5\,\mathrm{K}) \approx 1 \times 10^{-9}\,\mathrm{K}^{-1}$). With a sample

	Technique	Resolution in $\Delta l/l$	Source
Microscopic	X-Ray Diffraction	1×10^{-5}	Barron et al. [27]
	Neutron Scattering	1×10^{-6}	Sokolov et al. [28]
Macroscopic	Interferometry	1×10^{-8} to 1×10^{-7}	Barron et al. [27]
	Strain Gauges	1×10^{-6}	Kabeya et al. [29]
	Capacitance Dilatometry	1×10^{-9}	Barron et al. [27]

Table 3.1: Techniques used in cryophysics for measuring length changes

length of a few millimeters, this equals an absolute resolution of 1×10^{-12} m to 1×10^{-9} m, i.e. a device is needed which can measure sub-Ångstrom length changes[1].

Table 3.1 summarizes the mostly used techniques to measure thermal expansion. Each method has its raison d'être. XRD(X-Ray diffraction) and Neutron scattering are microscopic, i.e. they can resolve the position change of atoms within a unit cell. Using X-ray powder diffraction one can study anisotropic expansion without the need for having a large single crystal [8]. Neutrons have a magnetic moment and thus it is possible to obtain information about the magnetic structure [30], too. However, both techniques lack in general the resolution to measure α at low temperatures. Strain gauges are sensors whose resistance depends on the strain acting on them [31]. If the attachment of the sensor on the sample is easily manageable, this method can be regarded as the least complex and most cost-effective one. However, in contrast to other techniques, their sensitivity is only moderate. Optical and capacitive techniques offer the highest resolutions. Optical techniques make use of various interferometric setups to measure length changes below the wavelength of optical light ≈ 5000 Å. Capacitive dilatometers measure the change of capacitance between capacitor plates and translate it to change in the plate distance. This is the current established standard for highly-sensitive[2] measurements [32]. Compared with optical methods, its setup is easier and it achieves higher sensitivities due to the use of the three-terminal method[3].

When choosing a particular method, one has also consider whether it is suitable for the use within a magnetic field in order to investigate magnetoelastic effects. The size of a capacitive dilatometer and its setup can be, for example, more readily adapted than a large commercial XRD setup.

The motivation for this is to build a setup operable in a magnetic field to measure the thermal expansion in a temperature range down to 5 K. Combined with the relative ease

[1] One could argue that having a larger sample would make measuring easier, but this is accompanied with unwanted temperature gradients within the sample. Additionally, samples, e.g. single crystals, cannot be produced in arbitrary sizes.

[2] A measurement is considered to be highly-sensitive, if it can resolve a length change of 1 Å or less [32].

[3] It is in fact possible to achieve a resolution of 1×10^{-9} with a Fabry–Pérot interferometer, but it involves a very sensitive and elaborate setup and is therefore rarely used [27].

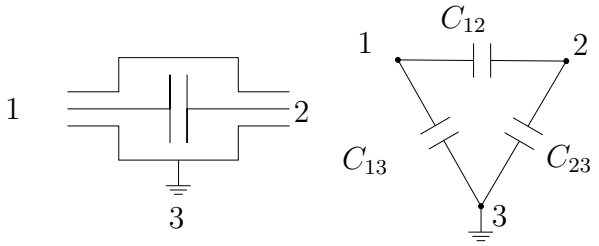

Figure 3.1: Left: Basic circuit of a three-terminal capacitor. Right: Delta-circuit representation. C_{12} denotes the capacitance to be measured, C_{13} and C_{23} the capacitances to ground.

of use, this makes capacitive dilatometry the method of choice.

3.2 Three-Terminal Method

The "secret" of the high sensitivity of capacitance dilatometry is the three-terminal method. It allows the measurement of capacitances eliminating the influence of unwanted stray capacitances. Fig. 3.1 shows a so called three-terminal-capacitor and its delta circuit representation. Terminal 1 and 2 represent the connections to the two capacitor plates/electrodes, Terminal 3 is connected to the shield, which prevents pickup of electrical noise at terminals 1 and 2. This is often also connected to a guard ring, which is used to have a homogeneous electrical field between the plates (see also section 4.3). The stray capacitances C_{13} and C_{23} shown in fig. 3.1 prevent an accurate measurement of small capacitances using a conventional two-terminal method (measuring directly at terminal 1 and 2). One would measure the sum of C_{12} and the capacitance to ground making an accurate measurement of C_{12} impossible, if they are in the same order of magnitude. In order to solve this problem, a capacitance bridge (see fig. 3.2) using the three terminals shown in fig. 3.1 was proposed by Thompson and Campbell [5, 33].

The different terminals of the capacitor shown in (fig. 3.1) can be found at the points (1), (2) and (3). V_1 and V_2 are precise 1 kHz sine wave voltages at the secondary windings of a transformer. Admittances are denoted by Y, the inverse of the complex impedance Z. Y_1 corresponds to an unknown capacitor C_1 and Y_a to the capacitance to ground of terminal (1). The lower leg of the bridge includes the same circuit for a well-defined standard capacitance C_2 and resistor Y_2 and the admittance of terminal ($1^\star$) to ground[4] Y_b. Y_0 is a sum of the admittances of *a*) one plate of C_1 to ground *b*) one plate of C_2 to ground *c*) the detector measuring V_0 . The impedances of the secondary windings are low compared to $1/Y_a$ and $1/Y_b$, whereas $1/Y_1$ and $1/Y_2$ are relatively high. Thus, finite Y_a and Y_b are effectively shunt. This is the reason, why one often defines terminal (1) as high (high admittance to ground) and terminal (2) as low (low admittance to ground). It can

[4]Terminal ($1^\star$) is only included in the drawing for clarification, during the experiment, only connections to terminal (1), (2) and (3) are made.

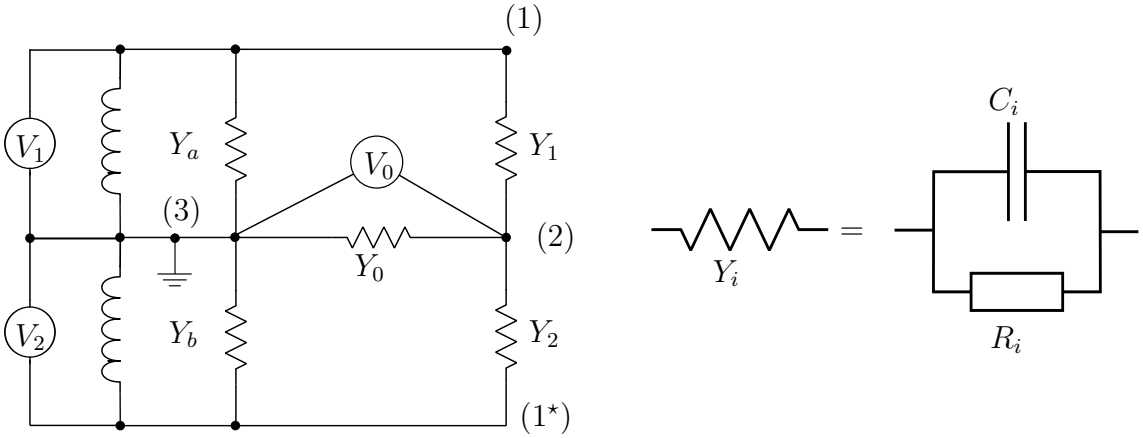

Figure 3.2: Left: Circuit for three-terminal capacitance bridge. V represent voltages and Y admittances (inverse impedances $Y = 1/Z$). Right: Circuit showing the composition of an admittance.

be shown via Kirchhoff's laws that[5, 34]

$$V_0 = \frac{V_1 Y_1 - V_2 Y_2}{Y_0 + Y_1 + Y_2} \tag{3.6}$$

V_1, V_2, C_2 and R_2 can be balanced such that $V_0 = 0$. Eq. 3.6 becomes then

$$\frac{Y_1}{Y_2} = \frac{V_2}{V_1}. \tag{3.7}$$

Using $Y = 1/R + i\omega C$ one arrives at

$$\frac{C_1}{C_2} = \frac{V_2}{V_1} \quad \text{and} \quad \frac{R_2}{R_1} = \frac{V_2}{V_1}. \tag{3.8}$$

Since C_2, V_1, V_2 and R_2 is known, one can measure C_1 and R_1. R_1 is also called loss.

So far, stray capacitances have not been addressed. Referring to fig. 3.2 two stray capacitances can occur: *a*) Terminal 1 connects to ground *b*) Terminal 2 connects to ground. In the first case, this is corresponding to the connections Y_a or Y_b, which are usually too low relative to the admittance through the secondary windings of the ratio transformer to have an effect on the voltage selection process. However, the longer the cable to the high terminal and thus their capacitance is, the larger Y_a becomes. Therefore, for very high accuracies or high capacitances, cable errors have to be corrected [35]. In the second case, an admittance is added which shunts Y_0. This does not affect the balance condition of the detector, since they are added to Y_0 [36]. However, a capacitance would reduce the noise, which the detector sees (high-frequency band pass), and a resistor would create thermal noise at the detector, which can influence its sensitivity [35].

In our experiment, the Anderling-Hagerling AH2550A capacitance bridge was used. It provides a resolution of 1×10^{-7} pF and an accuracy of 5 ppm. An order of magnitude estimation for the capacitor used within this experiment ($C \approx 1\,\text{pF}$, $A \approx 100\,\text{mm}^2$,$d \approx$

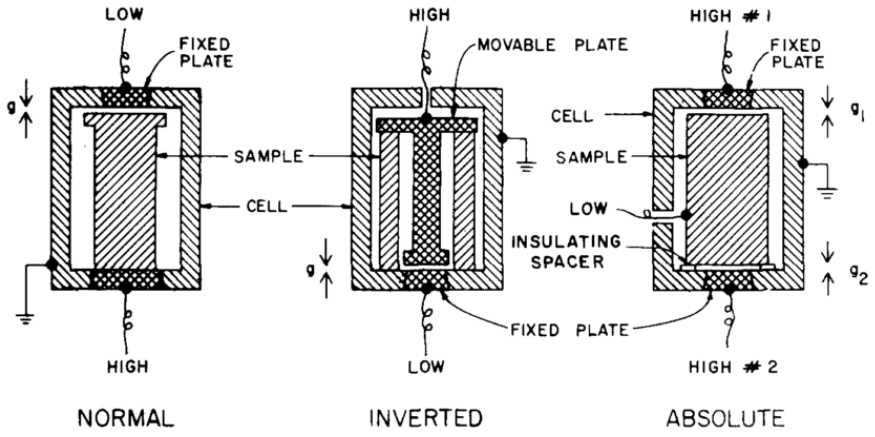

Figure 3.3: Schematic drawings showing three basic capacitance dilatometer setups. Normal: The sample is used as capacitor plate; Inverted: The expansion of the sample is transferred to the capacitor plates via a mechanical connections; Absolute: The sample is used as a capacitor plate and is isolated from the cell, hence having no cell effect. From [37].

1×10^{-1} mm) yields a length resolution of $\Delta l = 1$ pm fulfilling the precision requirements for a thermal expansion measurement which were estimated in section 3.1.

3.3 Capacitance Dilatometer

In general, the challenge of capacitance dilatometry is the design of the capacitor. The following points have to be considered:

Low Thermal Mass Ideally, the sample and the cell should be completely thermalized at the point of measuring the capacitance. Thus it should consist of material with a high thermal conductivity and low specific heat. Higher temperature sweep rates are then possible, which save time and coolant.

High Sensitivity For a parallel-plate capacitor, the sensitivity of the capacitance to a gap change can be quantified as

$$\left|\frac{\partial C}{\partial d}\right| = \frac{\epsilon A}{d^2}. \tag{3.9}$$

The higher the plate area and the closer the plates are, the better the resolution of the capacitor.

Low Cell Effect Unless an absolute method is used (see below), the thermal expansion of the dilatometer itself (plates, screws etc.) creates an unwanted background(cell effect) which has to be taken into account when determining α of a sample. Thus it is favorable to minimize this contribution and to make it well-defined.

Fig. 3.3 shows three fundamental configurations for three-terminal capacitance dilatometers. The "normal" configuration uses one side of the sample as a second plate. The

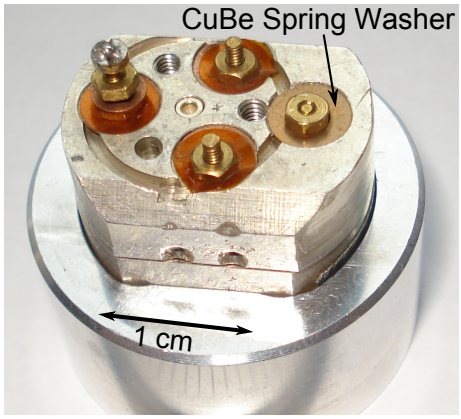

Figure 3.4: Photograph of the dilatometer used within this work. It sits on a stand for easier handling. The marked spring washer is used for clamping both halves together.

first three-terminal capacitance dilatometer was constructed in this way by White in his pioneering work [6]. "Inverted" setups separate sample and plates via transmitting the expansion through mechanical connections to a capacitor. It is called "inverted" since the gap is small for lower temperatures in contrast to the other methods. This provides higher sensitivities, where the thermal expansion is low. Both the "normal" and "inverted" type are differential techniques meaning that they measure the expansion relative to cell. This requires a calibration with a well-known reference sample in order to subtract the cell effect, thus restricting the accuracy to the reference data and the reproducibility of the cell effect. As in the "normal" design, the "absolute" type measures the capacitance between a metal plate and the sample. Additionally, the sample is thermally isolated from the cell. The cell temperature is kept constant while the temperature of the sample is varied. Because of the absence of the cell effect, this allows for very high accuracies (0.1 % in α [32])[5]. However this requires, that a thermometer and heater is connected to the sample, which can be a challenge, especially for small specimens. "Normal" and "absolute" require precise flat surfaces, whereas the "inverted" method does not necessarily do so. A review of the literature of the last three decades shows that the "inverted" method became the most widely used one [38, 39, 40, 41, 42, 43, 44, 45].

The dilatometer used in this experiment (see fig. 3.5 and fig. 3.4) is an improved version of the device described in [38]. It incorporates several design features, which have proven to be beneficial in other devices. Its main body is made of silver, which has favorable thermal properties. Silver has the additional advantage of having no nuclear heat capacity, thus having no Schottky anomaly at mK temperatures[6] as in [46]. Its small dimensions result in a low thermal mass, allowing relatively fast sweep rates of $0.3\,\mathrm{K\,min^{-1}}$. Sapphire is used to isolate the capacitor plates from each other. This is an advantage over organic

[5] Interferometeric techniques are also absolute.

[6] These temperatures are not reached within this experiment, 5 K at the cell is the lower limit.

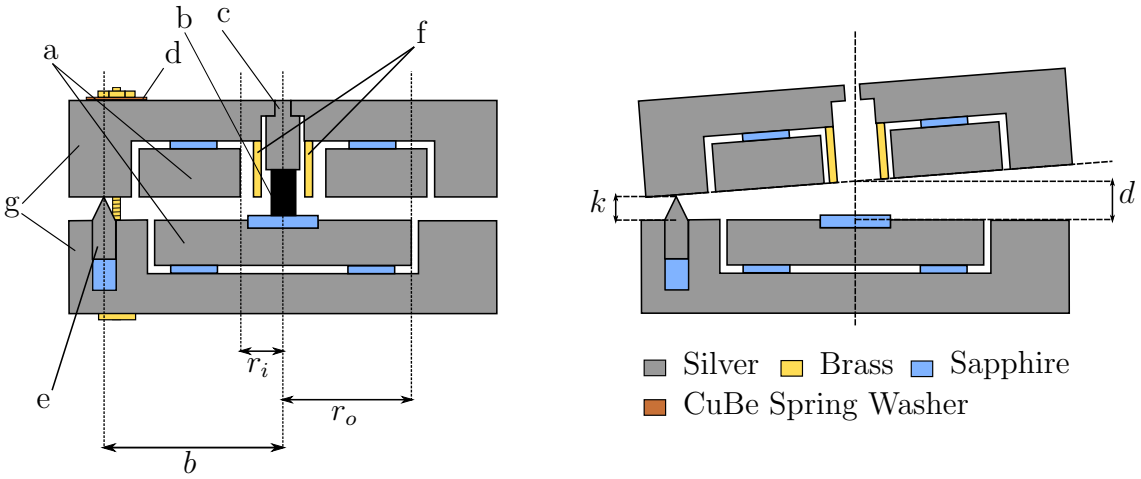

Figure 3.5: Left: Schematic drawing of the dilatometer. (*a*) Capacitor plates (*b*) Sample (*c*) Silver Spacer (*d*) CuBe-Spring (*e*) Cone-Bearing (*f*) Brass Shielding Cylinder (*g*) Housing. Right: Greatly exaggerated opening angle for clarity.

glues (e.g. StyCast), which often show relatively large creep effects leading to drifts in the capacitance[47, 39]. A brass cylinder prevents the sample from touching the plates and reduces the influence of dielectric materials on the capacitance. It acts as well as a guard in order to reduce fringe effects(see section 4.3). Silver spacer are put on top of the sample to allow various sample lengths while still being in the optimal capacitance range and to prevent the plates from short circuiting(see section 5.1). One specialty in its design is the tilted-plate principle, which is inspired by the work by Brändli, Griessen and Genossar [48, 49]. The upper half rests on cone bearings, which allow a rotation. This design enables the small size of the cell, since a similar sized cell with parallel plates would need a mechanism to transfer the expansion from the sample to the capacitor plates. Another advantage is the easier sample mounting, since the cell can be separated in its two halves. The cell are clamped together via a CuBe spring washer. Rotter et al [38] state the force acting on the sample as 50 mN to 500 mN. With a sample cross-section of $A \approx \pi(3\,\mathrm{mm})^2$, this corresponds to a pressure of up to 20 kPa. Since approx. 1 turn of the nut suffices to reach the plastic regime of the spring, it is assumed that approx. 500 mN are acting on the sample with the tension of 1 turn. Since the nut is progressing approx. 0.3 mm during 1 turn, the spring constant is estimated with $1700\,\mathrm{N\,m^{-1}}$.

The capacitance between the plates can be described by a tilted-plate-formula [38, 49, 34], which has been modified by Barcza and Mehboob [50, 51]:

$$C(d,T) = \frac{2\epsilon}{d^\star(T)} \left(\frac{A_o(T)\left(1-\sqrt{1-\gamma_o(d^\star(T),T)^2}\right)}{\gamma_o(d^\star(T),T)^2} - \frac{A_i(T)\left(1-\sqrt{1-\gamma_i(d^\star(T),T)^2}\right)}{\gamma_i(d^\star(T),T)^2} \right), \tag{3.10}$$

where

$$\begin{aligned}
\gamma_o(d^\star(T),T) &= \frac{r_o}{b}\left(\frac{k(T)}{d^\star(T)}-1\right) & \gamma_i(d^\star(T),T) &= \frac{r_i}{b}\left(\frac{k(T)}{d^\star(T)}-1\right) \\
k(T) &= k_0\left(1+\frac{\Delta l_{\mathrm{Ag}}}{l}(T)\right) & d^\star(T) &= d(T)\left(1+\frac{\Delta l_{\mathrm{Ag}}}{l}(T)\right) \\
A_o(T) &= \pi r_o^2\left(1+\frac{\Delta l_{\mathrm{Ag}}}{l}(T)\right)^2 & A_i(T) &= \pi r_i^2\left(1+\frac{\Delta l_{\mathrm{Ag}}}{l}(T)\right)^2
\end{aligned} \tag{3.11}$$

The plate distance is denoted as $d(T)$ and the literature values for the relative length change for silver is $(\Delta l/l)_{Ag}$ [52](see also fig. 9.1). The quantity k_0 represents the gap distance d, when the plates are parallel ($d = k$), b the distance from the center of the lower plate to the pivot at the cone bearing. The effective capacitor plate area is defined as $A_o - A_i$. All geometric constants refer to room temperature (293 K). The geometric parameters have to be replaced by effective ones, since fringe effects and machining imprecision are present(see section 5.1). $d(T)$ is replaced by $d^\star(T)$ to account for the expansion of silver (see below).

The formula aims at absorbing all expected thermal expansion effects of the dilatomerter itself to extract the largest non-predictible background signal during a measurement of the cell effect [53]. The cell effect is determined via measuring a silver sample, since then most of the sample's expansion is compensated (see also section 5.2). In this case, the following thermal expansion effects can be theoretically presumed:

Housing The sample is of the same material as the housing. Thus the housing expands at the same rate as the halves are pushed apart by the expanding silver sample. However, the part between the halves is not compensated leading to an increasing d. Thus $d(T)$ does not enter the eq. 3.10 directly, but via $d^\star(T)$.

Cone bearings The cone bearings are made of silver. However, as in (a), only the part within the gap has to be considered, since the rest is compensated by the expansion of the housing. This is accounted by letting k(T) expand.

Capacitor plates The radius of the plates increases with rising temperature, the area expands quadratically.

Sapphire Washers The sapphire washers below the plate expand less than silver. Therefore, the plates sink in the housing, since it expands more. To reduce the effect of the sapphire washers, a sapphire piece, which has double the length of the washers, is put below the cone bearings. This counters the effect of the sapphire washers below the plates, since then the amount, the halves are pushed away from each other by the cone bearings matches the amount the plates depart from each other caused by the smaller expansion of sapphire.

An ideal cell would then yield a zero length change when measuring silver within the model based an eq. 3.10.

One might ask the question, whether this formula is also applicable when using a non-silver sample, since it may not immediately obvious that one has to take into account an expansion of $d(T)$ and use $d^\star(T)$ instead. The answer lies in the differential method, i.e. a sample expansion is always relative to the cell effect measurement. Thus every expansion taken into account during the silver sample measurement has also to be considered during other measurements. This ensures that eq. 3.14 yields the literature values for silver, when a silver sample is measured.

Solving (eq. 3.10) for d cannot be done analytically, thus numerical algorithms such as Newton's method have to be used to relate the capacitance to a gap change (see also 3.6).

If one measures the expansion of silver sample, the following contributions to the gap change have to be taken into account [54]:

$$\Delta d_{\mathrm{Ag}} = \Delta d_{\mathrm{cell}} + \Delta d_{\text{cell-length-silver}} \tag{3.12}$$

The quantity $\Delta d_{\text{cell-length-silver}}$ represents the gap change coming from an Ag-sample which has the maximum length $\approx 4\,\mathrm{mm}$ of the cell. A non-Ag-sample with a silver spacer on top of it will lead to

$$\Delta d_{\mathrm{measured}} = \Delta d_{\mathrm{cell}} + \Delta d_{\text{Ag-Spacer}} + \Delta d_{\mathrm{sample}} \tag{3.13}$$

The quantity, one wants to obtain is $\Delta d_{\mathrm{sample}}/l_{\mathrm{sample}}$. Plugging eq. 3.12 into eq. 3.13 and solving for $\Delta d_{\mathrm{sample}}/l_{\mathrm{sample}}$ yields

$$\frac{\Delta d_{\mathrm{sample}}}{l_{\mathrm{sample}}} = \frac{\Delta d_{\mathrm{S}} - \Delta d_{\mathrm{Ag}}}{l_{\mathrm{sample}}} + \frac{\Delta d_{\text{cell-length-silver}} - \Delta d_{\text{Ag-Spacer}}}{l_{\mathrm{sample}}}. \tag{3.14}$$

The last term corresponds to the relative length change of a silver sample with length l_{sample}, thus

$$\frac{\Delta d_{\mathrm{sample}}}{l_{\mathrm{sample}}} = \frac{\Delta d_{\mathrm{measured}} - \Delta d_{\mathrm{Ag}}}{l_{\mathrm{sample}}} + \frac{\Delta l_{\mathrm{Ag}}}{l}(T) \tag{3.15}$$

3.4 Preparation of the Dilatometer

3.4.1 Grinding and Polishing

In general, the dilatometer has to be machined and prepared in such a way that the mathematical model (eq. 3.10) matches the device, e.g. $k = d$ if the plates are parallel. Thus, one has to ensure, that the plates and the housing sides facing each other are in-plane. This is achieved by grinding and polishing the dilatometer halves on the sides where they face each other. For this process a rotary grinding machine was used (model "ATM Saphir 520"). A common practice in metallography is to start with coarse grinding paper (plane-grinding) and then continue with the next finer one (fine-grinding) etc. till the desired roughness is achieved. The first paper used was ISO P500 (mean grain size

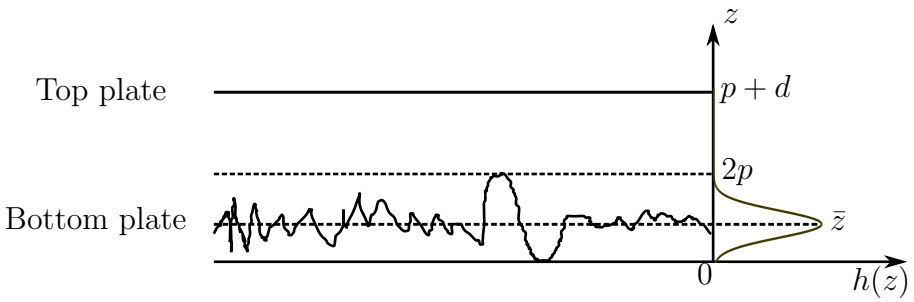

Figure 3.6: Model by [56] to model the influence of surface roughness on the capacitance. The top plate is ideally flat, the roughness of both plates is accounted for by the lower plate. $h(z)$ shows the height distribution (picture shows a normal distribution).

30.2 µm [55]). After several intermediate papers, the final grinding step was conducted with ISO P2500 paper (mean grain size 8.4 µm[55]) paper. A subsequent polishing with diamond lubricant was performed to achieve best surface quality (3 µm and 1 µm grain size).

In the following paragraph the question is addressed, by how much the capacitance of a non perfectly flat surface deviates from an ideally flat one. A model by [56] is adapted for a parallel-plate capacitor. If one assumes $d = k + 0.01\,\mathrm{mm}$ (a deviation of 0.01 mm from the parallel configuration), one yields differences below 0.1 % to the parallel case with $d = k$. Thus this model is assumed to be also valid for describing the influences of a non-perfect surface in the case of the tilted-plate dilatometer.

It is based on the fact that a rough plate can be divided into infinitesimal small parallel connected "terraces". These "terraces" can be described by a distribution $h(z)$. In order to account for the finite range of heights, a truncated distribution is used:

$$h(z) = \begin{cases} 0 & z > 2p \\ \dfrac{f(z)}{F(2p) - F(0)} & 0 \leq z \leq 2p\,, \\ 0 & z < 0 \end{cases} \tag{3.16}$$

where $f(z)$ denotes the probability density function and $F(z)$ the cumulative density function of a particular distribution, where $2p$ is the maximum height difference caused by a grain. The plates are modeled with one rough and one ideally flat surface instead of two rough surfaces (fig. 3.6). These models are equivalent, if the one rough surface combines the roughness of both plates. The distribution is normalized in such a way that

$$\int_0^{2p} h(z)\,\mathrm{d}z = 1, \tag{3.17}$$

which ensures that an ideal flat surface and the distorted surface have the same total area. If one assumes the biggest grain size used during the process, the maximum deformation depth can be safely estimated by $\approx 30\,\mu\text{m}$. The surface roughness[7] resulting from grinding with this grain size is approximately $5\,\mu\text{m}$ [57, 58]. Summing up the two surfaces yields then $2p = 60\,\mu\text{m}$. Using a truncated normal distribution with $\sigma = \sqrt{2(5\,\mu\text{m})^2}$ and a mean distance of $d = 0.1\,\text{mm}$, which is the order of magnitude encountered at our dilatometer, the relative error compared with a perfectly flat capacitor is

$$\left(\epsilon A \int_0^{2p} \frac{h(z)}{d+p-z}\,\mathrm{d}z - \frac{\epsilon A}{d}\right) / \left(\frac{\epsilon A}{d}\right) = d \int_0^{2p} \frac{h(z)}{d+p-z}\,\mathrm{d}z - 1 = 0.5\,\%. \tag{3.18}$$

It is assumed that average distance $d+p$ corresponds to the distance d of a ideally parallel plate. Since finer grains and polishing methods are used, one can safely neglect this contribution. This matches the findings of Schefzyk [34, 39]. He found that deviations $< 0.01\,\text{mm}$ from planeness cause only errors well below $1\,\%$. However, it is noted, that this contribution depends on the plate distance. If high sensitivity and thus low plate distances are needed, this error has to be taken into account [59].

3.4.2 Parallel-Plate Setup

After grinding, a dilatometer geometry has to be set up, in which the two plates are parallel. Doing this, it can be ensured that there is no tilt of the plates aside from the desired axis and k can measured (see fig. 3.5). The following procedure was used: A silver sample is mounted in the dilatometer. This Sample and the cone bearing are gradually changed in length via grinding and then the gap between the plates is examined with a microscope. If the distance between the plates is the same along the whole gap, parallelism is achieved. If this is the case, the capacitance was measured to translate it to k via $d = k = \epsilon A/C_0$. To obtain an error estimate, the setup is repeated ten times by opening and closing the dilatometer halves. The variation of the distance between the plates along the gap ($d = 0.19\,\text{mm}$) was $< 0.02\,\text{mm}$. The mean capacitance for the parallel setup was then determined to be

$$C_0 = 5.327(14)\,\text{pF} \tag{3.19}$$

3.5 Temperature Control

If a sample with α and a temperature difference of ΔT is assumed, one yields a relative length change of $\Delta L/L \approx \alpha \Delta T$. Since $\Delta l/l \approx \alpha \Delta T$ and $\alpha \approx 1 \times 10^{-6}\,\text{K}^{-1}$, in principle a temperature stability of $\approx 1\,\text{mK}$ or less is desired to not interfere with the best resolu-

[7] Here defined as the standard deviation of the surface height distribution.

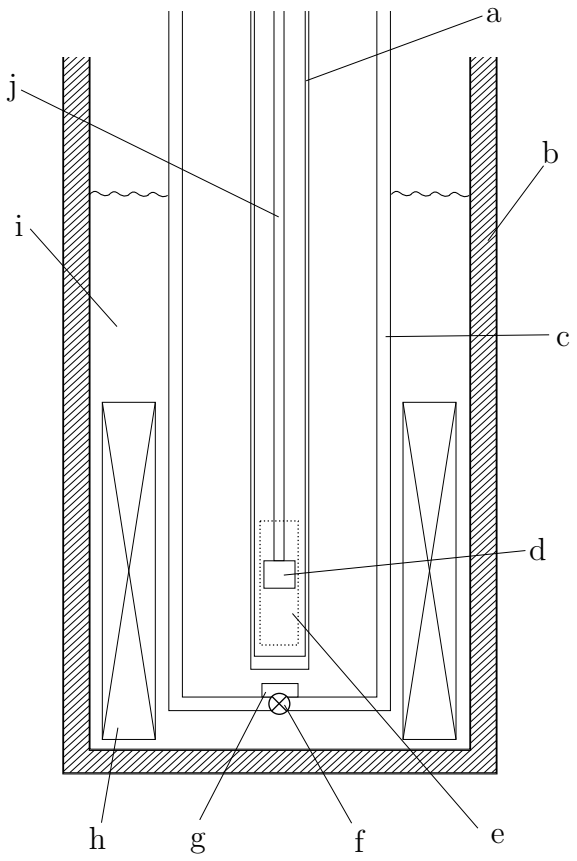

Figure 3.7: Schematic drawing showing the cryostat used within this experiment. (*a*) Shielding tube containing exchange gas (*b*) Vacuum-insulated Dewar (*c*) Vacuum-insulated Variable-Temperature-Insert (VTI) (*d*) Dilatometer with Sample (*e*) Sample Heater (*f*) Liquid-flow needle valve (*g*) Gas heater (*h*) Magnet (*i*) Liquid Helium (*j*) Sample rod containing all cables. Based on [60].

tion given by the capacitance bridge of 1×10^{-9} in $\Delta l/l$. Maintaining this stability and measuring with such a precision over a wide range of 4 K to 300 K is challenging as the following paragraphs show. This leads to the insight that temperature control is crucial and a resolution-limiting factor.

In order to achieve a temperature range of 4 K to 300 K and a stable temperature sweep, a commercially available gas-flow cryostat from Oxford-Instruments was used. A sketch of the full setup including the sample rod is shown in fig. 3.7. The temperature within the variable temperature-insert (VTI) is stabilized via a balance of cooling power of cold helium gas and heating power of a resistance heater, which sits at the needle valve and adjusts the temperature of the gas flowing trough it. The VTI is pumped by a rotary vacuum pump ($35\,\mathrm{m^3\,h^{-1}}$) to achieve a continuous gas flow. The boiling temperature of helium at atmosphere pressure is $T_b = 4.2\,\mathrm{K}$. Temperature below T_b can also be achieved, since the pressure within the VTI is reduced below the vapor pressure of helium by the pumping. Hence, below T_b, liquid helium will flow within the VTI and boil at lower temperatures

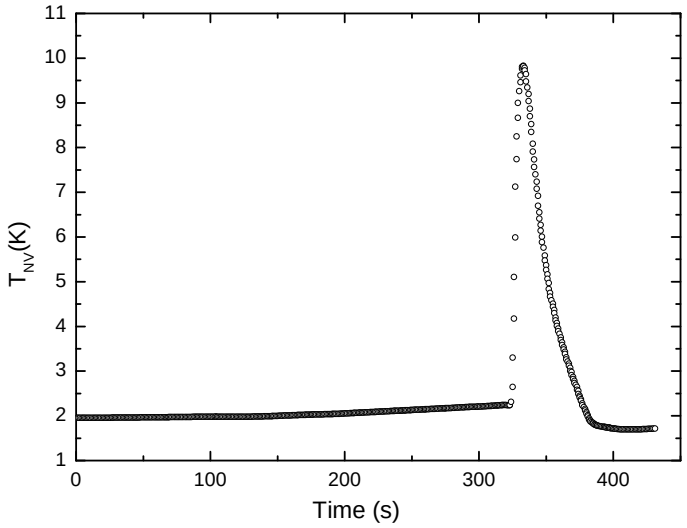

Figure 3.8: Temperature at the needle valve T_{NV} vs time during a slow PID-controlled heating below 4 K. The reason for the sudden jump is unknown. The lambda transition of liquid helium might play a role, since the latent heats of He-I and He-II differ.

thus cooling the sample further [8]. Stabilizing below 4 K is possible (specifications of the cryostat state 1.5 K as the lowest achievable temperature). However, a proven lowest starting temperature for sweeps is 4 K. Lower starting temperatures tend to a sudden temperature increase, when it was tried to gradually heat up the sample (fig. 3.8). The exact reasons are unknown. However, the sudden increase in temperature might be related to the drop in latent heat during the lambda transition of helium [62][9]. The heater and needle valve are automatically controlled by a temperature controller through a PID-algorithm[10]. The thermometer used as a feedback for this loop is sitting at the base of the VTI at the needle valve (see section 3.8).

While the thermometer at the vaporizer is well placed for feedback control of the needle valve and heater, the distance and thermal path is too large to measure a reliable value for the temperature at the dilatometer. As a remedy a second thermometer (see section 3.8) was attached to the dilatometer. A setup only using the temperature control of the VTI would yield a temperature stability within 50 mK to 100 mK (see [63] and fig. 3.10). In order to increase the stability, a second resistance heater was constructed to heat the dilatometer directly within the sample space. This allows a finer temperature tuning. $T = 200\,\mathrm{K}$ can be hold stable with fluctuations $\leq 2\,\mathrm{mK}$ (see fig. 3.7). However, this comes at the expense of greater complexity since the sample heater is as well controlled by a

[8] Helium does not solidify at these pressures and temperature ranges. The lowest temperature limit is set by the pumping power and the heat input of the surrounding parts (sample rod, non-perfect insulation etc.) [61]

[9] Ekin [60] mentions that, superfluid creep increases the gas flow rate and lowers the ultimate cooling power of the system, which could also relate to this effect.

[10] The differential term has not been used.

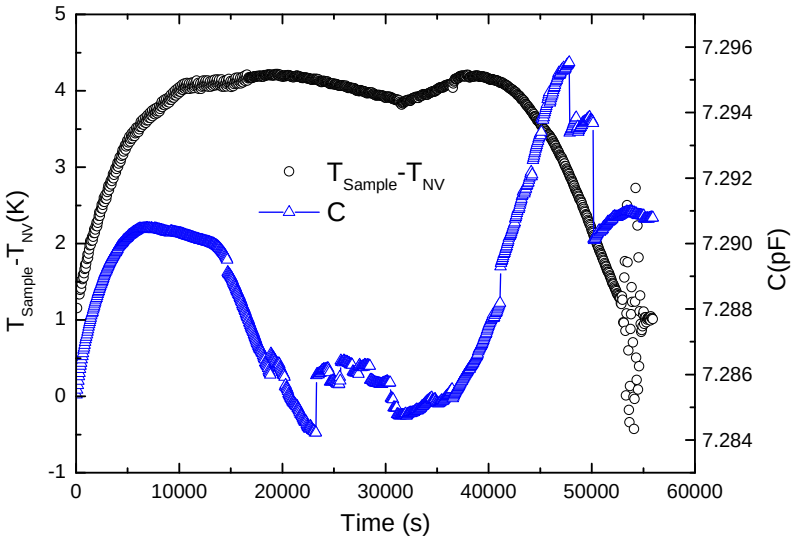

Figure 3.9: Temperature Difference between the thermometer at the vaporizer/needle valve T_{NV} and the thermometer at the sample T_{Sample} without using the additional heater surrounding the sample (sweep rate $0.3\,\mathrm{K}^{-1}$). The temperature gradients within the cell become too large and cause glitches (see section 4.4).

temperature controller using a PID-algorithm. Thus two entangled PID-mechanisms are present, which requires more tuning effort.

Figure 3.9 shows the behavior of the capacitance without the use of the second heater: The relaxation time (see section 4.6) does not allow a quasi-stationary cooling (see section 4.6). The gradients become too large and cause glitches. Lower sweep temperatures or better thermal coupling would have to be used.

The vaporizer heater is set to a temperature 1 K lower than the sample heater, so the sample heating power is balanced by an approximately constant cooling power. With the limit of 4 K at the vaporizer, the effective lower limit at the cell is then 5 K. The total power released over the sample heater resistance ($\approx 240\,\Omega$) ranges from ≈ 0.1 W to 1 W over the whole temperature range of 4 K to 300 K.

Figure 3.10 shows the difference between set and actual temperature at the vaporizer and the cell. While the temperature stability at the needle valve is partly poor (± 100 mK at 50 K), the temperature of the cell can be held stable within ± 10 mK. The fast stabilization at 50 K at the vaporizer is caused by a change in PID parameters. However, the temperature starts to fluctuate at around 200 K, which could not be related to the use of different PID values of either temperature controller.

The dielectricity of liquid helium (see section 4.1) and cable movement caused by the gas flow and varying pressure on the device could create unwanted noise. Therefore, the sample rod was put into a shielding tube made of stainless steel. The part covering the area of the dilatometer is copper, since its thermal conductivity over 10 times larger [60] than stainless steel. Thermal contact to the VTI space is achieved by using helium as an

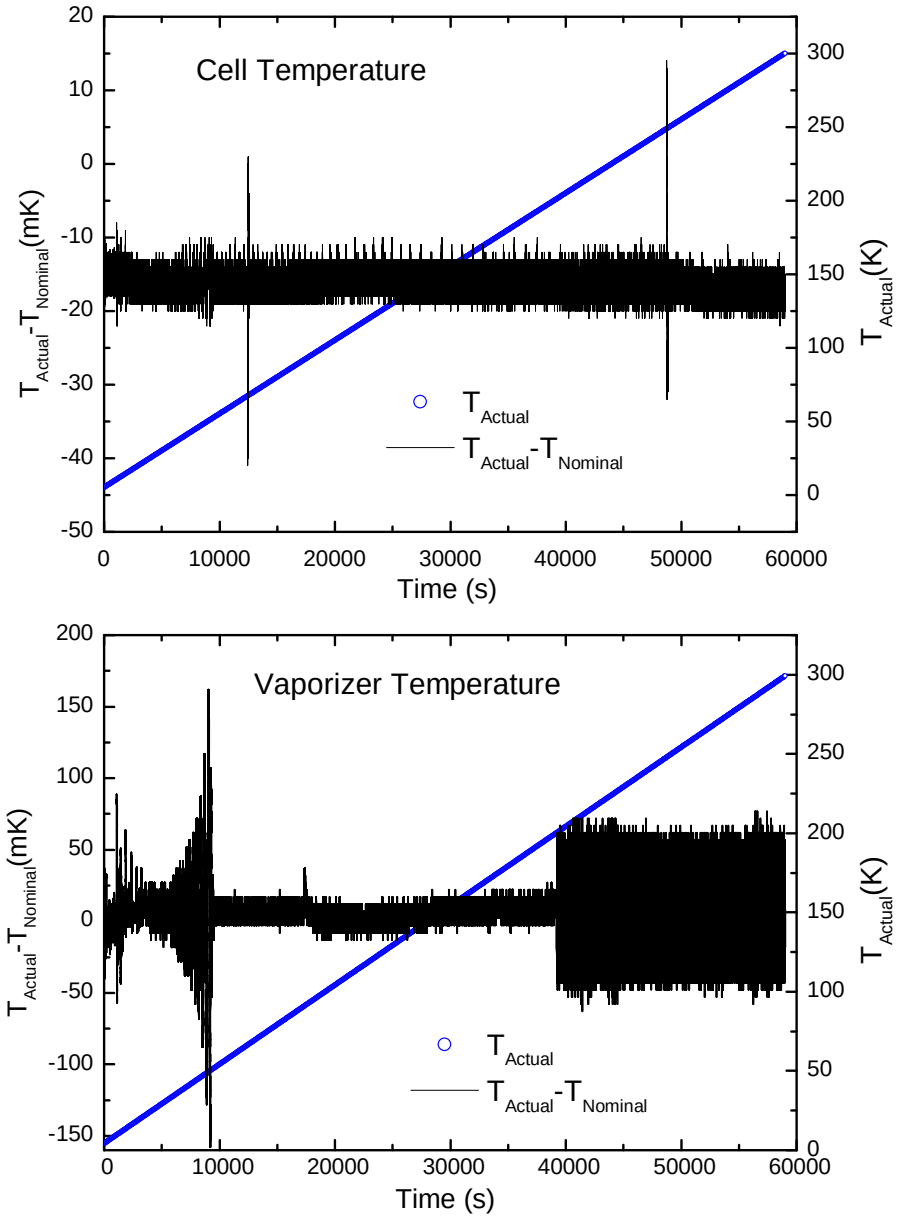

Figure 3.10: Top: Typical temperature stability at the cell. Bottom: Typical temperature stability of the thermometer at the vaporizer. T_{nominal} is the set temperature (linear profile with a specific rate) and T_{actual} is the actual measured temperature.

exchange gas in the sample space. This has also the advantage of creating thermal contact without electrical contact, since this would create a connection between dilatometer ground and cryostat ground, which could affect the measurement of the capacitance bridge (see section 3.2). The used exchange gas pressure ranged from 20 mbar to 300 mbar at room temperature between measurements (for a more detailed discussion see section 4.1).

3.6 Data Analysis

In order to translate the measured capacitance vs. temperature data into a relative length change and thermal expansion, several numerical operations were performed:

Numerical Solution of Eq. 3.10 The solution of eq. 3.10 has to be found numerically. The robust and reliable Newton's method is used. Since the function has no inflection points, there is no risk being trapped in a non-converging infinite loop. The method needs usually around 5 steps to converge. The algorithm is implemented in Mathematica, which runs consistency checks to guarantee a certain precision.

Binning of Data In order to reduce the number of data points, the noise and to obtain a smooth derivative (see also 4.2), the data is "binned". The data is grouped into windows of around 50 data points and the group is replaced by the group mean value.

Interpolation Some calculations involve combining two different data sets (e.g. cell effect and signal). In order to perform calculations although the data sets do not have points at the same temperature, one data set is interpolated via splines. The curve is interpolated piecewisely with a B-spline-approximation yielding smooth, differentiable curves.

Numerical Derivation In order to obtain the thermal expansion coefficient α, $\Delta l/l$ is derived. This is done by interpolating of the data via the method described above and then deriving it.

Glitches Glitches(see section 4.4) are easily visible in the derivative of $\Delta l/l$ α as outliers. Glitches are automatically removed via grouping the data into windows and then deleting points within these windows whose difference to the mean value of the group is greater than $m\sigma$, where $sigma$ is the standard deviation and m a factor depending on the quality of the data.

Numerical Integration In order to obtain a $\Delta l/l$ without glitches, α is integrated after removing the outliers, which represent glitches.

All steps above are done in Mathematica 8.0 which runs consistency checks to ensure precision. Everything is based on robust and reliable algorithms, so the error introduced by truncation is assumed to be negligible compared with errors related to the setup.

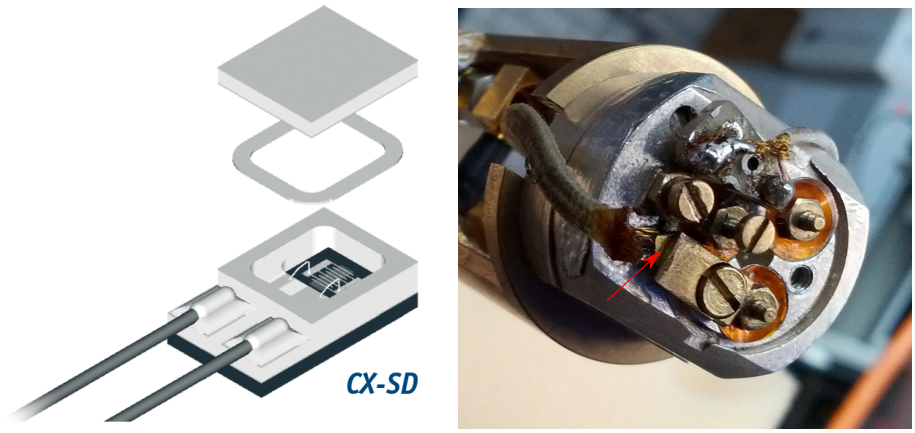

Figure 3.11: Left: Technical Drawing of a Cernox thermometer. A thin film of zirconium oxide is sputtered on a sapphire base and vacuum sealed within a cell to allow easy mounting without breaking the resistance. From [65]. Right: Photo showing the mounting of the thermometer at the dilatometer: The sensor (marked) is fixed with a brass clamp and greased with a thin film of Apiezon N (not visible).

3.7 Sample Preparation

Samples often have to be modified to fit into the cell. The maximum height after steps 3.4.1 and 3.4.2 is slightly below 4.1 mm. Their cross-section must fit within a circle of diameter 3 mm to not cause blockage within the cell. Two surfaces of the sample should be approximately parallel. To improve stability, a cuboid or cylindrical shape is beneficial. If necessary, the sample was cut with a diamond saw (model "Well 3032-4"). The surface roughness resulting is comparable with grinding ($\approx 1\,\mu m$ to $10\,\mu m$) [64].

3.8 Thermometry

General considerations when choosing a thermometer for this application involve

Temperature Range The thermometer should be able to cope with a range of 4 K to 300 K.

Response Time Since it is measured using a temperature sweep, the thermometer should thermalize within reasonable time, so the capacitance can be linked properly to the corresponding temperature.

Accuracy The deviation from the measured value to the true value should be low, preferably below 1 %.

Sensitivity / Resolution In order to resolve length changes of $\Delta l/l \approx 1 \times 10^{-9}$, a sensitivity of 1 mK or better is desired (see section 3.5).

Magnetic Field Thermometer use the temperature dependence of a resistor to measure the temperature. A magnetic field can hinder charge carriers and thus create an additional resistance, which is called magnetoresistance yielding an error in the

temperature. Thus for measurements within B-fields, a sensor with low magnetoresistance should be chosen.

For our purpose, Cernox "CX-1050" thermometers by Lake Shore Cryotronics were used. The measured resistance consists of thin film of zirconium oxide Zr_2ON_2, which has semiconductor-like resistance properties. Fig. 3.11 shows the model ("CX-1050-SD-1.4L") used to measure the temperature at the dilatometer and how it is mounted at the dilatometer. The model ("CX-1050-AA-1.4L") at the needle valve within the VTI space differs only in the packaging of the sensor.

Range	0.3 - 325 K
Resolution	0.1 mK at 1.4 K 0.1 mK at 1.4 K 0.5 mK at 77 K 20 mK at 300 K
Accuracy	6 mK at 1.4 K 7 mK at 4.2 K 110 mK at 77 K 450 mK at 300 K
Response Time	15 ms at 4.2 K 0.25 s at 77 K 0.8 s at 273 K

Table 3.2: Typical Specifications of a Cernox thermometer [65]

Tab. 3.2 shows the specifications of a typical Cernox thermometer. All parameters suit to the use with the capacitance cell. However, the resolution of 20 mK at 300 K is striking and limits our resolution at the point where α is the highest being at the order of 1×10^{-5}, thus no better resolution in $\Delta l/l$ than 1×10^{-7} is expected.

One strength of Cernox thermometers is the insensitiveness against magnetic fields[11]. Since magnetostriction effects are larger the lower the temperature is [66], one tries to undergo measurements at the lowest temperature possible. This has also the advantage of a better temperature stability (see also section 4.6). However, the downside is the higher magnetoresistance of the thermometer, which introduces temperature errors.

The maximum error is determined by Brandt et al. [67] to be $\Delta T/T = -1.38$ at 18 T. [12] The temperature calculated by the temperature controller based on a resistance vs. temperature curve would be $5.0\,\mathrm{K} \times \Delta T/T = 0.069\,\mathrm{K}$ too low in this case. The temperature controller will increase the power released in the heater to compensate for this phantom cooling effect. Thereby, through thermal expansion, the sample expands by

[11] This is exactly the reason, why one cannot use, for example, a platinum resistor as a thermometer, which has a better resolution at high temperatures.

[12] The maximum magnetic field the cryostat is able to deliver is 17 T.

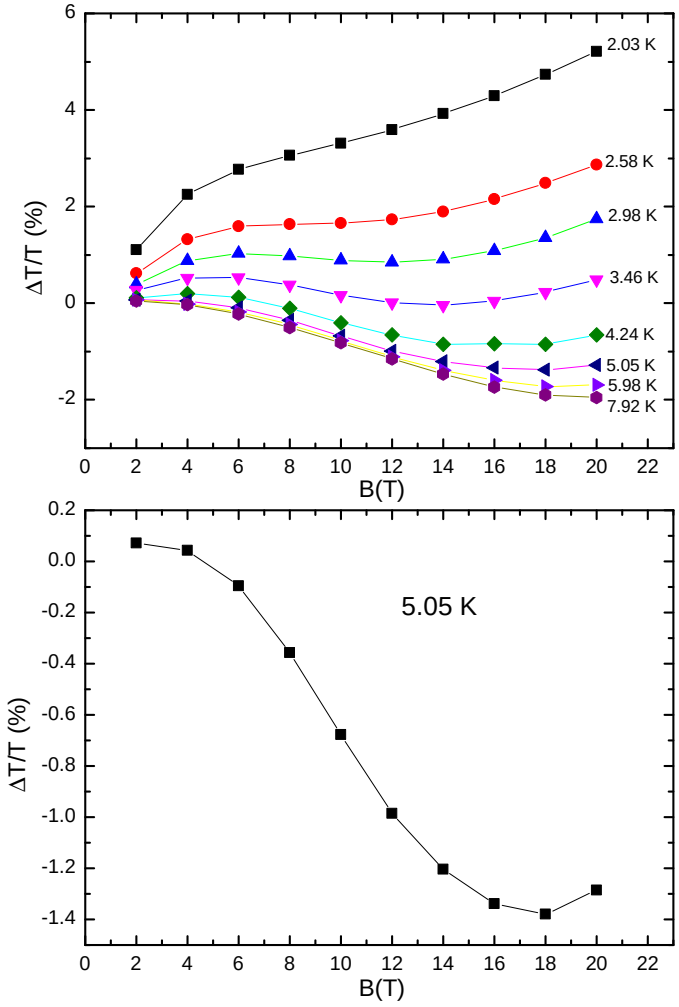

Figure 3.12: Top: Plot showing the magnetic field dependence of the relative temperature error of the thermometer at the dilatometer at different temperatures. Bottom: Plot showing the error for 5 K, which is the temperature used for measuring magnetostriction. Data from [67].

$\Delta L/L \approx \alpha(5\,\mathrm{K})\Delta T = 1 \times 10^{-9}$. Magnetostriction effects lie in the order of magnitude of 1×10^{-8} i to 1×10^{-7} in $\Delta l/l$ (see also section 5.10). Thus, this overall constitutes a relative error of about 1 % to 10 % depending on field and magnetostriction.

3.9 17 Tesla Magnet

The cryostat is fitted with a wet[13] solenoid magnet capable of delivering up to 15 T at 4.2 K. It consists of a mixture of NbTi (outer sections) and Nb_3Sn(inner sections) [68], which are both superconducting at liquid helium temperatures.

The field strength can be increased up to 17 T by additional pumping at the lambda stage

[13]Immersed in liquid helium

with a strong pump. This sucks in helium close to the magnet and lowers its vapor pressure. It will then cool via its latent heat and temperatures below 4.2 K are achieved (see section 3.5). Caused by buoyancy, the cool liquid helium will collect at the bottom of the lambda stage and cools locally the helium. The magnet is then cooled by convection currents within the helium bath. Since the thermal conductivity of gaseous helium is relatively poor, a steep temperature gradient will form at the boundary between the liquid and gaseous phase, thus ensuring that the helium bath above the lambda stage is not heated by much. Thus, this method is more efficient than pumping directly at the bath.

The deviation of the magnetic field along the cell is maximal 0.2 % [63] and since $\Delta l/l = \Delta H \lambda$, it is not greatly influencing the accuracy of magnetostriction measurements. The current resolution of the magnet's power supply is 0.1 mA. The magnetic field is calculated simply via $H = kI$, where $k = 0.1460\,\mathrm{T\,A^{-1}}$, thus $\Delta H \approx 1 \times 10^{-5}\,\mathrm{T}$. If one assumes a magnetostriction of $\lambda \approx 1 \times 10^{-6}\,\mathrm{T^{-1}}$, a resolution limit of the field in $\Delta l/l$ of 1×10^{-11} results, which is below the resolution of the dilatometer (see also fig. 5.10).

4 Systematic Errors

4.1 Exchange Gas

In this section, the question is addressed too which extent the dielectricity of the exchange gas (helium) influences the capacitance. The dielectricity of gaseous helium $\epsilon_{\mathrm{He}} = 1.000\,063$ [69] at NTP[1] can be safely neglected. The Clausius-Mosotti equation relates the dielectricity with the polarization α_p [18]:

$$\epsilon - 1 = \frac{n\alpha_p}{\epsilon_0} \Big/ \left(1 - \frac{n\alpha_p}{3\epsilon_0}\right) \approx \frac{n\alpha_p}{\epsilon_0}, \tag{4.1}$$

where n is the number density and ϵ_0 the vacuum permittivity. The approximation on the right can be made for gases, since their n is low [70]. The polarization α_p is an atomic property and is thus constant in the gaseous phase. Since Helium can be well approximated as an ideal gas, one yields $\epsilon - 1 \propto p/T$. Assuming a maximum temperature change of 300 K to 4 K or reducing the pressure from 1000 mbar into the 1 mbar range, does not create variations in ϵ greater than in the permille range[2]. Hence, even at low pressure and low temperature, the influence of the dielectricity of helium gas on the capacitance is too small to have to be taken into account.

However, in its liquid phase, ϵ changes to 1.0480 [72], which poses a significant error if it would be neglected. This is the reason, why it is not advisable to put the dilatometer directly into the helium flow, since at low temperatures 2 K to 4 K liquid helium might reach the capacitance plates and create disturbances [54].

In the experiment performed during this work, the shielding tube is firstly evacuated, then filled with helium and sealed at room temperature to a specific pressure. Helium liquefies at 4.2 K at 1 atm pressure. The vapor pressure at 4 K is $\approx$ 800 mbar [60, 73]. Since the vapor pressure and the pressure inside the tube are decreasing monotonically [3],

[1] Normal Temperature and Pressure. $T = 25\,^{\circ}\mathrm{C}$ and $p = 1$ atm are assumed (authors do not give concrete information).

[2] Both dependencies have been experimentally tested by van Itterbeck [71] and Clay [69] down to 20 K and 2 atm.

[3] Since there is temperature gradient from the top to the bottom of the sample rod, it is not safe to say that the pressure is $\propto T$.

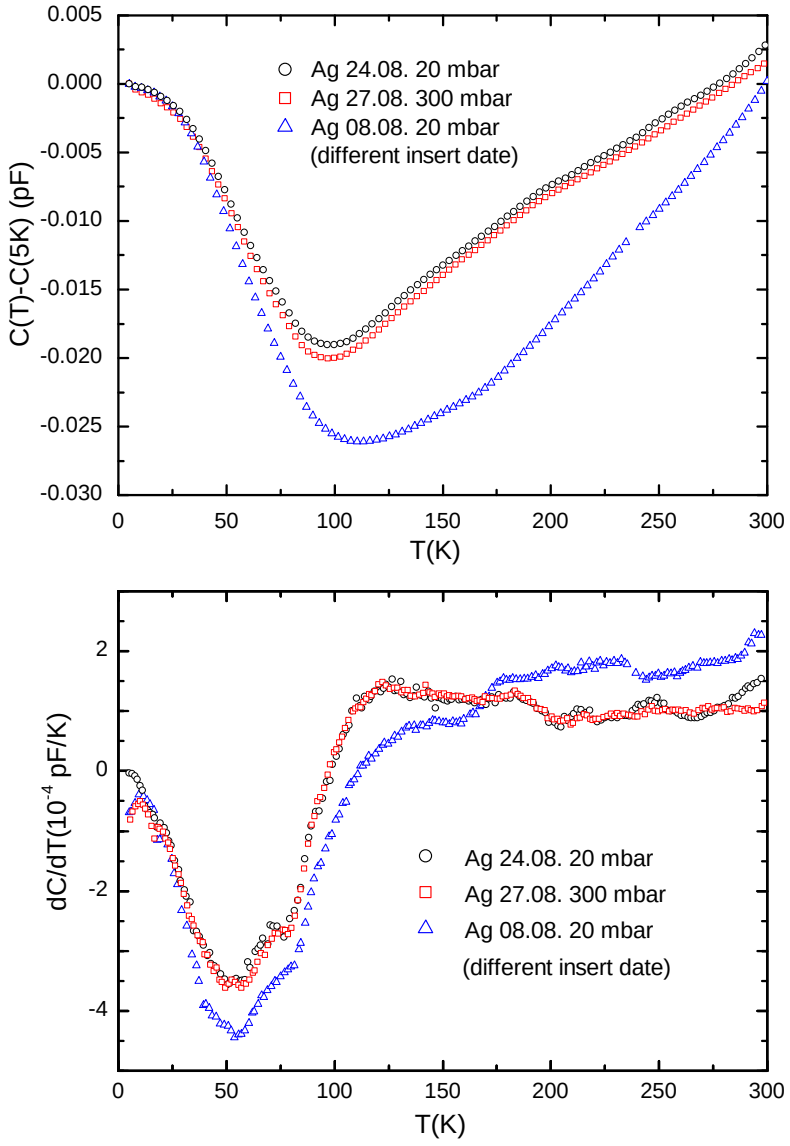

Figure 4.1: Top: Capacitance vs temperature during three temperature sweeps with a silver sample. The upper two curves correspond to different pressures of the exchange gas at room temperature. The sample was not reinserted into the cell between the measurements. The lower curve corresponds to the same sample, but it has been reinserted resulting in a reproducibility error unrelated to the helium gas pressure. Bottom: Derivatives of the curves shown in the upper plot.

it is impossible for the helium volume within the tube to liquefy in the temperature range 4 K to 300 K, if its pressure is 800 mbar or less at room temperature. However, residual gases (oxygen, carbon dioxide, nitrogen) or water could could cause problems and thus one should take care to have a clean exchange gas and sample space. Köckert [74] discusses residual gas effect and assesses an error of ca. 1×10^{-7} in $\Delta l/l$ for "dirty" exchange gas (no quantification given), which does not constitute a large influence on $\Delta l/l$. However, phase transitions of residual gas components might cause sudden changes in the capacitance, which could be visible in the data.

In some cases it is preferable to use a non-arbitrary exchange gas pressure, since at low pressures below ≈ 10 Pa the thermal conductivity of helium scales linearly with pressure (above it is pressure-independent) [60]. Thus it is possible to control the cooling power of the gas flow within the VTI space at low temperatures and low pressures. This is important in bath cryostats, since this is the only way to control cooling and to compensate the growing temperature gradient between sample space and helium bath. In our case, however, the PID-temperature controller automatically adjusts the needle valve. During the first half of measurements, pressures around 300 mbar at room temperature were used. To check for influences of residual gases, the pressure was later reduced to 20 mbar. No significant influence on the capacitance was noticed (see fig. 4.1).

4.2 Numerical Errors

During the translation from the measured capacitance to a relative length change and the thermal expansion coefficient, several numerical operations are performed which are can be afflicted with an error:

- Numerical Solving of Equation 3.10
- Derivation of relative length change to obtain thermal expansion coefficient
- Integration of "deglitched" thermal expansion coefficient to obtain a smooth relative length change

Naturally, the derivation is the most hazardous one, since it involves small differences of the experimental data. The error propagation by using differences boosts the error to a much higher level than of the data being derived [75].

To estimate the effect of a noise in the relative length change and its consequences on the thermal expansion coefficient, a 20th-order polynomial is fitted against the literature data of copper [37] and the resulting polynomial is derived analytically. The effect of limited precision is simulated via a random noise added to the polynomial in the order of the precision of the dilatometer (1×10^{-7}). This noisy signal is then derived using the methods from section 3.6 and compared with the exact derivative(see fig. 4.2). The resulting error is in the range of 10 %. However, binning of the noisy signal reduces the

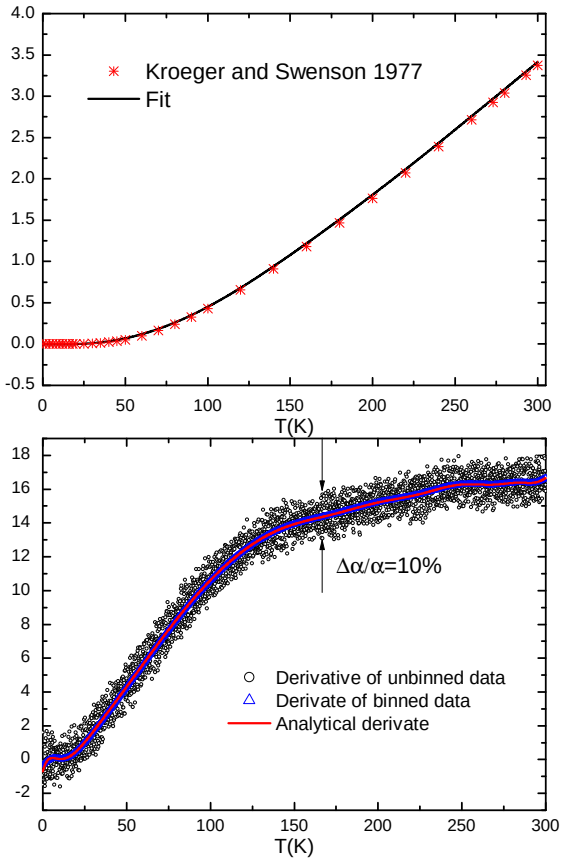

Figure 4.2: Top: A polynomial is fitted against literature Data for Copper from Kroeger and Swenson [37]. Bottom: Showing (a) the analytical(exact) derivative of the polynomial, (b) the derivative of the polynomial with added noise and (c) the derivative of the binned noisy polynomial. The thickness of (c) is bigger than the error for clarification.

error effectively.

4.3 Inhomogeneity of the Electrical Field / Fringe Effects

Theoretically, (eq. 3.10) does only hold if a situation is considered, where the plates extent infinitesimally and where the capacitance is calculated between two specific areas on these plates. However in finite dimensions fringe effects have to be considered, which cause an inhomogeneous electrical field at the boundaries of the capacitor plates(fig. 4.3). This creates an additional contribution to the capacitance, since there is more surface connected with electrical field lines and thus more charges can be stored.

In order to estimate fringe effects, formulas found by Kirchhoff [77], Maxwell [78] and Scott and Curtis [79] are available for circular geometries. However, the task of finding analytical expressions for the capacitance becomes quickly challenging when deviating from these geometries [80].

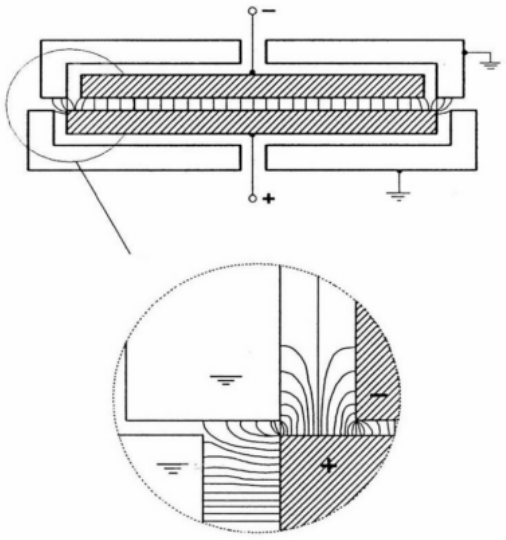

Figure 4.3: Graphic showing the inhomogeneity at the boundaries of capacitance plates. The field lines "crawl" around the fringes and cause an additional capacitance contribution. The shown configuration differs from the setup used in this work. From [76].

The basic, parallel configuration of our capacitor is shown in fig. 4.4. Neglecting edge corrections, the effective area is $\pi(r_o^2 - r_i^2)$. The capacitor is reduced to the annular geometry shown in fig. 4.4 (b). This will overestimate the edge corrections for the following reasons:

- The edge at R_o does not contribute to the capacitance, since $R_o - r_o > 3d$ [79, 81].
- There is an additional edge at r_i.
- The housing is removed, and therefore no guard electrodes connected to ground are present (the capacitance to ground does not add to the measured capacitance, see section 3.2).

In this geometry, an estimate of the edge corrections can be made based on the method of Johansen [82]: The area $\pi(r_o - r_i)^2$ of the annular capacitor is mapped on n parallel connected circular capacitors with radii ρ, where it is possible to apply Kirchhoff's formula [79]

$$C_n = \epsilon \frac{A}{d} \tag{4.2}$$

$$C_e = C_n \frac{2d}{\pi\rho} \left(\log \frac{8\pi\rho}{d} - 3 + z \right) \tag{4.3}$$

$$z = (1 + x) \log 1 + x - x \log x \tag{4.4}$$

$$x = t/d. \tag{4.5}$$

The radius ρ is determined by the constraint that the total circumference and area of the

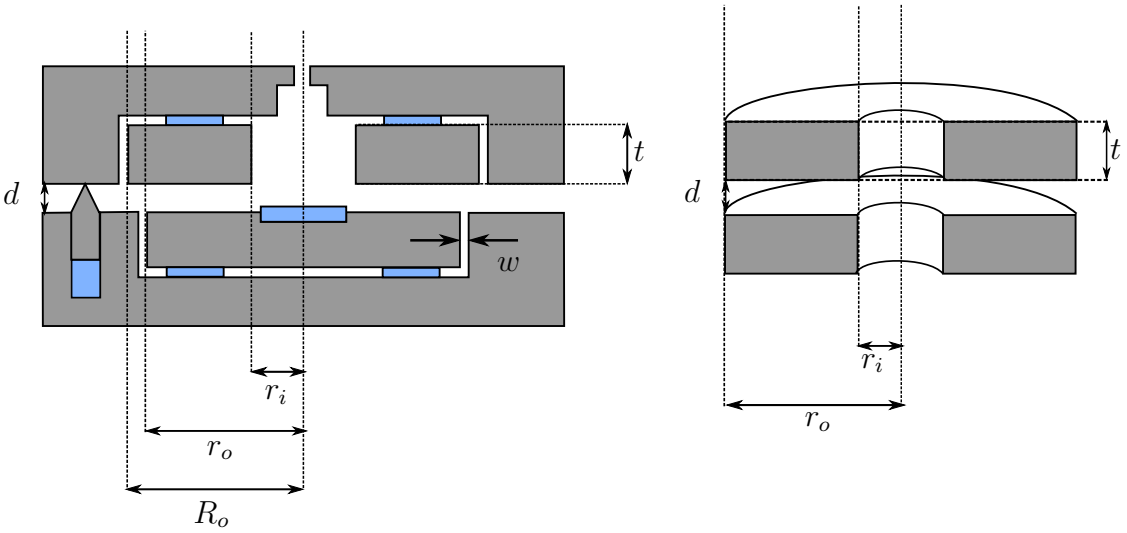

Figure 4.4: Left: Schematic Drawing showing quantities important for the estimation of fringe effects of the cell. Right: Simplification of cell geometry for an analytical estimate of fringe effect errors.

n capacitors and the original capacitor are equal:

$$\pi(r_o^2 - r_i^2) = n\pi\rho^2 \tag{4.6}$$

$$2\pi(R + r) = n2\pi\rho \tag{4.7}$$

With $r_o = 6\,\text{mm}$, $r_i = 3\,\text{mm}$, $b \approx 0.1\,\text{mm}$, $t \approx 2\,\text{mm}$, one yields

$$\frac{C_e}{C_n} = 9\,\%. \tag{4.8}$$

To estimate the effect of guarding by the housing and the brass cylinder, one can use Maxwell's formula for a circular Kelvin guard ring capacitor with the same plate distance $d = 0.1\,\text{mm}$ and area $A = \pi(r_o - r_i)^2$ [78] and calculate the relative deviation to an ideal capacitor without any edge effects with $C_{\text{uncorr}} = \epsilon A/d$ via

$$\frac{C_{\text{corr}}}{C_{\text{uncorr}}} = 1 + \frac{wd}{r(d + 0.22w)}\left(1 + \frac{w}{2r}\right). \tag{4.9}$$

The correction of edge effects is then

$$1 - \frac{C_{\text{corr}}}{C_{\text{uncorr}}} = 6\,\%. \tag{4.10}$$

An unguarded configuration only taking finite dimension into account would result for a circular capacitor in [79]

$$\frac{C_{\text{finite, unguarded}}}{C_{\text{uncorr}}} = 1 + \frac{4d}{\pi r_o}\left(\log\frac{4\pi r_o}{d} - 3 + z\right) = 9\,\%. \tag{4.11}$$

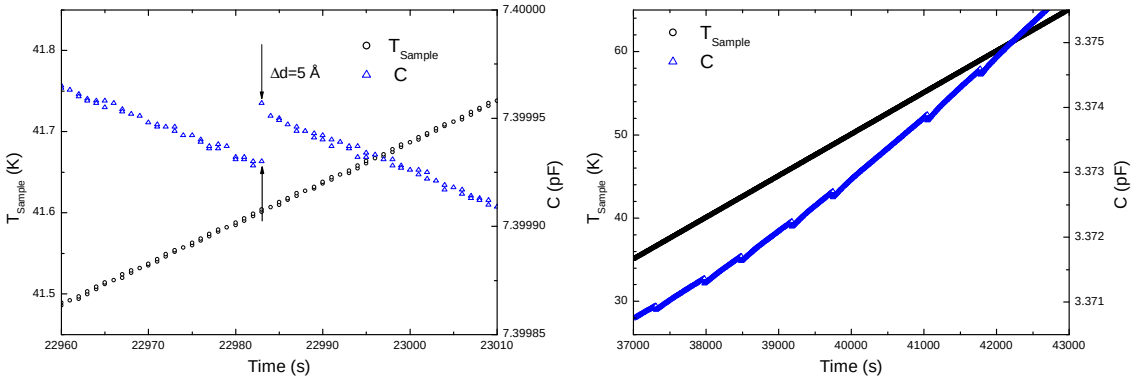

Figure 4.5: Left: Plot showing the sudden change in capacitance during a temperature sweep with a silver sample (3.99 mm in length). This behavior is also known as "glitch". Right: Plot showing a periodic occurrence of glitches during a measurement of a copper sample (4.02 mm in length). The occurrence of glitches is more frequent than in other measurements.

This shows that the guarding is probably not efficient, since the error stays in the same order of magnitude. The reason is, that compared with the overall dimensions, w is relatively large. Thus, the error caused by fringe effects is estimated to be in the range 1 % to 10 %.

The value of 4.8 changes only slightly during length changes in the micrometer range, which are the length changes encountered during our temperature sweeps from 5 K to 300 K for usual metals. With the overall compensation of the effect through the calibration at room temperature(see section 5.1), this contribution is therefore neglected for materials with $\Delta l/l$ in the range of 1×10^{-3}. This is in accordance with the findings of [38, 54].

4.4 Glitches / Friction Effects

The length changes detected within this experiment are in the sub-Ångstrom range. The surface roughness at the contact surfaces of sample, silver spacer and dilatometer is at best of the order of one micrometer. Temperature sweeps are thus often accompanied by hysteresis and friction effects caused by the relative movement of surfaces [8].

During this work, sudden changes in the capacitance during temperature changes were noticed. The capacitance jumps, but then continues smoothly. This is a well-documented effect and referred to as "glitch" [34, 74, 83, 84]. The origin for these effects is the relative movement of sample and dilatometer. The form of the jump suggest a stick-slip motion similar to the phenomenon seen in atomic force microscopy [85], which is caused by the friction between two contact surfaces. Fig. 4.5 shows glitches during a temperature sweep of a copper cylinder. The sample was made using a lathe instead of the procedure described in section 3.7. The more frequent occurrence of glitches can be explained by the rougher surface, which supports the theory of friction as the underlying process. The size of the

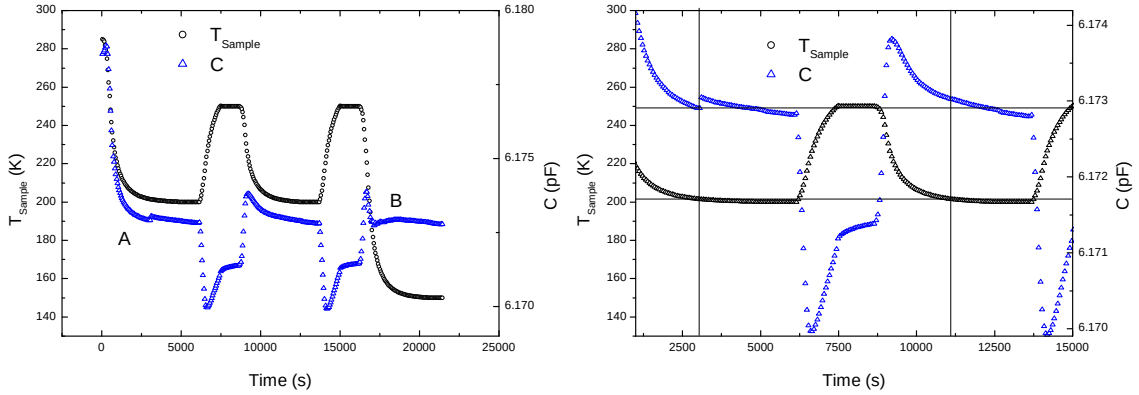

Figure 4.6: Left: Plot showing reproducibility errors (A,B) in the capacitance caused by friction effects during temperature steps. A is likely to be caused by friction between sample and cell. B shows an extreme example of a glitch. Right: Zoomed in area of the plot on the left for clarity

glitches is usually of the order of Å.

Glitches can cause reproducibility errors, since after the glitch, the capacitance and thus the length is not relative to the starting capacitance anymore, but to the starting capacitance plus the offset introduced by the glitch. Therefore, if they are of the order of 1 Å, they contribute an error of 1×10^{-7} in $\Delta l/l$. However, glitches can be easily identified in αas outliers. After their removal, α is integrated over the temperature resulting in a $\Delta l/l$ without major influences of glitches(see also 3.6).

Rapid cooling ($\gtrsim 3\,\mathrm{K\,min^{-1}}$) cycles were often accompanied by large glitches (see fig.3.9). This can be explained by different thermal contraction speeds of the different parts resulting in relative movement of the movable parts. The capacitance jumps reached up to $0.01\,\mathrm{pF} \mathrel{\hat{=}} 0.1\,\mu\mathrm{m}$. Thus fast temperature changes often lead to large reproducibility errors(see fig. 4.6).

4.5 Incorrect Spring Tension

The CuBe-washer used a as spring to hold the two dilatometers halves together can be tightened with different intensity. However, it is hard to quantify the exact tension to stay within the elastic regime of the washer. Fig. 4.8 gives a guideline how to accomplish an appropriate tension of the washer. An established technique is to turn the nut until it touches the washer and then tighten it further by approximately 3/4 turns. To investigate the implications of faulty spring tension, a test with a copper sample was made. In this case, the spring was extremely tightened to show the maximum influence of the spring. The capacitance curve showed more glitches than usual and spikes were visible (fig. 4.7). The spikes are a distinct property of this measurement. A possible explanation would be, that a higher normal force allows a new order of friction mechanisms that cause very short

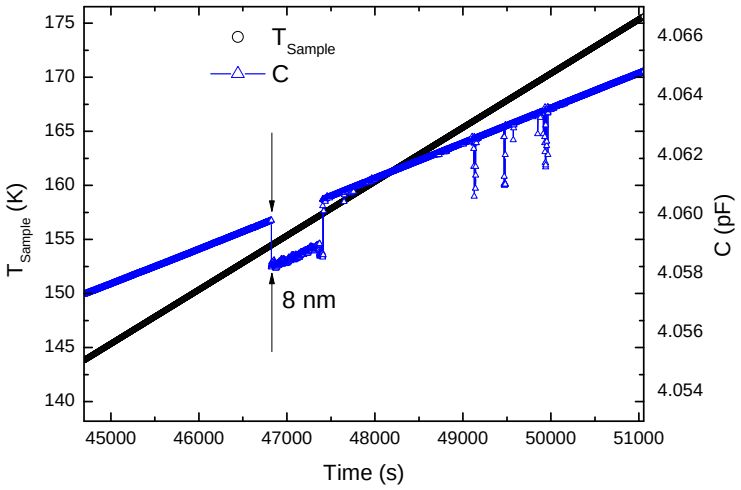

Figure 4.7: Plot showing features in the capacitance during a temperature sweep with an extremely tightened spring. Glitches occur more frequently and had larger jump sizes. Spikes are visible.

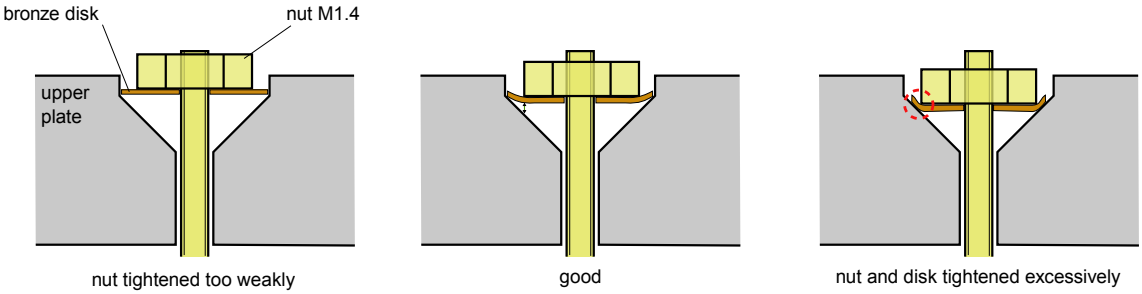

Figure 4.8: Schematic drawing showing a good practice for the required tension of the spring. Graphic by H. Müller [86].

glitches.

4.6 Thermal Gradients

Ideally, the temperature distribution within the cell and sample should be homogeneous at the point of measuring. However, since it is constantly heated, one has a constant heat flux and thus an unavoidable temperature gradient within the cell. In this section, the question is addressed how a non-uniform temperature distribution can influence the the measurement of the capacitance.

The thermal conduction equation reads

$$\frac{\partial T(\vec{r},t)}{\partial t} = a^2 \nabla^2 T(\vec{r},t) \quad \text{or in more physical terms} \quad \frac{\partial \vec{q}}{\partial t} = -\lambda \nabla T(\vec{r},t), \tag{4.12}$$

where $\dot{\vec{q}}$ is the heat flux, λ the heat conductivity and $T(\vec{r},t)$ the temperature distribution in space and time. $a^2 = \lambda/(c\rho)$ is a variable combining heat conductivity λ, specific heat

c and mass density ρ.

In order to estimate the influence of temperature gradients and to investigate the characteristic scales, a rod of length $l = 22\,\mathrm{mm}$ is assumed, which is the cell's diameter. It is heated at both sides with a constant heating rate k to model to heating by the heating cylinder around the cell. The initial and boundary conditions can be stated as

$$T(x,0) = 0 \quad \text{and} \quad T(0,t) = T(l,t) = kt \tag{4.13}$$

If a homogeneous and temperature-independent a is assumed, the solution of (eq. 4.12) to this problem is [87]

$$T(x,t) = -\int_0^t \int_0^l G(x, t-\tau, \xi) k \,\mathrm{d}\xi \mathrm{d}\tau \tag{4.14}$$

with the kernel

$$G(x,t,\xi) = \frac{2}{l} \sum_{n=1}^{\infty} \exp\left[-\left(\frac{an\pi}{l}\right)^2 t\right] \sin\frac{n\pi}{l} x \sin\frac{n\pi}{l}\xi. \tag{4.15}$$

The first harmonic ($n = 1$) dominates the solution:

$$T_1(x,t) = \frac{4kl^2}{a^2\pi^3}\left(\exp\left[-\frac{a^2\pi^2 t}{l^2}\right] - 1\right) \sin\left(\frac{\pi x}{l}\right). \tag{4.16}$$

The largest temperature difference is between the middle and the sides:

$$T_1(0,t) - T_1(l/2,t) = -\frac{4kl^2}{a^2\pi^3}\left(\exp\left[-\frac{a^2\pi^2 t}{l^2}\right] - 1\right), \tag{4.17}$$

The characteristic time scale (also known as relaxation time) is

$$\tau = \frac{l^2}{a^2} = \frac{l^2 c\rho}{\lambda}. \tag{4.18}$$

This determines roughly the time how fast a body thermalizes. At the starting temperature of a sweep ($\approx 5\,\mathrm{K}$) the relaxation time τ is low, since c is low and λ high (see fig. 4.9), thus the first term drops quickly. Now, $\dot{T}$ is not zero, but the gradient (eq. 4.17) is constant. This situation often called quasi-stationary heating. This shows, that a temperature sweep with constant rate is preferable, since it can be seen from eq. 4.17 that the gradient is dependent on the sweep rate. Using literature data of silver for c [88], ρ [89] and λ [90] and assuming a constant l and ρ, the relaxation time (eq. 4.18) is calculated within the temperature range $5\,\mathrm{K}$ to $300\,\mathrm{K}$ (see fig. 4.9). The results show $\tau < 3\,\mathrm{s}$. Assuming $\tau = 3\,\mathrm{s}$ at high temperatures, $t \gg \tau$ and a typical sweep rate of $k = 0.3\,\mathrm{K\,min^{-1}}$, the temperature gradient based on eq. 4.17 is determined to be $\Delta T = 4k\tau/\pi^3 = 2\,\mathrm{mK}$. Since τ is only changing slightly at high temperatures, quasi-stationarity is likely to occur.

However, the relaxation time is suspected to be higher, since the system to be thermalized

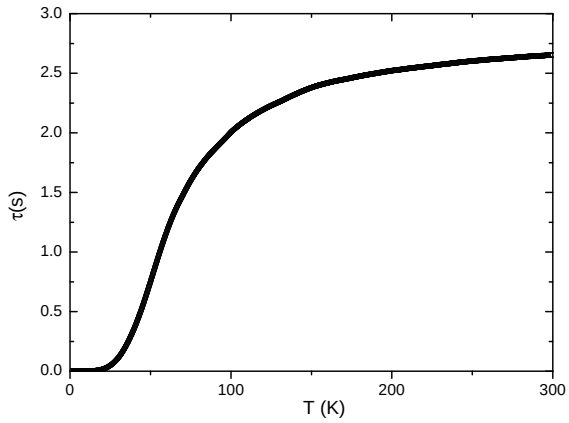

Figure 4.9: Relaxation time τ for a silver rod with length $l = 22\,\mathrm{mm}$ as a model for the dilatometer cell (see text for details)

is not completely silver (brass, sapphire,sample) and is likely to be larger than assumed in this 1D-model. Surrounding parts as for example the brass part holding the cell have to be included[4].

A temperature sweep made with faulty PID-settings produced temperature oscillations with a steady periodicity (see fig. 4.10). However, the resulting data allow estimates based on the above-mentioned model. The growing hysteresis with temperature indicates that the relaxation time is greater than the half of the periodic time of the temperature oscillation $\approx 60\,\mathrm{s}$. To account for this, the relaxation time in our 1D-model is generously increased the by a factor of 50 to $\tau = 150\,\mathrm{s}$. The maximum gradient based on eq. 4.17 would be $\Delta T = 100\,\mathrm{mK}$. This introduces errors of approximately $0.1\,\mathrm{K} \times \alpha \approx 1 \times 10^{-6}$ in $\Delta l/l$ during a quasi-stationary heating at high temperatures. This constitutes an error below 1 %, if one assumes a typical $\Delta l/l$ of 1×10^{-3}. These findings are in agreement with Schefzyk who found an error of $\pm 20\,\text{Å}$ when measuring length changes with his cell at high temperatures [34]. However, these results are only partially comparable due to the different sizes of the cells.

The error should be reproducible and thus only affecting the accuracy and not the precision. As for all systematic errors, the calibration against silver reduces this error, if the calibration sample is heated at the same rate as the unknown sample.

To yield better quantitative and exact results (a 1D model can only give rough estimates), a more detailed experimental study is recommended. However, the data shown in fig. 5.2 suggests that thermal gradients are not large source of error.

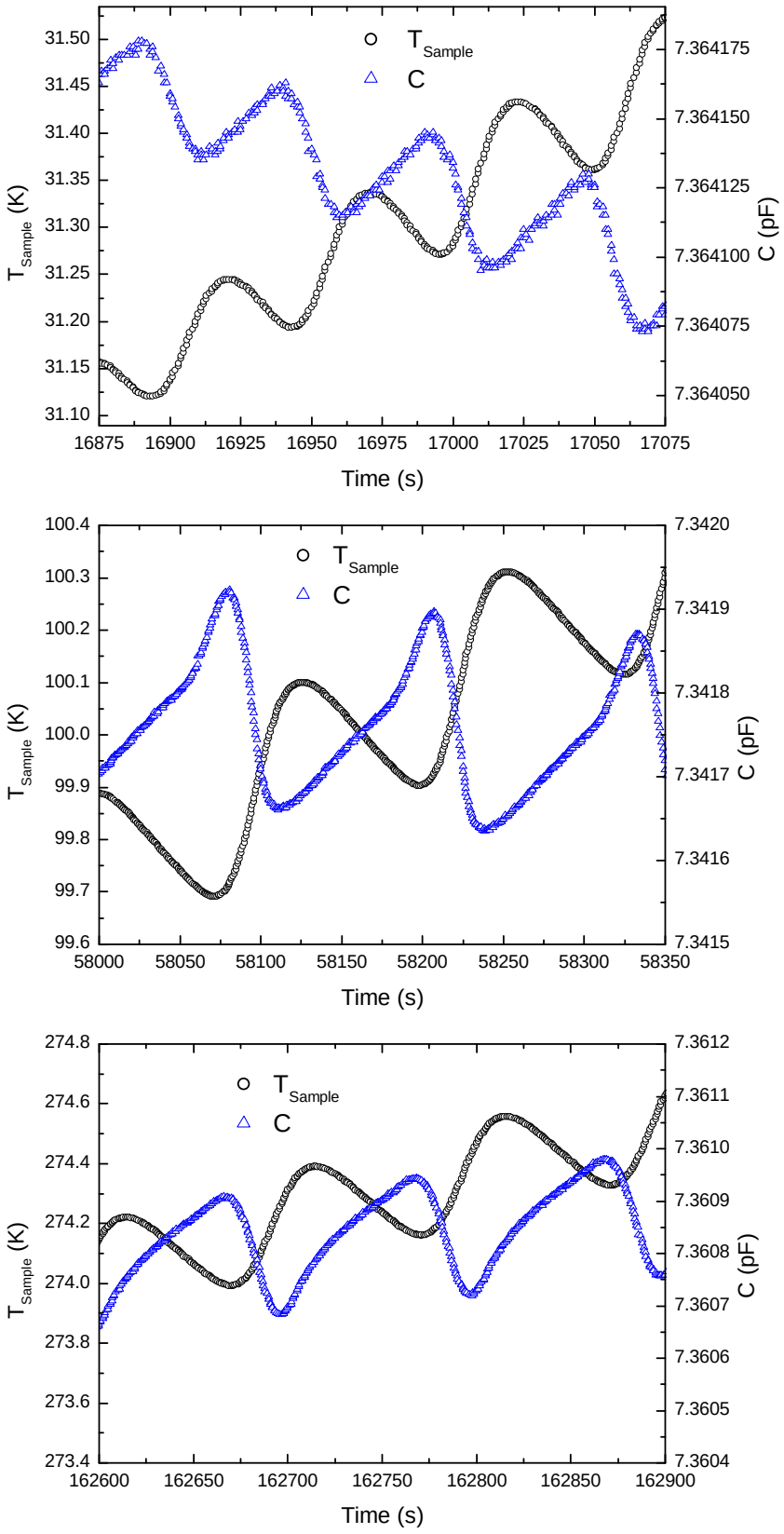

Figure 4.10: Sample temperature vs. Capacitance during a temperature sweep with a rate of $0.1\,\mathrm{K\,min^{-1}}$ with a silver sample at 30 K (top) 100 K (middle) and 270 K (bottom). The oscillations are caused by non-ideal PID-controller-settings.

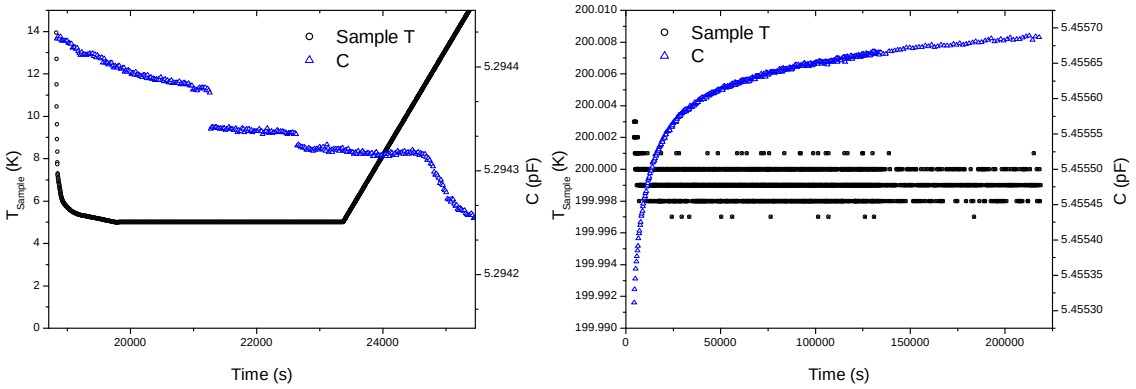

Figure 4.11: Left: Aluminum sample (2.27 mm in length) held constant at 5 K. The step-like features are glitches. Neglecting these yields an overall capacitance change of $\approx 1 \times 10^{-4}$ pF $\hat{=}$ 4 nm. Right: Plot showing the drift in capacitance during a long-term (> 59.5 h) temperature stability test at 200 K. The overall capacitance change of $\approx 4 \times 10^{-4}$ pF corresponds to a length change of ≈ 0.01 µm.

4.7 Creep / Drift

Materials deform slowly if they are subjected to constant load. This behavior is called creep. It is attributed to thermal movement of dislocations within the material [91, 92]. The time dependence of creep strain can be modeled by [91]

$$\epsilon = a \ln \gamma t + 1 \tag{4.19}$$

where

$$a(T) \begin{cases} \to const & T \to 0 \\ \propto T & T \gtrsim 10\,\mathrm{K} \\ \propto T^2 & T \lesssim 10\,\mathrm{K} \end{cases}. \tag{4.20}$$

During a long-term stability test at 200 K with a aluminum sample (2.27 mm in length), an approximately logarithmic time dependence of the capacitance was observed although the temperature was held constant within ±3 mK (see fig. 4.11). Eq. 4.19 and the large time scale suggest creep as an underlying process. If the change in capacitance change would correspond to thermal expansion, this would yield a $\Delta T \approx 0.1$ K over a time of 59.5 h. The time scales for thermal relaxation are much shorter (see section 4.6), which suggests that this behavior is not caused by thermal gradients.

Fig. 4.11 shows the same sample held constant at 5 K after cooling. Contrary to the drift at 200 K, the drift is downward. Thermal gradients relax very quickly at these temperatures (see fig. 4.9) and the capacitance difference $\approx 1 \times 10^{-4}$ pF would correspond to a temperature change of $\approx$ 20 K within the sample, since the thermal expansion is

[4] Brass has a thermal conductivity approximately 10 times lower than copper and silver [60].

low at these temperatures, hence this effect is as well due to creep. Such gradients are unrealistic at these temperatures, hence this effect has to be caused by other mechanisms than thermal expansion. The glitch in 4.11 is evidence for relative motion between the cell and the sample. A drift of, for example, the standard capacitance within capacitance bridge 3.2 is unlikely, thus a process within the cell must be responsible. One may speculate that the delayed response of the capacitance to the temperature change is attributed to the low thermal expansion at 5 K. The thermal expansion is typically low ($\alpha \approx 1 \times 10^{-9}\,\mathrm{K}^{-1}$) and the resolution of the cell is 5×10^{-8} in $\Delta l/l$ (see section 5.10).

In the cell, there are multiple parts which are under load: The plates are screwed within the housing and pressed on sapphire and the CuBe-spring is under constant tension. Since the cell consists of materials with different thermal expansion coefficients (silver, brass, sapphire), tension can also build up during temperature changes. If a load is removed, materials also creep back. Schefzyk gives an overview over this effect [34]. As indicated by the different signs of the capacitance change seen in fig. 4.11, the creep behavior is dependent on the thermal history of a material. It is hard to address this problem quantitatively. However, one can give an error estimate based on the data shown in (fig. 4.11):

If one takes the steepest point in fig. 4.11, the maximum creep rate at 200 K can be stated as $d_{\mathrm{creep}} = 3\,\mathrm{Å\,min}^{-1}$ Assuming the temperature dependencies of d_{creep} shown in (eq. 4.19), $4.5\,\mathrm{Å\,min}^{-1}$ at 300 K can be estimated. Interpolation of the data and calculating the relative length change using one temperature sweep period (≈ 15 h at $0.3\,\mathrm{K\,min}^{-1}$) as the longest timescale possible results in a contribution of the order 1×10^{-6} to $\Delta l/l$. Since relative length changes are usually $\approx 1 \times 10^{-3}$, this corresponds to a relative error of 1×10^{-3}.

Annealing procedures might provide a way to reduce stress within the material. White's original cell was annealed [6] before use, but there is no investigation whether this had an effect. However, degassing silver can have an effect of some percent in α [13].

4.8 Sample and Silver Spacer Length

During the preparation of measurement, two lengths are measured with a micrometer screw: The length of the sample and the length of the silver spacer. The measuring error is determined by the machining process during the production of the sample and the silver spacer. The silver spacer was manufactured on a lathe yielding errors in the 1×10^{-2} mm range. The samples were cut with a diamond saw afflicting an error $< 1 \times 10^{-2}$ mm.

These errors afflict the resulting $\Delta l/l$ in two ways (eq. 3.14): l_s is in the denominator, thus directly inflicting an relative error on the result. However, with an error below 1×10^{-2} mm in l_S, this does not yield an error of more than 1 % in $\Delta l/l$.

In eq. 3.15 it is assumed that the sum of the length of sample and the sample spacer matches the length of the silver spacer used in the cell effect measurement. The error in

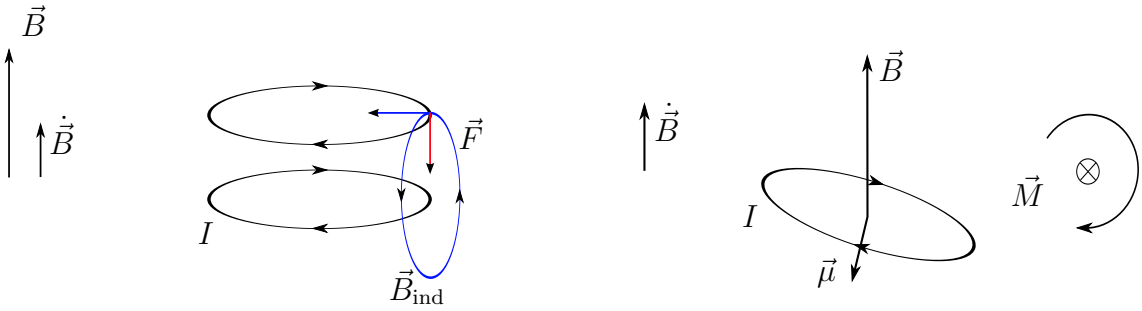

Figure 4.12: Left: Schematic drawing representing the situation if the plates are perfectly aligned with the magnetic field B. The resulting force (red) yields to an attraction of the plates. Right: Schematic drawing showing the situation of a tilted plane. Tilted eddy currents result in a torque $\vec{M}$. Its direction is dependent on the direction of the magnetic field and its time dependence.

the length of the silver spacer afflicts then the accuracy of $\Delta l/l$:

$$\Delta d_{\text{cell-length-silver}} - \Delta d_{\text{silver-piece}} = \frac{\Delta d_{\text{sample-length-silver}}}{l_S} \pm \frac{\Delta l_{\text{err}} (\Delta l/l)_{\text{Ag}}}{l_S} \tag{4.21}$$

With the expansion of silver being in the range 1×10^{-3}, the length error being of the order $1 \times 10^{-2}\,\text{mm}$, this introduces an error around $1\,\%$ in $\Delta l/l$ for millimeter sample lengths.

4.9 Magnetic Field Effects

Since the external magnetic fields used during the experiments can reach high field strengths (up to $17\,\text{T}$), it is worthwhile analyzing possible effects on the cell. Magnetostriction measurements are conducted at low temperatures via linear magnetic field sweeps. Consisting of silver, the cell has a high conductivity and low heat capacity making it in principle vulnerable to the effects of eddy currents.

In order to estimate the relative orders of magnitude of effect caused by an external magnetic field, the two dilatometer halves are modeled as two wire loops with the radius $R = 22\,\text{mm}$ and distance $z = 0.1\,\text{mm}$. The induced voltage is then

$$U_{\text{ind}} = -\dot{\Phi} = -\dot{\vec{B}}\vec{A}. \tag{4.22}$$

The specific resistance of silver is $\rho \approx 1 \times 10^{-9}\,\Omega\,\text{m}$ [89]. Using a cross-section of $a = 5\,\text{mm}^2$, a length of $l = 2\pi R$ and $\dot{B} = 1\,\text{T}\,\text{min}^{-1}$, one yields

$$P = \frac{U}{R^2} = \frac{\dot{B}A}{\rho(l/a)} = 3 \times 10^{-6}\,\text{W}. \tag{4.23}$$

The heat capacity of the dilatometer ($m \approx 40\,\text{g}$) at $5\,\text{K}$ is $C = cm = 9 \times 10^{-3}\,\text{J}\,\text{K}^{-1}$ [89].

Thus the temperature change is

$$\frac{P}{C} = 3 \times 10^{-4}\,\mathrm{K\,s^{-1}}. \tag{4.24}$$

This indicates, that the temperature instability caused by eddy currents is manageable by the temperature controller.

The magnetic field of a single loop along its axis z amounts to [93]

$$B_z = \frac{\mu_0 I \pi R^2}{2\pi \left(z^2 + R^2\right)^{3/2}} \overset{z \ll R}{\approx} \frac{\mu_0 I}{2R}. \tag{4.25}$$

With $r \approx 0.1\,\mathrm{mm}$ being the distance between the loops, the Lorentz force acting on one loop is

$$F = \int I \left(\mathrm{d}\vec{l} \times \vec{B}\right) = 2\pi R B I = \mu I^2 \frac{R}{r} = 60\,\mu\mathrm{N} \tag{4.26}$$

This effect always yields an attracting force between the plates, since the eddy currents of the two loops always have the same direction relative to each other. An attracting force should yield smaller effects than a force, which is opening the dilatometer halves, since the sample and silver spacer prevent a closing of the halves. The magnitude is only dependent on the sweep rate $\dot{B}$.

Silver is paramagnetic. Its mass susceptibility is $\chi/\rho = 2.3 \times 10^{-9}\,\mathrm{m^3/kg}$. A force may act on the bulk silver, if it is affected by an magnetic field gradient. Being a paramagnet, silver is pulled into the direction of the higher field density. Naturally, there is an magnetic field gradient along the magnet axis. Assuming the top field of 15 T, the maximum vertical B-field gradient $\Delta B/\Delta x \approx 15\,\mathrm{T}(0.0006/2\,\mathrm{mm}) = 0.005\,\mathrm{T\,mm^{-1}}$ [63]. The force on the whole dilatometer would be [60]:

$$F = \frac{\chi}{\rho}\frac{B}{\mu}\frac{\Delta B}{\Delta x} \approx 5\,\mathrm{mN} \tag{4.27}$$

The eddy currents create an additional magnetic dipole moment $\mu = I\vec{A}$. This dipole moment and the magnetic field gradient yield then a force of

$$\mu \frac{\Delta B}{\Delta x} = 0.8\,\mathrm{mN} \tag{4.28}$$

Since the direction of μ depends on $\dot{B}$ and ∇B on the direction of B, this force is also changing its direction depending on the directions of B and $\dot{B}$.

If the plates are tilted against the field, the torque estimated via the current loop model is

$$|\vec{M}| = |\vec{\mu} \times \vec{B}| = IA \sin\theta \cos\theta B. \tag{4.29}$$

Since the loop is tilted, the magnetic flux is reduced via $\cos\theta$, where θ is the angle between

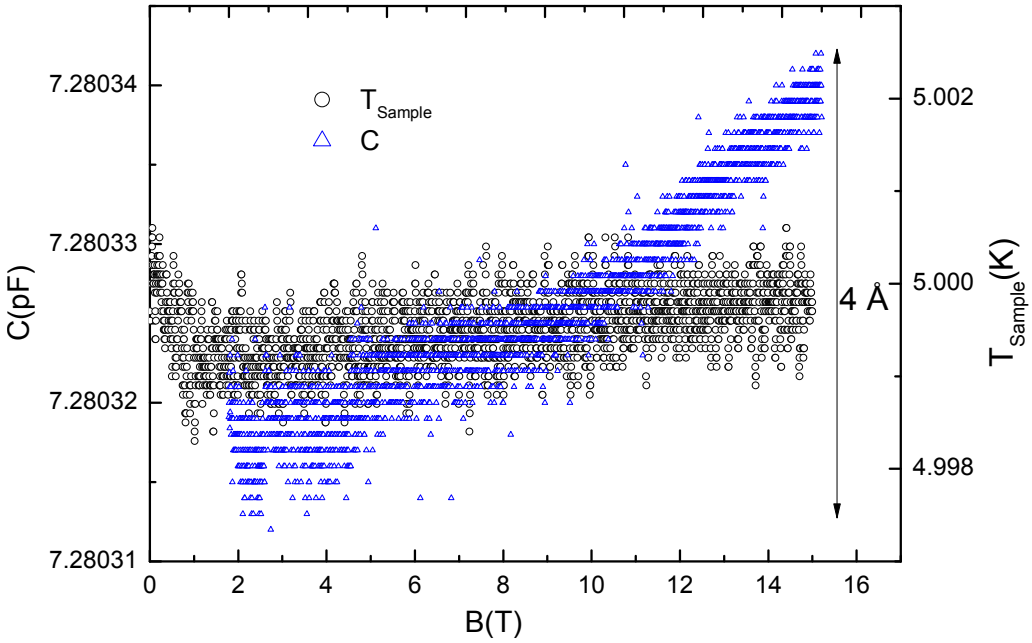

Figure 4.13: Field sweep with silver sample with increasing magnetic field, stabilized at 5 K. Sampling effects caused by the resolution limit of the capacitance bridge are visible.

the surface area vector and the magnetic field B. If one assumes a maximum field $B = 15\,\mathrm{T}$ and and a moderate angle of $\theta = 0.5°$ (the natural tilt of the upper half is around 0.1°), the force at one end of the loop would be

$$F = M/R = 5\,\mathrm{mN}. \tag{4.30}$$

The dependencies of eq. 4.29 indicate that this is the most unpredictable effect. Whether this effect is opening or closing the dilatometer depends on the field direction, the time dependence of the field and of the orientation of the tilted surfaces relative to the magnetic field.

In order to test for the influences described above, a measurement of a silver sample is performed. The oscillatory magnetostriction observed of silver is $\lambda \approx 1 \times 10^{-8}$ to 1×10^{-9} [94], which is close to the overall resolution of our experiment and thus suitable to measure unwanted systematic errors.

This measurement was done with the magnetic field pointing downward in fig. 3.5 and positive sweep rate. The capacitance rises leading to the conclusion that the resulting force pushes the plates together. Since the effect is dependent on the field strength, it cannot be caused by the interaction of eddy current flowing within the plates. To isolate the exact source of error, additional experiments with varying tilt angle, magnetic field sweep rate and negative $\dot{B}$ are recommended.

5 Calibration Measurements

5.1 Room-Temperature Calibration

From section 4.3, it becomes clear, that fringe effects have to be corrected. Additionally, errors from manufacturing processes can be expected, thus making a replacement of the geometrical "blueprint" dimensions by effective dimensions necessary. From 3.4.2 one can estimate the extent of the corrections needed:

$$C_{\text{uncorrected}} = \frac{\epsilon A}{k} \quad \Rightarrow \quad \frac{C_{\text{measured}} - C_{\text{uncorrected}}}{C_{\text{uncorrected}}} \approx 30\,\% \tag{5.1}$$

The variable $k = 0.19(2)\,\text{mm}$ denotes the optically measured distance between the plates. In order to obtain the effective parameters, the model of Eq. 3.10 is cross checked against the actual measured capacitance using the device depicted in fig. 5.1. The dilatometer is fixed to micrometer screw which pushes a tip into the dilatometer. The halves of the cell are then pushed apart by turning the micrometer. While stepwisely opening the dilatometer in this fashion, the reading on the micrometer d_μ and the capacitance C is noted. The process is then reversed and the value for C and l_μ are again recorded (see fig. 5.2).

Hysteresis effects can be attributed to relative motion at the contact surfaces and thermal expansion of the tip[1]. The downturn at (A) can be explained by touching surfaces of the housing within the dilatometer (see fig 3.5). The fact, that the plates do not short-circuit

	Real(mm)	Effective(mm)
r_i	3.0	2.7
r_o	6.0	6.2
b	9.8	9.8

Table 5.1: Real dimensions of the cell as they would be measured (see fig. 3.5) and effective parameters determined from calibration.

[1]The tip is several cm in length, $\alpha \approx 1 \times 10^{-5}\,\text{K}^{-1}$, thus temperature changes of 0.1 K can cause length changes of 0.1 µm.

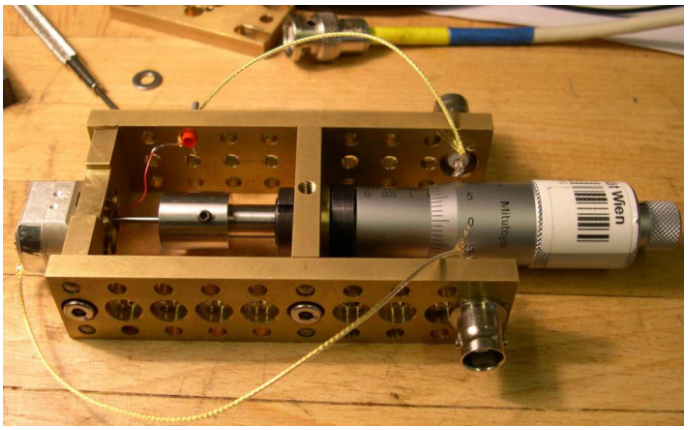

Figure 5.1: Photograph showing the device to perform a room-temperature check to verify the mathematical model for translating capacitance change to a plate distance change. From [51].

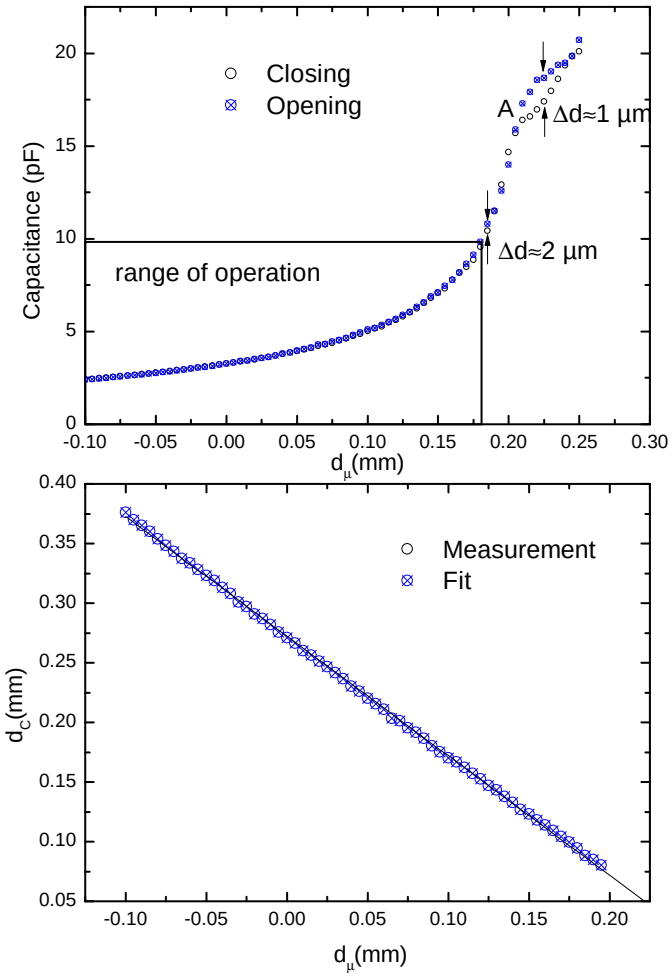

Figure 5.2: Top: Capacitance vs. Micrometer reading is shown for opening and closing dilatometer halves. The capacitance range, in which the dilatometer is operated in the following measurements is depicted. Distances corresponding to the capacitance differences are denoted. Bottom: Calculated distance vs. the micrometer with effective parameters shown in tab. 5.1 and linear fit to the data.

at this point, shows good surface quality, since plate distances in the order of 10 µm can be maintained without electrical contact between the plates.

Using $C(d_\mu)$, the gap width d_c according to eq. 3.10 is calculated and compared with d_μ within the range denoted in fig. 5.2, since deviations from the model of eq. 3.10 are observed. The values corresponding to an opening of the dilatometer are then analyzed, since thermal expansion measurements are conducted via heating the dilatometer, which corresponds mostly to an opening of the cell. In order to find the best value for the effective area, r_o, r_i and b are varied and $d_c(d_\mu)$ fitted with $f(x) = a + mx$ for each parameter set. Ideally, the function $d_c(d_\mu)$ should be linear with a slope of -1. A variation of b caused slope changes less than 1 %. Thus, b is held fixed at the original value 9.8 mm.

The variation of r_o and r_i shows best results for r_o in the range 6 mm to 6.5 mm and r_i in the range 2.5 mm to 3.5 mm.

Fig. 5.3 shows the deviations of the slope Δm relative to -1 with varying parameters in these ranges. Based on these findings, the parameters presented in table 5.1 are chosen. In order to check the parameters against the calibration measurements of copper and aluminum, the quantity

$$z = \sum_i^N |(\Delta l/l)_{i,\text{measured}} - (\Delta l/l)_{i,\text{literature}}| / \sum_i^N (\Delta l/l)_{i,\text{literature}} \tag{5.2}$$

is defined, where the sum goes over all literature data points. This gives a quantity ranging in the same order of magnitude as Δm. Using the data of aluminum and copper (see section 5.10 and 5.3), z is calculated and added to Δm yielding

$$X = \Delta m + z_{\text{Cu}} + z_{\text{Al}}. \tag{5.3}$$

Thus a low X indicates a better calibration. Fig. 5.3 shows X depending on r_o and r_i. Points neighboring $r_o = 6.2$ mm and $r_i = 2.7$ mm yield a slightly higher X. Thus the parameter set from table 5.1 yields also a good agreement of the measurements of copper and aluminum with literature data and is thus used. In this case, $\Delta m = 0.3$ %. Using the new effective parameters and calculating $C = \epsilon A/k$ yields an agreement with C_{measured}, if A has an error of about 4 %. However, the error in k is suspected to be larger, since it was only measured at the fringes of the dilatometer and an additional error of some percent ($\hat{=}$ micrometer) could be explained by surface imperfections. Therefore, the error of the obtained effective area is assumed to be in the order of magnitude of (1 %).

It is also noted that this error like all systematic errors is reduced by the calibration against silver. Since the effective area appears in the cell effect measurement and the measured data (see eq. 3.14), the error is proportional to $\Delta d_{\text{measured}} - \Delta d_{\text{Ag}}$.

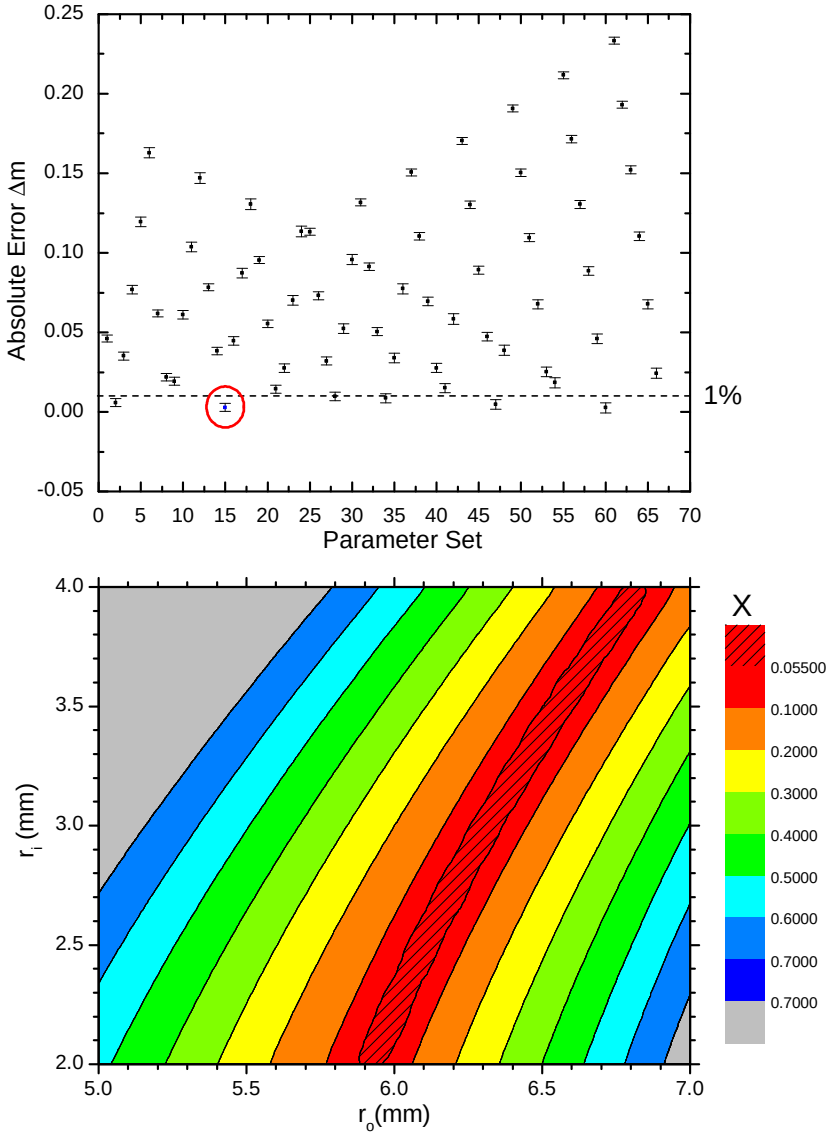

Figure 5.3: Top: Difference to the ideal value -1 of the slope of a linear fit to $d_C(d_\mu)$ with different parameter sets (r_o and r_i are varied). The parameter set yielding the best results is marked with a red circle (corresponds to the effective values in tab. 5.1). Bottom: Contour plot showing the combined error of room-temperature calibration and calibration measurements with copper and aluminum. A lower X indicates better choice of parameters(see text for details).

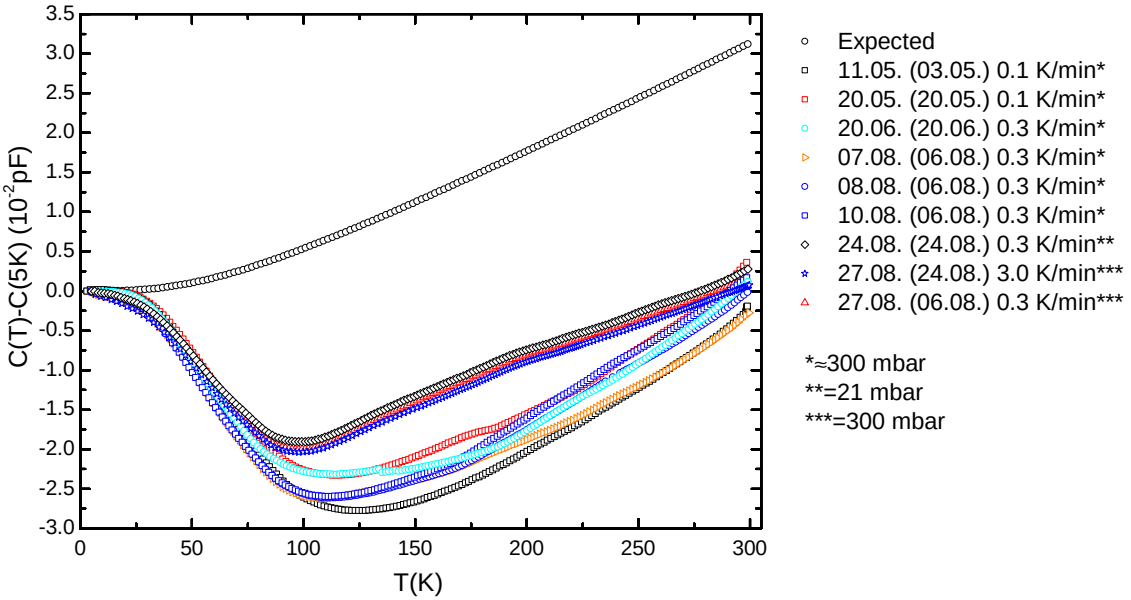

Figure 5.4: Expected capacitance change of a silver sample using eq. 3.10 and measured capacitance changes. The dates in brackets represent the date of the insertion of the sample rod into the cryostat. The data have been acquired using different helium exchange gas pressures of 21 mbar and 300 mbar. The pressure for some runs could only be estimated (see text for details).

5.2 Cell Effect

In order to measure the cell effect(see section 3.1), the thermal expansion of the cell itself, a measurement with a high-purity (99.995 %) silver sample ($l = 3.99\,\mathrm{mm}$) is performed. Fig. 5.4 shows the expected capacitance behavior based on eq. 3.10[2]and the real temperature dependence of the capacitance during one cell effect measurement. Figure 5.5 shows the relative length change of several cell effect measurements. The overall reproducibility at high temperatures is poor (up to $\approx 55\,\%$ difference). However, it can be noted that the difference between two measurements is larger, if the cell has been dismounted between measurements. This indicates a source of error linked to mechanical reasons and not thermal behavior of the cell. The length changes obtained using faster and slower sweep rates exhibit similar non-reproducible effects, which supports this hypothesis.

Figure 5.5 also shows the different exchange gas pressures used during the setups. Most of the measurements were conducted by letting a defined volume of helium expand in the evacuated tube, which yields approximately a 300 mbar pressure. To yield more precise value, a pressure gauge was used in later runs. The measurements performed on 27.08 and 24.08. yield a relative good reproducibility, although different exchange gas pressures and the same sweep rates were used. This indicates, that different exchange gas pressures

[2]For this calculation, $d^\star(T) = d(T)$ has to be used, since the the expansion of silver is in fact changing the capacitance. However, when translating C to d to obtain the cell effect, this behavior is regarded as a non-cell-effect and thus corrected (see section 3.1).

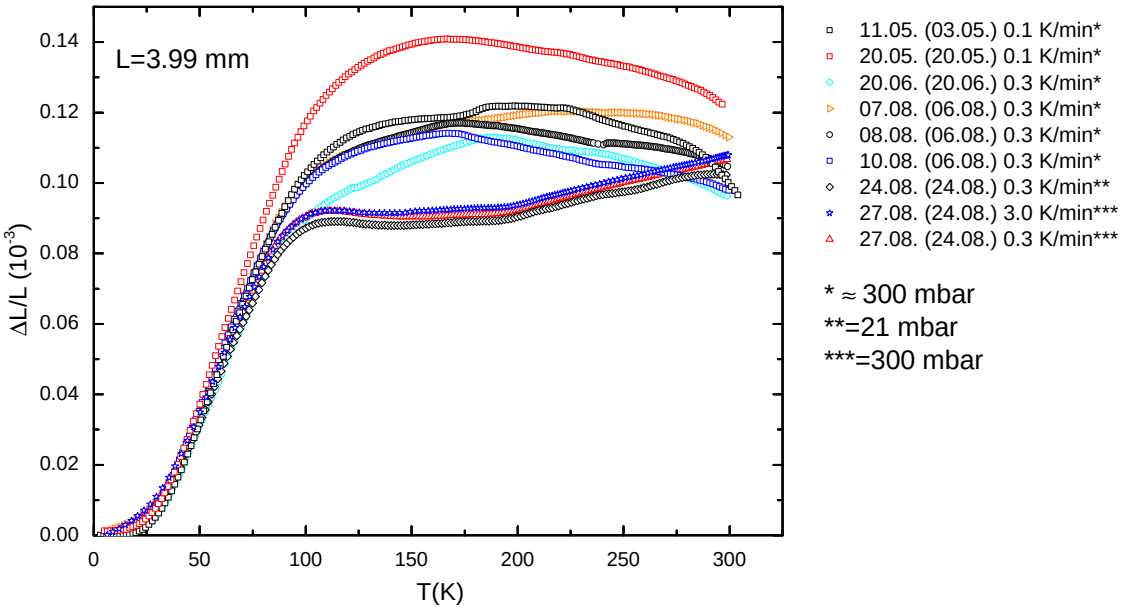

Figure 5.5: Relative length changes of the same silver sample. The dates in brackets denote the date of the insertion of the sample rod into the cryostat. The data have been obtained using different helium exchange gas pressures of 21 mbar and 300 mbar, whereas the pressure for some measurements can only be estimated (see text).

and residual gases effects can be assumed to play only a minor role (see also section 4.1). However, the error arising from this non-reproducibility does not propagate entirely to the quantity to be measurand. Since the measured value is a sum of cell effect and sample signal, the relative size determines to what extent the error of the cell effect propagates to the result. In addition, the size of the difference of the cell effect and the measured gap change has to be considered. The larger it is, the smaller the influence of the reproducibility error of the cell effect. This can be inferred from eq. 3.15

$$\begin{aligned}\frac{\Delta d_{\text{sample}}}{l_{\text{sample}}} &= \frac{\Delta d_{\text{measured}} - \Delta d_{\text{Ag}}}{l_{\text{sample}}} + \frac{\Delta l_{\text{Ag}}}{l} \\ &= \frac{(\Delta d_{\text{sample}} + \Delta d^{(1)}_{\text{Cell}} + \Delta d_{\text{Ag-Spacer}}) - (\Delta d^{(2)}_{\text{Ag}} + \Delta d_{\text{cell-length silver}})}{l_{\text{sample}}} + \frac{\Delta l_{\text{Ag}}}{l},\end{aligned} \tag{5.4}$$

where $\Delta d^{(1)}_{\text{Ag}}$ and $\Delta d^{(2)}_{\text{Ag}}$ denote gap changes caused by different cell effect behavior. This restricts our samples to materials with at least gap changes greater than the cell effect sample in order to achieve a reasonable reproducibility in $\Delta l/l$. A relative length change of the order of 1×10^{-3} is required to reduce the influence of the cell effect to the order of 1 %. Many solids fulfill this requirement. However, the non-reproducibility of the derivative of the cell effect and its overall non-smooth behavior creates undesired features in the thermal expansion coefficient (see e.g. section 5.3). The search for the origin of

these effects posed one of the largest challenges of the experimental setup (see sections 5.3 and 5.10).

In order to obtain smooth thermal expansion coefficient curves, further investigation is needed in order to improve the quality of the cell effect. Since the interplay of the thermal expansion of all parts causes the cell effect and the non-reproducibility occurs on a sub-micron level, the search for a cause for the poor reproducibility and non-smoothness of the cell effect is complex. Many workers in the field of capacitive dilatometry faced similar issues. Although extensively studied, the complexity of the cell effect often prohibits a clear and systematic extraction of its sources[3]. However, one of the following effects may give rise to a non-reproducibility and non-smoothness of the cell-effect:

Electrical Contacts The electrical connection of the cell to the coaxial cable leading to the capacitance bridge is achieved by using cable shoes (see fig. 3.11), which are clamped to the screws fixing the capacitor plates. During fixing the cable shoes (this has to be done after every reinsertion), the screws could be accidentally turned and thus the position of the plates could change. A replacement of the clamp contact with cable shoes by direct soldering is recommended.

Cone Bearings The contact surface, where the cone bearings stick into the upper dilatometer half was altered during the grinding process (see 3.4.1). Burrs formed during this process could cause a non-smooth behavior similar to glitches during the expansion of the cell.

Eccentric Screws Eccentric screws are located below the cone bearings, which were originally included into the design to allow fast adjustment of the cone bearings. A cryotape was put on the screw heads to prevent moving. However, this tape was removed and attached several times and it was noticed that the stability of the screw was poor when not fixed with the tape. Therefore, a slight movement of the screws during dismounting and mounting of the cell could happen and thus alter properties of the cell.

Spring Tension The tension of the CuBe spring washer is not well reproducible, since it can just be estimated based on the turns of the nut on top of the washer (see fig. 4.8). A more quantitative approach could lead to insights whether the properties of the spring have an effect on the reproducibility.

5.3 Copper

In order to test the performance of the dilatometer, a test with copper, a substance with well-known properties, is conducted. The sample corresponds to the NIST standard reference material 736 [95] with a length of $l = 3.04\,\mathrm{mm}$. The relative length change data

[3]For example, Auweiler [41] and Baier [43] struggled also with non-reproducible cell effects above ca. 100 K, but despite ample research, no distinct source of the cell effect could be found.

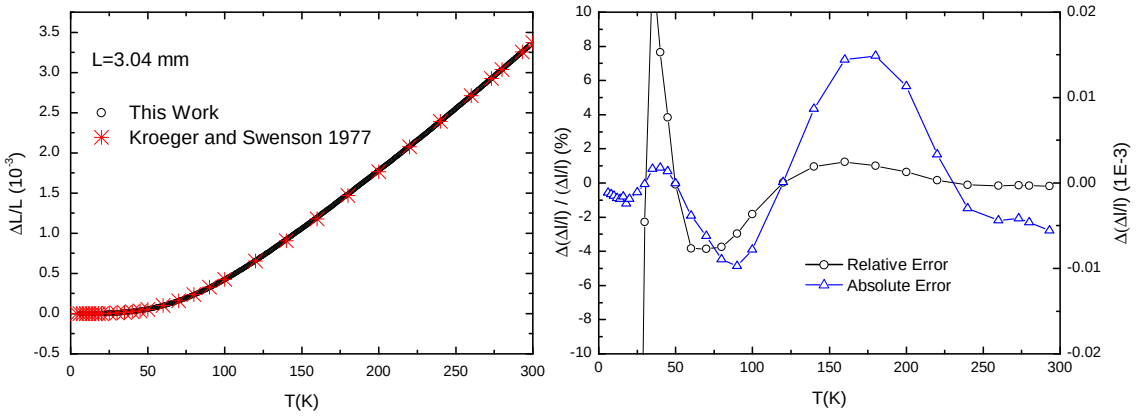

Figure 5.6: Left: Relative length change of copper in comparison with literature data. Right: Absolute and relative error of the relative length change compared literature data [37].

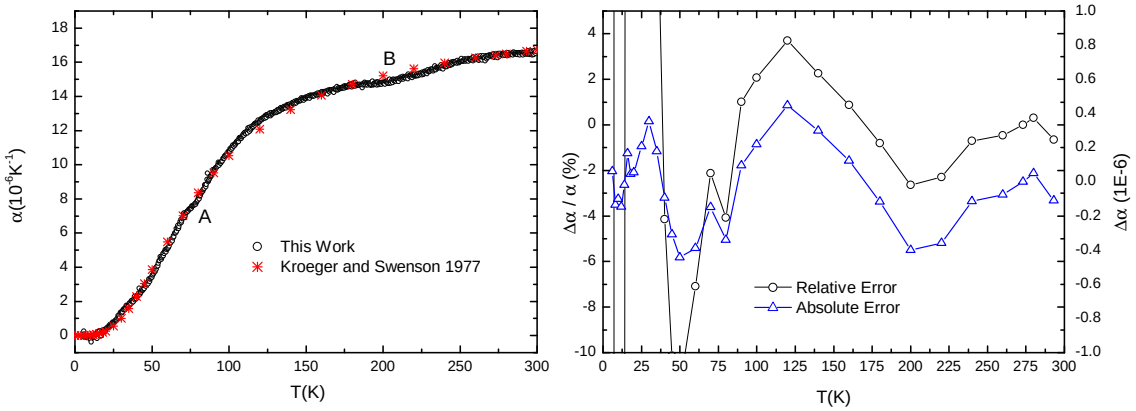

Figure 5.7: Left: Linear thermal expansion coefficient of copper. The two features A and B denote regions, where the measured values deviate significantly from the smooth behavior of the literature values. Right: Absolute and relative error of the linear thermal expansion coefficient compared with literature data [37].

matches the literature data of Kroeger and Swenson well [37][4](see fig. 5.6). The errors range from $-4\,\%$ to $4\,\%$. The relative error at low temperatures is high since differences boost systematic errors, which are expected to be large, since gap change caused by the cell effect lies in the same order of magnitude as the gap change caused by the copper sample itself.

The thermal expansion coefficient shows a good agreement with the literature data of Kroeger and Swenson [37], too. The relative errors are below $4\,\%$ at high temperatures, which is remarkable, since one expects an enhancement of the error by differentiating (see section 4.2). At low temperatures, the relative errors diverge for the same reasons as in the relative length change.

[4]The measurements of Kroeger and Swenson are performed with an absolute dilatometer yielding high accuracy (see fig. 3.3).

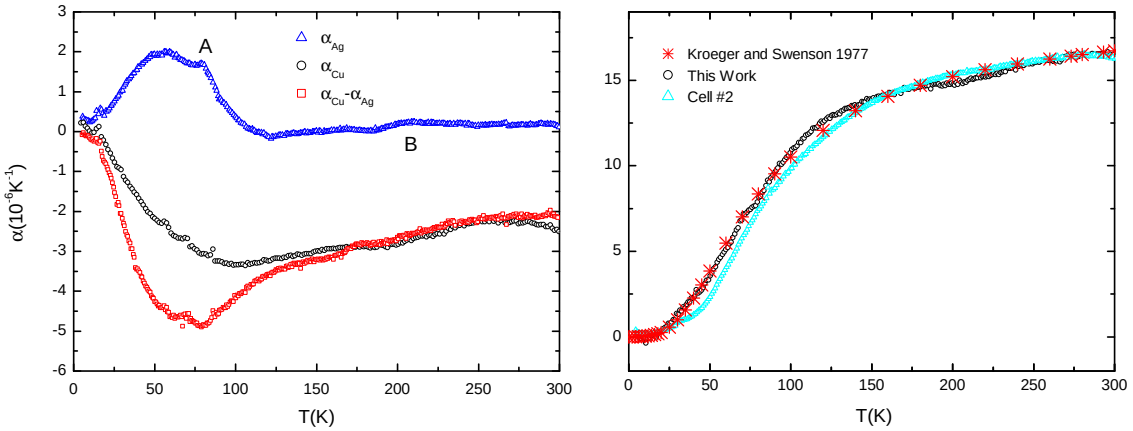

Figure 5.8: Left: The first two terms of eq. 5.5 for copper are shown. The features A and B denote non-smooth features (see 5.7). Right: Comparison with different cell sharing the same design.

Fig. 5.7 shows two regions A and B where the curve significantly deviates from a smooth behavior of the literature values. According to eq. 3.14 α splits up in the following terms:

$$\alpha(T) = \underbrace{\frac{d}{dT}\left(\frac{\Delta l}{l}\right)_{\text{measured}}}_{\alpha_{\text{Cu}}} - \underbrace{\frac{d}{dT}\left(\frac{\Delta l}{l}\right)_{\text{Ag}}}_{\alpha_{\text{Ag}}} + \alpha_{\text{Ag-Lit}}(T) \tag{5.5}$$

Fig. 5.8 shows the first two terms separately and their difference. It can be clearly seen, that feature A has its origin in the cell effect measurement. The feature in B appears in both terms, but it is not canceled well, which is assumed to be related to the poor reproducibility of the cell effect at high temperatures (see fig. 5.5).

In order to quantify the reproducibility of measurand, one measurement of the same copper sample with a different cell is compared with the obtained data[5](see fig. 5.8). The device shares the same design with the dilatometer presented in this work. Since the cell effect and its reproducibility differs in each dilatometer, this cannot yield a precision for a single device. However, it allows the comparison of calibration quality and comparability of data acquired with similar devices.

The data obtained within this work exhibits similar accuracy compared with the data obtained with the other cell. However, the curve of the thermal expansion coefficient acquired with the other dilatometer is smoother allowing a better determination of e.g. phase transitions (see section 7).

[5]Data provided by Müller [86].

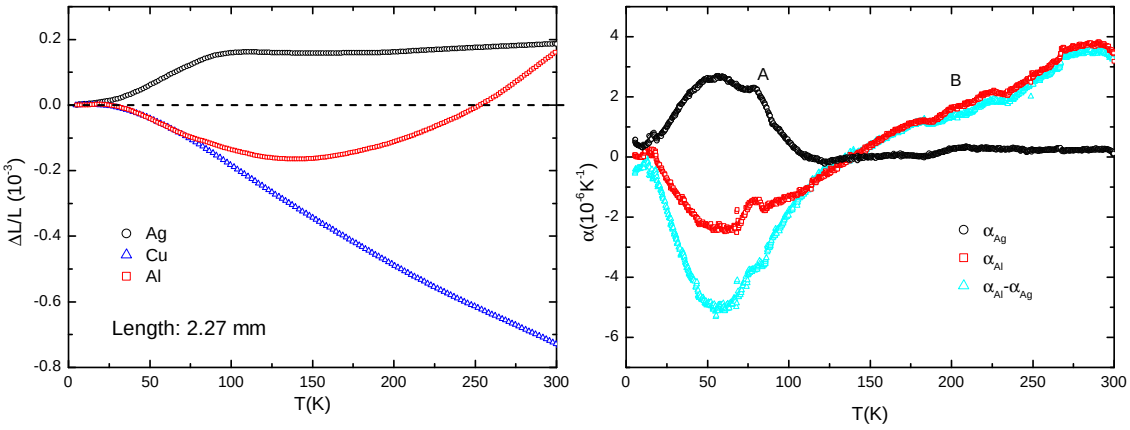

Figure 5.9: Left: Cell effect and measured relative length changes of aluminum and copper without subtracting the background. Right: First two terms of eq. 5.5 for aluminum and their difference.

5.4 Aluminum

Thermal Expansion

In addition to copper, a test measurement of a high-purity aluminum sample (99.996 %) with $l = 2.27\,\mathrm{mm}$ was performed.

Figure 5.10 shows the relative length change versus literature data. The error relative to literature data is overall larger than in copper. The increasing error starting at 150 K can be explained by the decreasing difference of measured relative length change and the cell effect (see fig. 5.9). This effect arises from the larger expansion of aluminum compared with silver at high temperatures(see fig. 9.1).

The thermal expansion coefficient shows a deviation similar to copper (see fig. 5.11) at high temperatures. In comparison with fig. 5.5, this is again attributed to the poor reproducibility of the cell effect. However, feature A observed when measuring copper (see fig. 5.7) appears less pronounced. Investigating the different terms of eq. 5.5 show that the feature appears in the cell effect and in the actual measurement and thus cancels out (see fig. 5.9).

Since the measurement of the thermal expansion of copper is performed using a different cryostat and sample rod than for the cell effect, whereas the aluminum data was obtained using the same cryostat and sample rod as for the cell effect, feature A is attributed to the experimental setup and not the cell. The setup might also give rise to the poor reproducibility of the cell effect (feature B). However, in order to have further evidence, measurements of the cell effect have to be conducted in another setup.

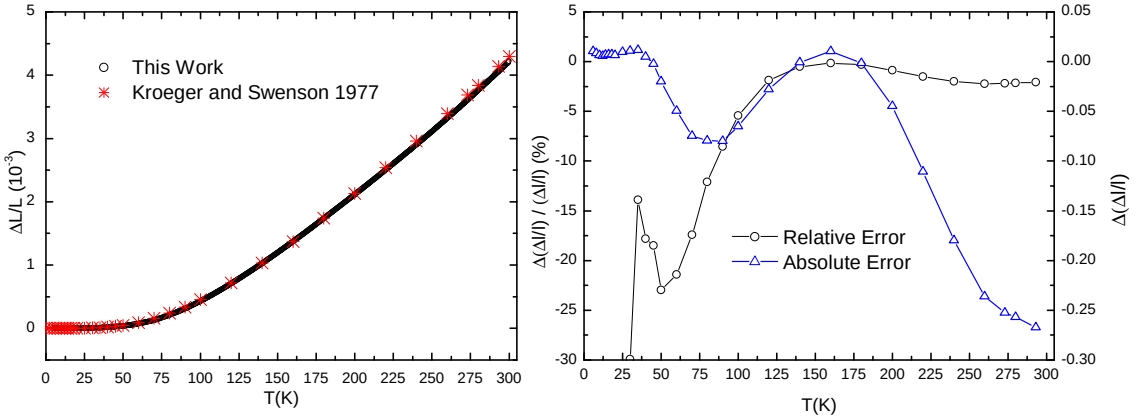

Figure 5.10: Left: Relative length change of aluminum. Right: Absolute and relative error of the relative length change compared with literature data [37].

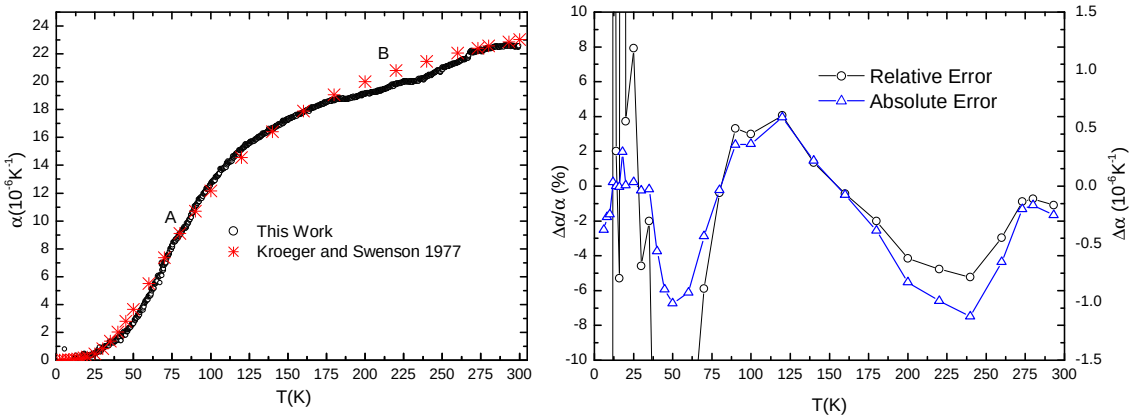

Figure 5.11: Left: Linear thermal expansion coefficient of aluminum. Right: Absolute and relative error of the linear thermal expansion coefficient compared with literature data [37]. Feature A marks a region, where an unsmooth deviation is visible in copper, but not in aluminum. Feature B denotes a deviation also seen in copper (see section 5.3).

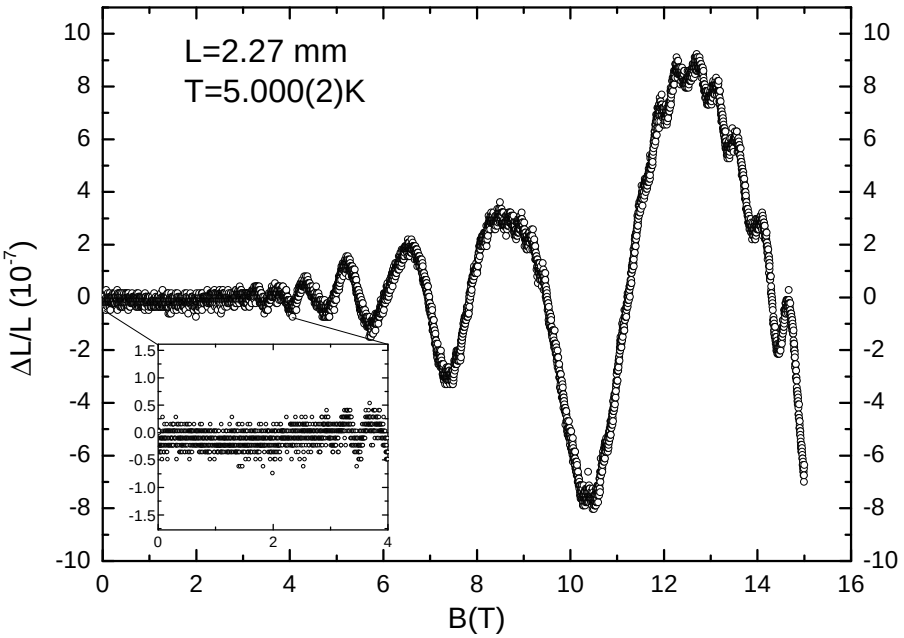

Figure 5.12: Magnetostriction of aluminum at $T = 5.000(2)\,\mathrm{K}$. The data features magnetooscilations known from literature [17].

Magnetostriction

The phenomenon of magnetooscillations in metals is an elegant tool to investigate the length change resolution of the dilatometer. As already mentioned in 2.4, this effect arises from the de-Haas-van-Alphen effect, the oscillation of the magnetization with changing external magnetic field. The measurement shows two oscillations with different frequency and amplitude lying on top of each other, which correspond to different extremal cross-sections of the Fermi surface [6]. The first oscillation is visible, when the amplitude reaches $\approx 5 \times 10^{-8}$, which acts as a scale for the resolution of the dilatometer.

[6] A detailed analysis of aluminum was conducted by Griessen [17].

6 $LiMn_{0.95}Ni_{0.05}PO_4$

6.1 Crystal Properties

$LiMn_{0.95}Ni_{0.05}PO_4$ belongs to the family of the olivine phosphates $LiMPO_4$(M=Mn,Fe,Co,Ni), which came into the focus of research due to their exceptional high lithium-ion conductivity [96] and large magnetoelectric effect[1][97]. The first makes them in principle well-suited for electrochemical energy storage devices as secondary batteries [96]. However, the application is hindered by their poor electronic conductivity. Efforts to improve its value have hitherto only been successful for M=Fe [98]. Currently, research is being focused on doing the same with the other compounds, since the cell voltage increases by replacing Fe with Mn, Co or Ni (in this order). Considerable progress has been made for the M=Mn materials [99]. A Ni-doping is supposed to increase the cell voltage further, making it worthwhile to investigate such materials. The second peculiarity, the large magnetoelectrical effect, offers additionally a wide range of applications [100]. Magnetic fields, to name but one, could be detected with high sensitivity.

In this chapter, the thermal expansion of a $LiMn_{0.95}Ni_{0.05}PO_4$ single crystal is investigated in order to analyze the interplay of magnetic ordering and the crystal lattice. The synthesis and growth of the crystal is described elsewhere [101].

Figure 6.1 shows the crystal structure of $LiFePO_4$, which shares the same olivine-structure with $LiMn_{0.95}Ni_{0.05}PO_4$ [101]. Layers of magnetic M-ions stacked along the a-axis are separated by lithium layers and PO_4 tetraeda. The magnetic ions are surrounded by oxygen atoms forming octahedra. $LiMn_{0.95}Ni_{0.05}PO_4$ belongs to the Pnma symmetry group and the lattice constants for $LiMn_{0.95}Ni_{0.05}PO_4$ are a=10.432(2) Å, b=6.087(3) Å and c=4.735(3) Å [101].

An AFM(antiferromagnetic) ordering is observed in every compound of the isostructural group $LiMPO_4$ at low temperatures. However, it has been found that the easy axis of the magnetization differs depending on the magnetic ion M: $LiMnPO_4$, $LiFePO_4$, $LiCoPO_4$ and $LiNiPO_4$ order antiferromagnetically with easy axis along the crystallographic a, b, b and c axis [102]. Wang et al. [101] observes an AFM ordering along the a axis within

[1]Magnetoelectricity is the effect of an electrical polarization occurring under the influence of an external magnetic field.

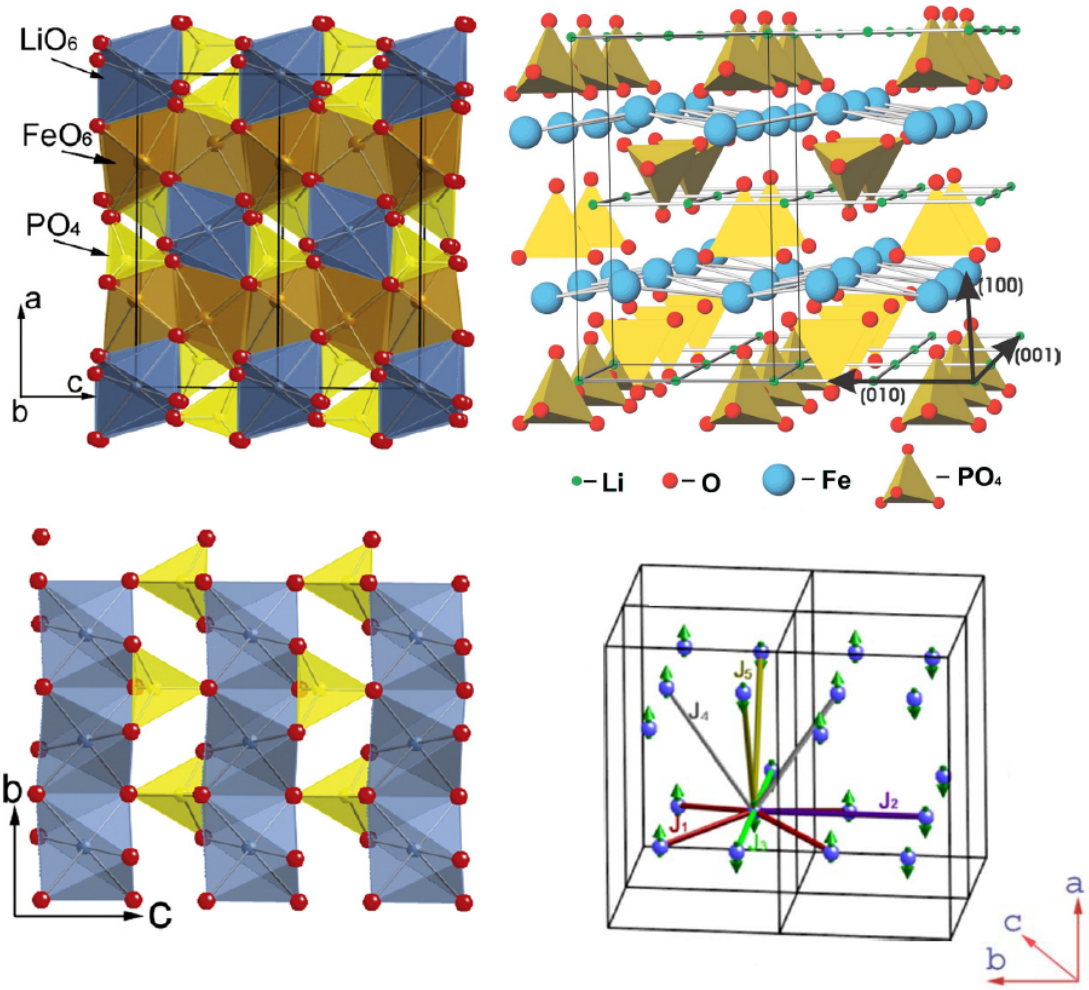

Figure 6.1: Structure of $LiFePO_4$ as an example for the $LiMPO_4$ family. Left top and bottom: From Li et al. [108] Right top: From Lit et al. [103]. The directions (100),(010) and (001) correspond to the a,b and c axis. Right bottom: Drawing is showing the antiferromagnetic ordering along the a-axis of$LiMn_{0.95}Ni_{0.05}PO_4$ with antiferromagnetic coupling in-plane and ferromagnetic coupling between planes. From [102].

$LiMn_{0.95}Ni_{0.05}PO_4$ matching the expectation that the magnetic properties are not greatly influenced by a 5 % Ni-doping (see fig. 6.2).

Neutron scattering studies found that the spins in $LiFePO_4$ [103], $LiCoPO_4$ [104] and $LiNiPO_4$ [105] are not strictly collinear, but rotated by a small angle with respect the to the easy axis. This spin ordering in buckled planes within $LiCoPO_4$ allows the formation of so called ferrotoroidal magnetic domains, which may give rise to the strong magnetoelectric effects [106, 107].

From susceptibility measurements the Néel temperature is determined to be 32.5 K (see fig. 6.2).

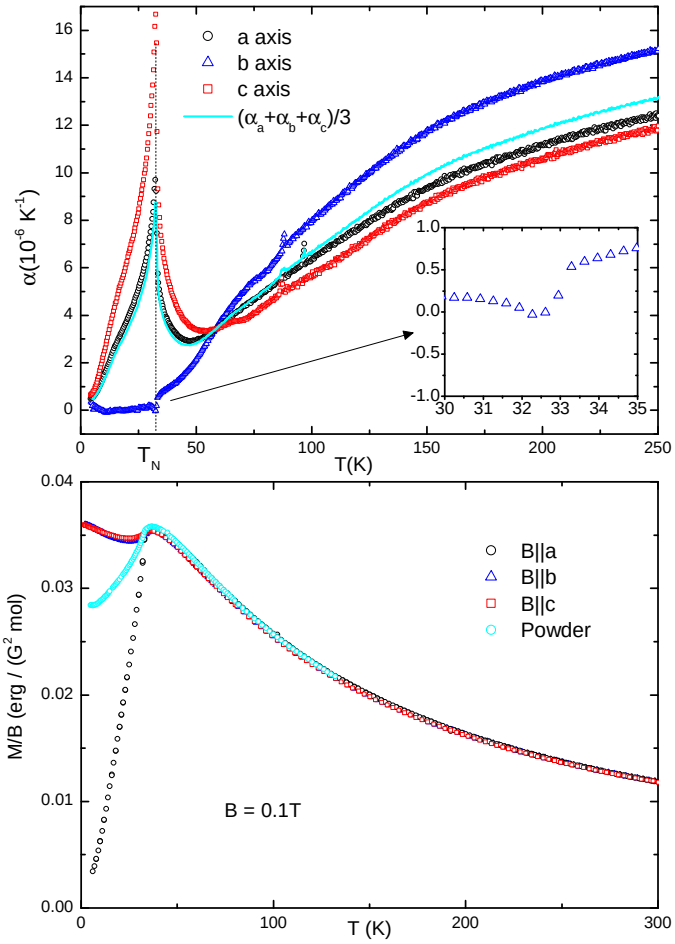

Figure 6.2: Top: Linear thermal expansion coefficient of $LiMn_{0.95}Ni_{0.05}PO_4$ of the a,b and c axis and volume. The black line shows an estimate of the the phononic contribution. Bottom: Magnetic susceptibility measured with an external magnetic field of 0.1 T. Mag. susceptibility from [101].

6.2 Thermal Expansion

The measurements of $LiMn_{0.95}Ni_{0.05}PO_4$were conducted at the Technical University of Vienna using a setup different from the one described in section 3. The cell was replaced by a cell of similar design having a smaller cell effect (see fig. 6.5). Temperature control is achieved via a similar setup described in 3. However, the cryostat used in this setup is a bath cryostat, i.e. there is no direct control of the cooling power via a needle valve. The cell is coupled to a helium reservoir via helium exchange gas. Through the control of the helim exchange gas pressure the thermal coupling and thus the cooling power can be adjusted. Heating is achieved by a resistance heater attached to the shielding tube (see 3.7). The a- and c- axis show each a pronounced positive anomaly at the Néel temperature $T_N = 32.5(5)$ K confirming the ordering temperatures observed in the magnetization (see fig. 6.2). On the contrary, only a slight change is observed along the b-axis. However, the expansion along the b-axis is the largest at high temperatures. The c-axis shows the

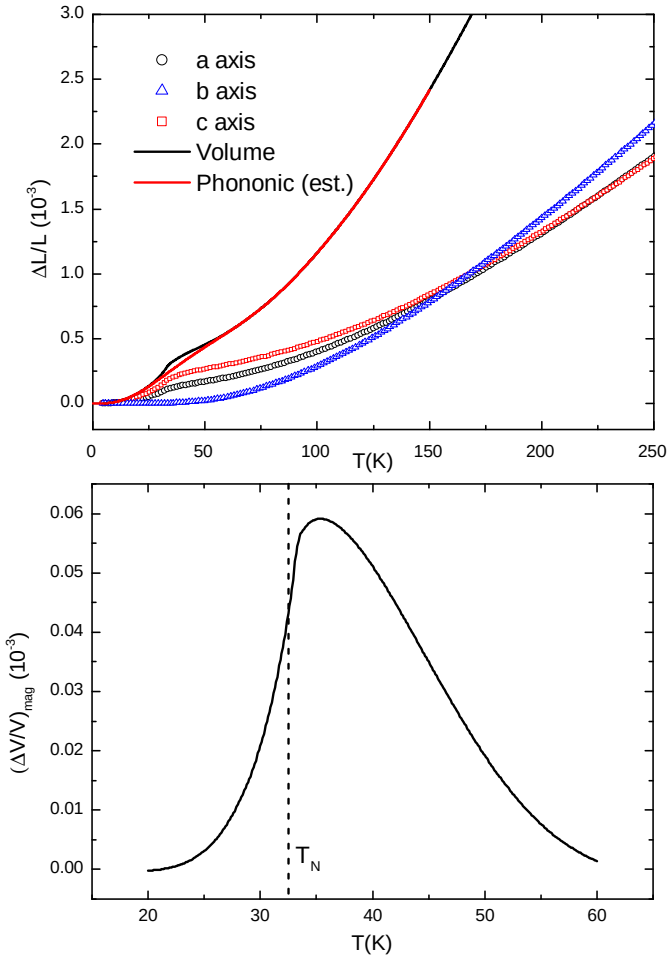

Figure 6.3: Top: Relative length change of $LiMn_{0.95}Ni_{0.05}PO_4$ along different axes, relative volume change and approximate phononic driven volume expansion. Bottom: Magnetically driven relative volume change.

largest anomaly although the magnetic coupling is supposedly weaker than in the a-axis. However, magnetoelastic effects are the result of an interplay between magnetic anisotropy, magnetic exchange interaction[2] and elastic properties of the crystal. All of these parameters are currently unknown for the investigated compound. A comparison with the data of Co_2SiO_4, a material exhibiting the same olivine structure indicates that the directions of the anomalies are not an intrinsic property of the crystal symmetry [110]. By interpolating the relative length changes of each axis, the overall volume change is calculated:

$$\frac{\Delta V}{V_{\mathrm{RT}}} = \left(1 + \frac{\Delta l_a}{l_a}\right)\left(1 + \frac{\Delta l_b}{l_b}\right)\left(1 + \frac{\Delta l_c}{l_c}\right) - 1, \tag{6.1}$$

where V_{RT} denotes the volume of the crystal at room temperature.

A rough estimate of the phonon background is assessed by fitting a polynomial to high-

[2]Magnetic anisotropy and exchange coupling have found to be equally important in $LiCoPO_4$[109].

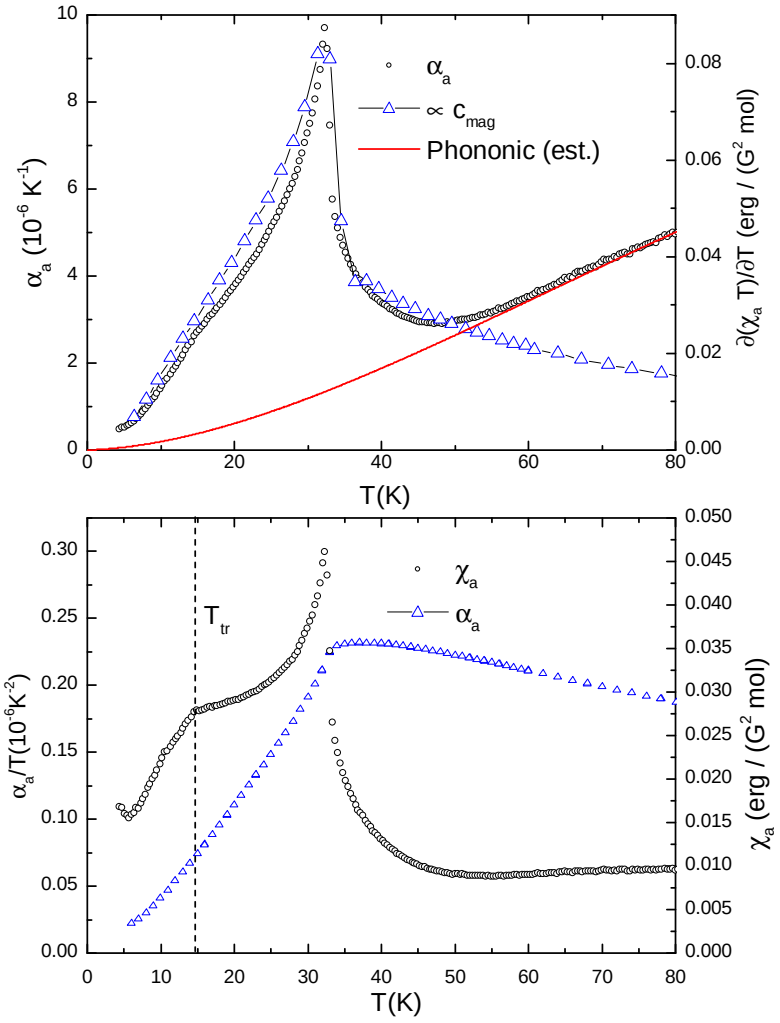

Figure 6.4: Top: Magnetic contribution to the thermal expansion along the a-axis and the quantity $\partial(\chi T)/\partial T$, which is proportional to the magnetic specific heat. Middle: α_a/T showing a transition at T_{tr} and magnetic susceptibility along a-axis

temperature values of $\Delta V/V_{\mathrm{RT}}$ (see fig. 6.3). In order to yield the magnetovolume effect (relative length change caused by spontaneous magnetostriction), the estimated phonon background is subtracted. The maximum of the resulting curve is 6×10^{-5} corresponding to an expansion of $7 \times 10^{-4}\,\mathrm{mm}^3$.

Using the susceptibility data, one can calculate the magnetic specific heat

$$\frac{\partial\,(\chi T)}{\partial T} \propto c_{\mathrm{mag}}, \tag{6.2}$$

which is proportional to the magnetic specific heat c_{mag} [111]. The magnetic specific heat mimics the thermal expansion along the a-axis α_a closely (see fig. 6.4). The Grüneisen relation (eq. 2.21) indicates that the energy scale responsible for the magnetic ordering dominates within this temperature range.

Plotting α_a/T, a kink at $T_{\mathrm{tr}} = 14.7(5)\,\mathrm{K}$ becomes visible. It is known from the cali-

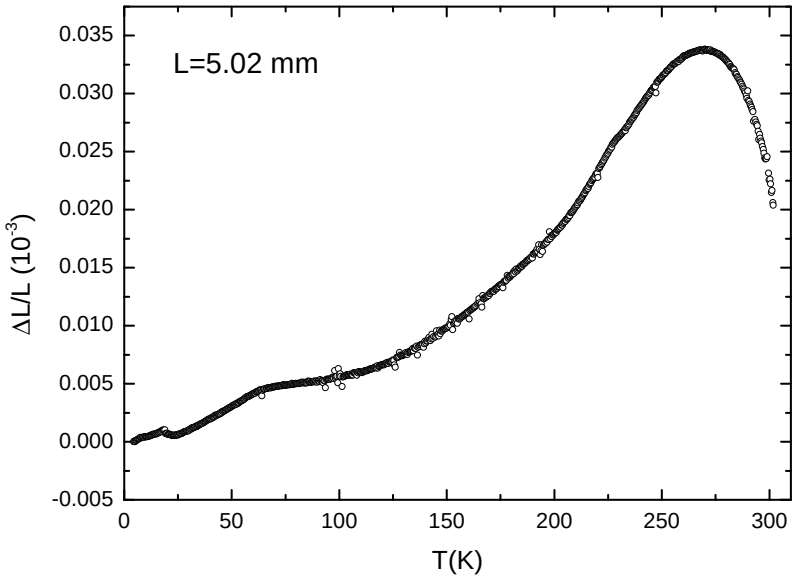

Figure 6.5: Cell effect for the cell used for the measurements of $Li(Mn_{0.95}, Ni_{0.05})PO_4$. Data provided by Müller [86].

bration measurements (see chapter 5), that the error increases at low temperatures and deducing sample effects below 20 K can be hazardous. However, due to the anomaly, $LiMn_{0.95}Ni_{0.05}PO_4$ exhibits a relative large expansion at low temperatures. Compared with the results presented in section 5.2 the cell effect is one order of magnitude less mitigating effects seen in the measurand. Based on these considerations and from the observation that the surrounding points exhibit a smooth behavior, this feature is treated as a sample effect. Its shape does not resemble a discontinuity caused by first- or second-order phase transitions. The origin of the feature can hence not be elucidated at this point. Szewcyk et al. observe a similar feature in $LiCoPO_4$ when the sample is exposed to a magnetic field of 8 T [112]. The authors present evidence suggesting that the transition is caused by a change in the rigidness of the spin lattice, i.e. the magnon system, either by a change in the exchange interaction or magnetic anisotropy. In $LiMn_{0.95}Ni_{0.05}PO_4$ the magnetic susceptibility shows no anomaly at T_{tr} providing further evidence that the effect does not arise from a magnetic order phenomenon.

In order to draw further conclusions on the transition at T_{tr} and to establish a stronger link to the observation of Szewcyk et al., more information is needed. It is suggested to measure the thermal expansion with an external magnetic field, since data of Szewcyk et al. shows that the anomaly increases with magnetic field strength. An observation of the feature in specific heat measurements and testing its magnetic field dependency would further provide confirmation that the feature corresponds to the findings of Szewcyk et al. The phononic background of α_a is estimated via a polynomial and subtracted. The resulting $\alpha_{\mathrm{a,mag}}$ shows the expansion caused by magnetoelastic coupling. The Onsager

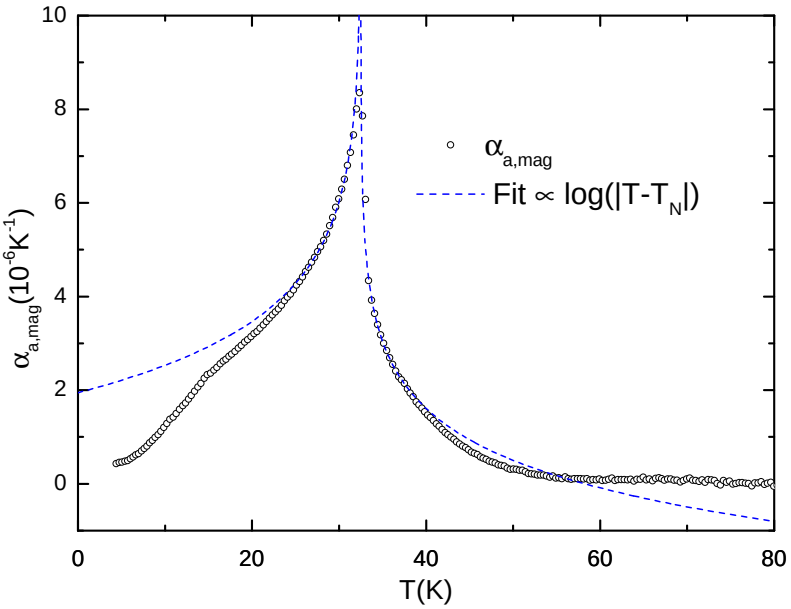

Figure 6.6: Magnetically driven thermal expansion $\alpha_{\mathrm{a,mag}}$ with fits corresponding to the Onsager solution for a 2D-Ising-system (see text for details)

solution to the 2D-Ising model yields [113, 114]

$$c_m \propto \log(T - T_N) \Rightarrow \alpha_{\mathrm{a,mag}} \propto \log(T - T_N). \tag{6.3}$$

Fitting $a \log(T - T_N) + c$ to $\alpha_{\mathrm{a,mag}}$ yields a good agreement close to the phase transition (see fig. 6.6). Szewcyk et al. perform the same analysis for $LiCoPO_4$ and obtain similar results. They treat the agreement as an indication of a quasi-2D-Ising behavior of the Co-spins and presume that the asymmetric shape of the transition arises from the weak coupling of the magnetic moments between Co-layers.

7 $CeFeAsO_{1-x}F_x$

7.1 Background on Iron-Pnictides

Soon after the discovery of the new class of iron-based superconductors by Kamihara et al [115] in 2008, the dawn of a new "iron age" succeeding the "copper age" of cuprates was proclaimed [116]. Despite an extensive effort to increase the critical temperature, the record-holder among iron-based superconductors remains GdThFeAsO with $T_C = 56\,\mathrm{K}$ [117, 118]. This is still below the boiling point of nitrogen, the crucial barrier for applicability, which has only been surpassed by cuprates yet. However, in contrast to several iron-based superconductors, their brittleness makes them unfavorable for machining. Nevertheless, using the full-fledged arsenal of solid-state physics, a comprehensive knowledge of characteristic properties was accumulated leading the way to a deeper understanding of the underlying processes of superconductivity in iron-based superconductors.

Figure 7.1 shows the most investigated crystal structures of Fe-based superconductors. All members include a layer of FePn, where Pn is a pnictogen (mostly As), hence the name iron-pnictides (from ancient Greek πνίγειν , "to choke") or iron-arsenides. The 11-systems (see below) constitute an exception having FeSe or FeTe planes giving them the name iron-chalcogenides[1]. This is similar to cuprates, where CuO_2 planes are a common feature. However, in cuprates, the CuO_2 planes are square planar, whereas the structure of the iron-pnictogen bonds is tetrahedral. Iron-based superconductors compounds are classified as follows:

1111 FePn-layers with RO-layers(R=rare-earth ion) in between
122 FePn-layers with R-layer in between
111 FePn-layers with A-layers(A=Alkali metal) in between
11 FeSe-layers or FeTe-layers directly stacked upon each other

A description of more complicated iron-pnictides (e.g. 32522) which have also been found to exhibit superconductivity can be found elsewhere(e.g. [120]).

Untreated 1111 and 122 systems show either a tetragonal-orthorhombic structural transition at T_S together with an antiferromagnetic ordering at $T_N \leq T_S$ or a superconducting

[1] In contrast to As and Te, Se is non-toxic.

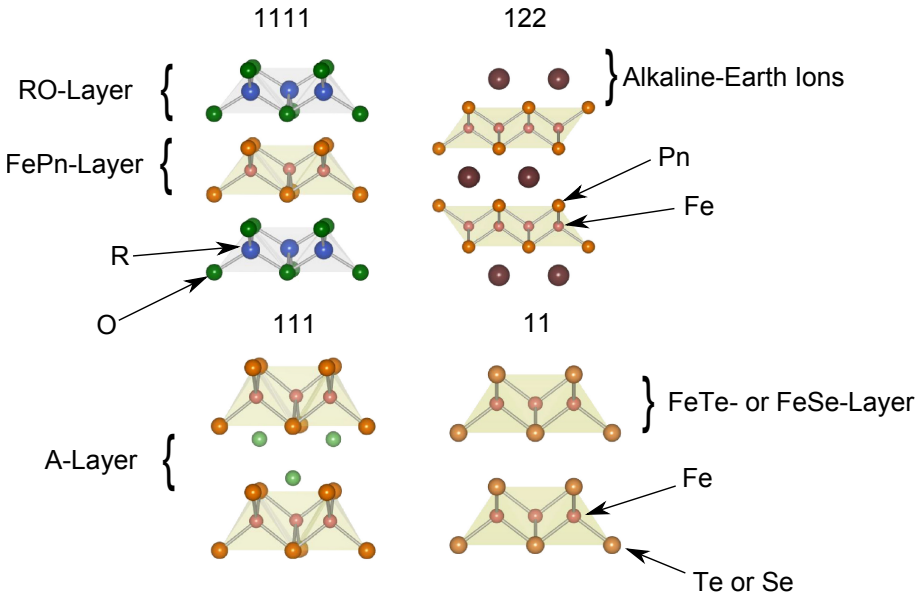

Figure 7.1: Drawing showing the structural classification of iron-based superconductors. Pn: Pnictogen, A: Alkali metal and R: Rare-earth ion. After [119].

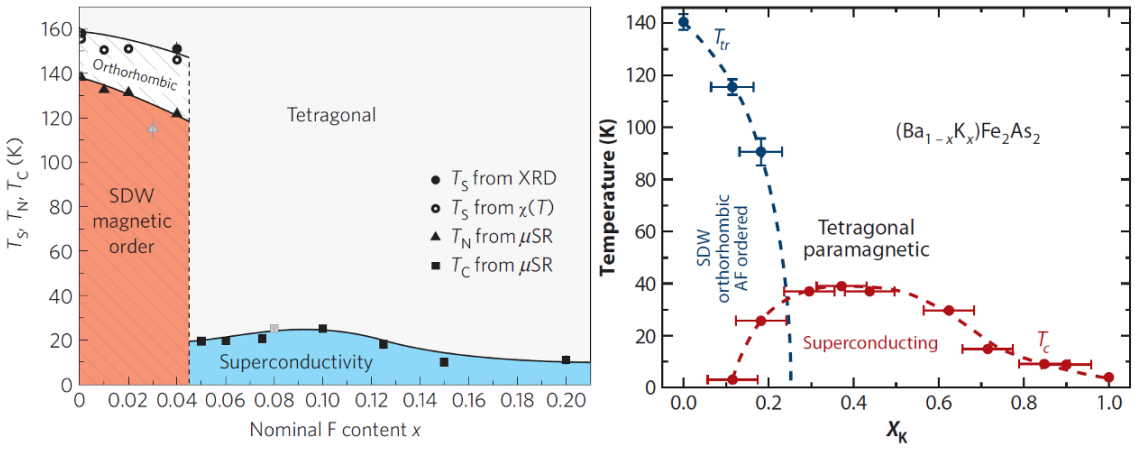

Figure 7.2: Phase diagrams of LaFeAsO [121] and $Ba_{1-x}K_xFe_2As_2$ [120].

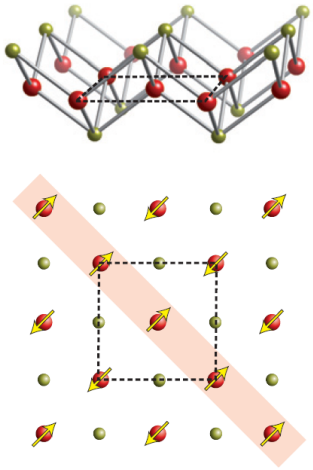

Figure 7.3: Drawing showing a typical stripe ordering in the FePn-layers FeSe-layers in the antiferromagntic phase of iron-based superconductors. From [122]. The stripe order for FeTe is different [125] Top: Side view of iron layer (red:iron ions, gold: pnictogen/chalcogen anions). Botto,: Stripe order of Fe-Spins within iron-layers.

phase at T_C when cooled down under atmospheric pressure. The structural and magnetic transition can be coinciding (e.g. $BaFe_2As_2$) or occurring at separate temperatures(e.g. LaFeAsO). The magnetic ordering has found to be a commensurate SDW (spin density wave) forming stripes within the FeAs-planes ([122] and references therein, see fig. 7.3).

The common appearance of structural and magnetic transitions is striking. The concept of a nematic phase was proposed to explain the interplay of magnetic and structural degrees of freedom [123, 124]. In this picture, the structural transition would be naturally explainable by the magnetoelastic coupling of spin correlations and thus the structural transition would be a precursor for an impeding magnetic ordering.

If additional holes or electrons are introduced into the FeAs-layers by doping, two cases can happen. If one starts with a non-superconducting compound, the magnetic and structural transitions are suppressed and a superconducting phase emerges. For superconducting parent compounds, the contrary is observed. Doping enhances T_C up to a maximum, but then suppresses the superconducting phase, whereas an antiferromagnetic phase and new orthorhombic phase emerges (see fig. 7.2). Similar effects can be induced by applying pressure [126] or even by an isovalent doping(e.g. replacing As by P [127]).

A mixing of superconducting and SDW-phase is also observed [128]. However, it is still debated whether the phases occur separately [129] or microscopically mixed [130].

In the non-superconducting phase, Fe-superconductors have metallic properties. This is in contrast with cuprates, which are insulators at room temperature, but a feature in common with heavy-fermion superconductors [131] and BSC-type superconductors.

The largest quest for understanding the physics of Fe-SC is, of course, the clarification of the pairing mechanism and the symmetry of the order parameter. However, current

results favor a conventional s-wave or s±-wave (see [122] and references therein). A pairing mechanism based fully on conventional electron-phonon coupling is not favored by theoretical considerations [132] and experimental data of the isotope effect yields only an exponent of 0.35 in $SmFeAsO_{1-x}F_x$ (0.5 is predicted by BCS-theory) [133][2] However, its closeness to 0.5 might indicate that phonons are not irrelevant. A promising candidate for the Cooper pair coupling mechanism are antiferromagnetic spin fluctuations [134].

7.2 Thermal Expansion

In this section, the results of thermal expansion measurements of the 1111 compound $CeFeAsO_{1-x}F_x$ with x=0, x=0.02 and x=0.04 is analyzed. The electron-doping via fluor is expected to suppress the structural and AFM transition, since this is a generic property of 1111-systems. The doping levels are nominal, i.e. have been obtained via weighing the precursors before the crystal synthesis.

7.2.1 Parent Compound, CeFeAsO

Figure 7.4 shows the results obtained for undoped CeFeAsO. The expansion of the cell is larger at temperatures below $\approx 100\,\mathrm{K}$, thus a non-smooth behavior in this region is treated as an influence of the cell effect. The expansion is much less than copper, making the interpretation of features overall more hazardous. However, the phase transitions can be clearly identified by anomalies in α. The structural transition can be observed at $T_\mathrm{S} = 151.4{+}1{-}0.5\,\mathrm{K}$ and the subsequent negative anomaly with the magnetic transition at $T_\mathrm{N} = 137.0(5)\,\mathrm{K}$. The errors are estimated based on the distance to surrounding data points and the error of the thermometer(see section 3.8). Both of the transition temperatures agree well with literature [135]. The rising α at $\approx 5\,\mathrm{K}$ can be related to the magnetic ordering of cerium moments, since its order temperature $T_\mathrm{Ce} = 4.4(3)\,\mathrm{K}$ [135] is known.

Assuming a second-order magnetic phase transition, the pressure dependence of T_N can be estimated via eq. 2.34. From fig. 7.4, $\Delta\beta = 3\Delta\alpha \approx 3 \times 10^{-6}\,\mathrm{K}^{-1}$ is estimated. With $V_m = 4.17 \times 10^{-5}\,\mathrm{m}^3\,\mathrm{mol}^{-1}$ [136] and $\Delta c_p \approx 2.5\,\mathrm{J\,K}^{-1}\,\mathrm{mol}^{-1}$ [137], one finds

$$\frac{dT_N}{dp} = V_m T_N \frac{\Delta\beta}{\Delta c_p} \approx -8\,\frac{\mathrm{K}}{\mathrm{GPa}}. \tag{7.1}$$

Zocco et al. finds that $dT_N/dp = -9\,\mathrm{K\,GPa}^{-1}$ by directly applying hydrostatic pressure, which agrees with the value obtained here considering the large uncertainties involved in determining Δc_p and $\Delta\beta$ [138].

[2] An electron-phonon coupling in the BCS sense, would yield $T_C \propto M^{-0.5}$, where M is the mass of an atom of the superconductor.

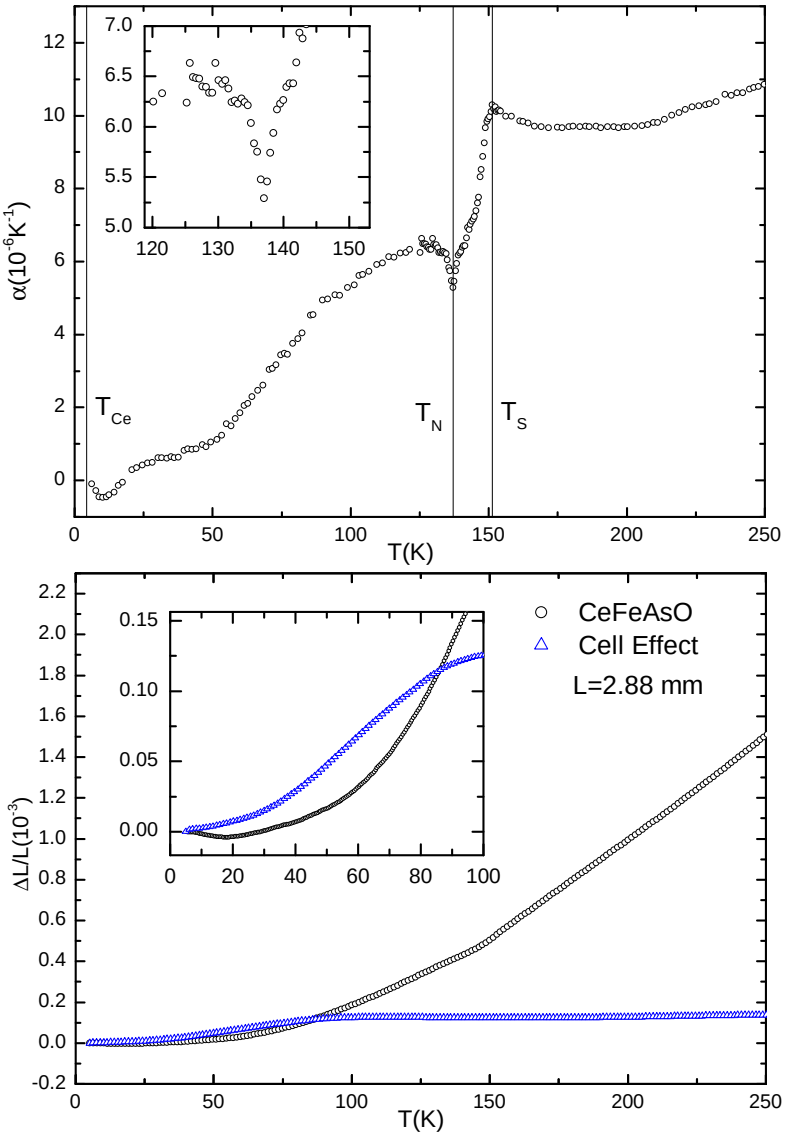

Figure 7.4: Top: Thermal Expansion Coefficient of undoped CeFeAsO. Inset shows the magnetic transition. T_S, T_N, T_{Ce} denote the temperature of the structural transition, magnetic transition and the cerium moment ordering. Bottom: Relative length changes of CeFeAsO and cell effect. The cell effect is greater than the samples expansion at low temperatures, which indicates a large error in this temperature region.

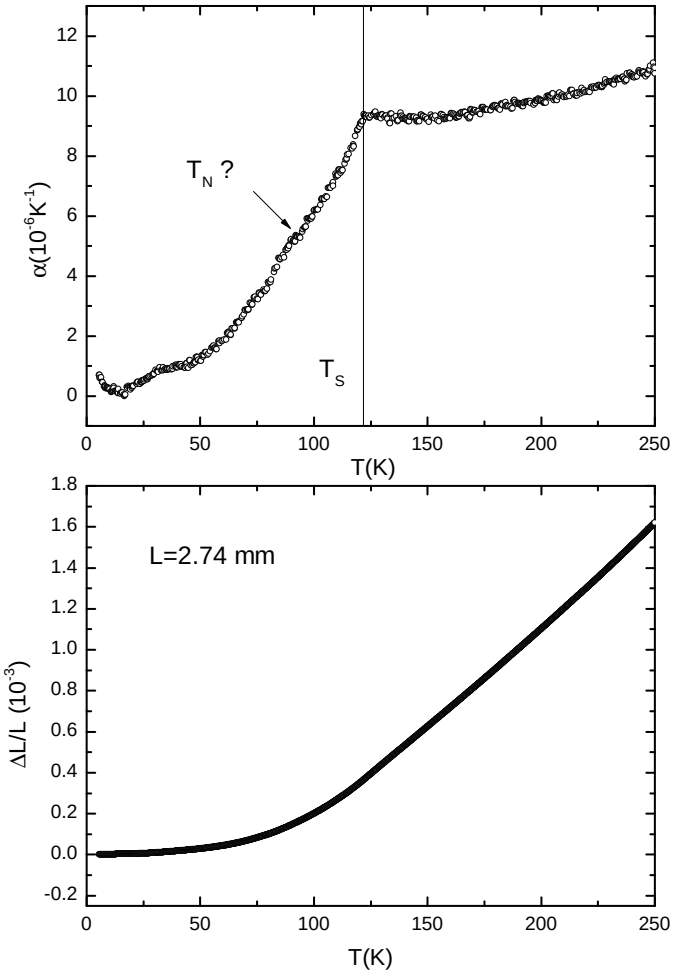

Figure 7.5: Top: Thermal expansion coefficient of $CeFeAsO_{0.98}F_{0.02}$. T_S denotes the structural transition temperature. The magnetic transition could not be differentiated from noise. T_N marks the approximate position which is expected from the phase diagram in [135]. Bottom: Relative length changes.

7.2.2 $CeFeAsO_{0.98}F_{0.02}$

In the 2 % fluorine-doped material, the thermal expansion coefficient shows a much less pronounced transition at $T_S = 121.7(5)$ K. The noise prohibits a clear identification of the magnetic ordering temperature. However, it is suspected to be around 90 K based on the phase diagram in [135]. The onset of the Ce-ordering can again be observed, but the incomplete peak does not allow a clear determination of T_{Ce}. From literature [135] a slight lowering of T_{Ce} relative to the undoped material is expected.

The observed decrease of the anomaly heights and the smearing out of phase transition is similar to $LaO_{1-x}F_xFeAs$ [54].

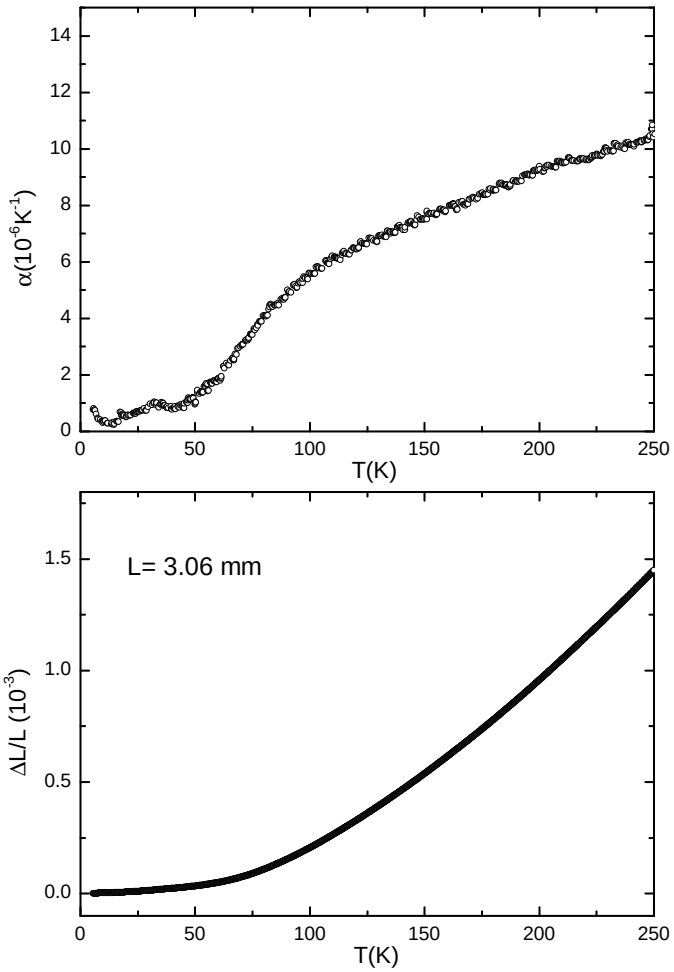

Figure 7.6: Top: Thermal Expansion Coefficient of $CeFeAsO_{0.98}F_{0.04}$. Bottom: Relative length changes.

7.2.3 $CeFeAsO_{0.96}F_{0.04}$

Figure 7.6 shows the thermal expansion and relative length change of a $CeFeAsO_{0.98}F_{0.04}$ sample with length $l = 3.06\,\mathrm{mm}$. No phase transition temperatures can be extracted from the data. It is assumed that noise and cell effect superimpose the signal caused by the sample. In comparison with literature [135], the small anomaly at low temperatures can again be related as the cerium ordering.

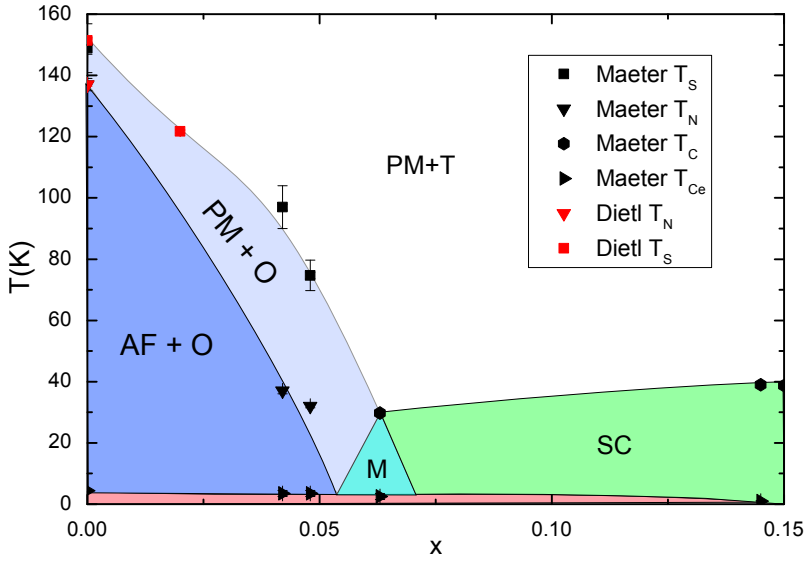

Figure 7.7: Phase Diagram of $CeFeAsO_{1-x}F_x$. Results of this work are combined with data from [135]. AF+O: Antiferromagnetic+Orthorhombic, PM+O: Paramagnetic+Orthorhombic, SC: Superconducting, M: Mixed Phase. All lines are guides to the eye.

Nominal(%)	NQR(%)
5	4.2(2)
10	4.8(3)
15	6.3(2)
20	14.5(20)
25	15.0(20)

Table 7.1: Doping levels obtained via weighing precursors (nominal) and via NQR after synthesis [139].

7.3 Phase Diagram

The results from the measurements are combined with data from Maeter et al. [135] within a phase diagram (see fig. 7.7). The data for the undoped compound agrees with the data from Maeter. The doping level for T_S at x=0.02, however, has to be afflicted with additional error, since its doping level is nominal, i.e. measured by weighing the different elements before synthesis. Maeter et al. used Nuclear Quadropole Resonance to determine more accurate x and showed that the deviation between the real and nominal doping levels can yield up to 50 % [139]. However, only small deviations between nominal and actual doping levels are shown for low F-concentrations (see tab. 7.1).

8 Conclusion and Outlook

The thesis at hand describes the setup and calibration of an experiment to measure thermal expansion from 5 K to 300 K by means of high-resolution capacitive dilatometry and demonstrates its applicability via measuring reference materials and studies of CeFeAsFO. Thermal Expansion data of $LiMn_{0.95}Ni_{0.05}PO_4$ was measured with a different setup at the Vienna University of Technology and analyzed.

Temperature control was achieved using a helium gas-flow cryostat from Oxford instruments. In order to enhance the temperature stability, a second resistance heater close to the dilatometer was used. The cryostat is equipped with a superconducting magnet being able to deliver magnetic fields up to 17 T. The capacitance is measured via a three-terminal method using the ultra-precision capacitance bridge 2550A from Andeen Hagerling.

Through measurements of copper and aluminum reference samples it is shown that the experiment is able to measure relative length changes and thermal expansion coefficients with an accuracy of the order 1×10^{-5} and $1 \times 10^{-7}\,\mathrm{K}^{-1}$, respectively. The cell effect arising from the expansion of the dilatometer itself was determined to be of the order 1×10^{-4} in relative length change $\Delta l/l$. Its non-reproducibility was analyzed and various possible sources were discussed. The search for the origin of the non-reproducibility turned out to be challenging and is still ongoing. However, it was found in copper and aluminum measurements that the cell effect causes only minor errors in the thermal expansion coefficient α. Nevertheless, unwanted features (e.g. dips) can be observed, which may not be distinguishable from sample effects when measuring materials with unknown thermal expansion.

The temperature stability of 1 mK at 5 K makes the setup well-suited for magnetostriction measurements. This was confirmed by data obtained from silver and aluminum samples. The magnetooscillation observed in aluminum demonstrates a resolution of 5×10^{-8} in $\Delta l/l$. The cell background caused by magnetic forces was determined to be of the order 1×10^{-7} in $\Delta l/l$.

Measurements of $\Delta l/l$ and α of single-crystalline $LiMn_{0.95}Ni_{0.05}PO_4$ were conducted. The experiments were performed using a similar dilatometer at the Vienna University of Technology with a cell effect of one order of magnitude less, which mitigates systematic errors. The antiferromagnetic phase transition was analyzed and two strong positive anomalies

in the a and c axis[1] at the Néel-temperature of $T_N = 32.5\,\mathrm{K}$ were found, whereas the b axis showed no clear changes at the transition. A logarithmic divergence was fitted to the phase transition. Following the analysis of Szewczyk et al. this indicates a quasi-2D-Ising behavior of the Mn/Ni spins [112]. An additional feature of unknown origin was found at $T_{\mathrm{tr}} = 14.7\,\mathrm{K}$ similar to the one found by Szewczyk et al in $LiCoPO_4$ analyzing specific heat data under an magnetic field of 8 T. Here, a change in stiffness of the magnon system is proposed to cause the anomaly in c_p. Further measurements in particular under an external magnetic field are needed in order to elucidate the origin of the new feature.

Furthermore, the thermal expansion of fluorine doped polycrystalline $CeFeAsF_xO_{1-x}$ was measured and analyzed. Despite the small expansivity relative to silver, it was possible to identify phase transitions. For CeFeAsO, the results yield a structural transition temperature $T_{\mathrm{S}} = 151.4{+}1{-}0.5\,\mathrm{K}$ and a magnetic transition at $T_{\mathrm{N}} = 137.0(5)\,\mathrm{K}$ agreeing well with literature [135]. For $CeFeAsO_{0.98}F_{0.02}$, the structural phase transition temperature can be determined to be $T_{\mathrm{S}} = 121.7(5)\,\mathrm{K}$, but no magnetic ordering temperature can be extracted. This value fits well to the established phase diagram of CeFeAsO [135]. The 4 %-doped compound $CeFeAsO_{0.98}F_{0.04}$ shows a thermal expansion coefficient with no clearly observable anomalies, thus no transition temperatures could be inferred.

The quest to obtain a cell effect with better reproducibility still remains. However, this work elucidates important key aspects and can act as a starting point for further investigations. The recently acquired second dilatometer with similar design will allow cross-checks, which can yield important information about how to effectively influence the cell effect. Experiments with different cryostats, temperature control mechanisms and sample rods might also yield more information on how to combat the problem.

Thermal expansion data of $LiMPO_4$ (M=Fe,Mn,Co,Ni) single crystals over the temperature range 5 K to 300 K pose a novelty. Together with specific heat data, dominating energy scales can be determined via the Grüneisen parameter and the pressure dependence of the Néel temperature can be derived through the Ehrenfest relation. Being materials, which are currently heavily investigated due to their intriguing magnetic properties, findings related to magnetoelastic properties could be of scientific interest in particular.

In summary, the goal to set up a capacitive dilatometry experiment with high resolution and good accuracy was successfully achieved, whereas optimization of the cell effect behavior could further enhance data quality.

[1] Axes correspond to the symmetry group Pnma.

9 Appendix

9.1 Reference Thermal Expansion Coefficients

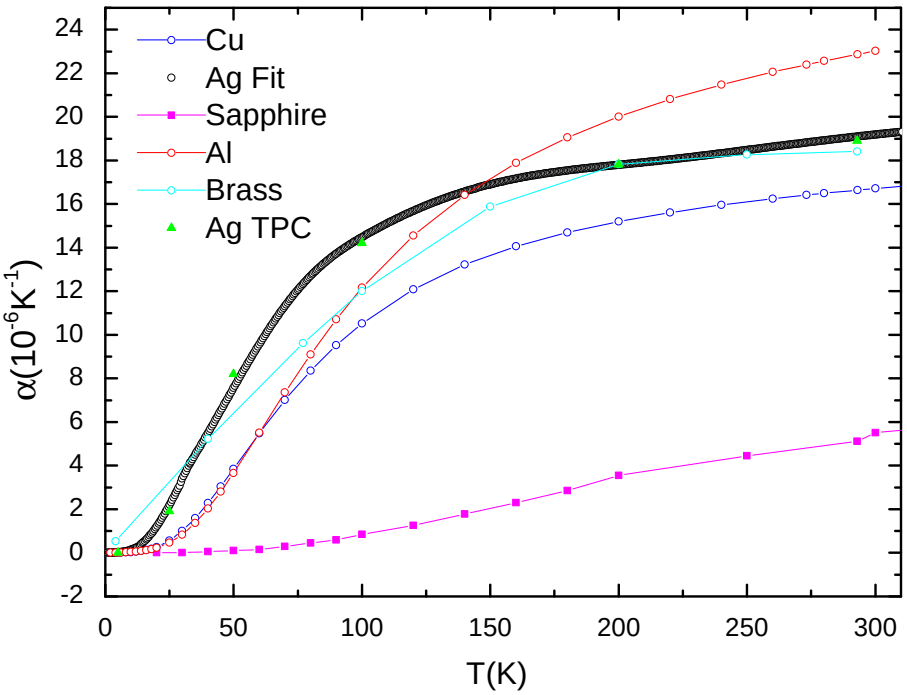

Figure 9.1: Literature values for all relevant thermal expansion coefficients. The fit for Ag used in the analysis is shown. Sources: [52](Ag TPC: recommended values), [37] (Cu and Al), [140] (Sapphire) and [141] (Brass). Thermal Expansion coefficient for brass is derived via fitting and deriving of $\Delta l/l$. Since there are only a few data points given, the values have to be seen as a rough estimate.

References

[1] Grüneisen, E. *Annalen der Physik* **344**(12), 257–306 (1912).

[2] Mie, G. *Annalen der Physik* **316**(8), 657–697 (1903).

[3] Grüneisen, E. *Annalen der Physik* **331**(7), 393–402 (1908).

[4] Prytherch, W. E. *Journal of Scientific Instruments* **9**(4), 128 (1932).

[5] Thompson, A. M. *Instrumentation, IRE Transactions on* **I-7**(3), 245 –253 dec. (1958).

[6] White, G. *Cryogenics* **1**(3), 151 – 158 (1961).

[7] Landau, L. D. and Lifschitz, E. M. *Lehrbuch der theoretischen Physik 5, Statistische Physik Teil 1.* Harri Deutsch, Frankfurt am Main, 8. edition, (1976).

[8] Barron, T. H. K. and White, G. K. *Heat capacity and thermal expansion at low temperatures.* The international cryogenics monograph series. Kluwer Academic/Plenum Publ., New York, (1999).

[9] Lyon, K. G., Salinger, G. L., Swenson, C. A., and White, G. K. *Journal of Applied Physics* **48**(3), 865–868 (1977).

[10] Ashcroft, N. W. and Mermin, N. D. *Solid state physics.* Brooks/Coole Thomson Learning, Singapore, 33. [repr.], (college edition) edition, (2006).

[11] Schwabl, F. *Statistische Mechanik.* Springer, Berlin ; Heidelberg, 3. edition, (2006).

[12] White, G. K. *Proceedings of the Royal Society of London. Series A. Mathematical and Physical Sciences* **286**(1405), 204–217 (1965).

[13] White, G. and Collins, J. *Journal of Low Temperature Physics* **7**, 43–75 (1972).

[14] Zhu, L., Garst, M., Rosch, A., and Si, Q. *Phys. Rev. Lett.* **91**, 066404 Aug (2003).

[15] Carr, R. H., McCammon, R. D., and White, G. K. *Proceedings of the Royal Society of London. Series A. Mathematical and Physical Sciences* **280**(1380), 72–84 (1964).

[16] Green, B. A. and Chandrasekhar, B. S. *Phys. Rev. Lett.* **11**, 331–332 Oct (1963).

[17] Griessen, R. and Olsen, J. *Solid State Communications* **9**(19), 1655 – 1658 (1971).

[18] Kittel, C. *Introduction to solid state physics.* Wiley, Hoboken, NJ, 8. edition, ([20]11).

[19] Gerthsen, C. *Gerthsen Physik.* Springer, Berlin ; Heidelberg, 23 edition, (2006).

[20] Nolting, W. *Statistische Physik.* Springer, Berlin ; Heidelberg, 6. edition, (2007).

[21] Jaeger, G. *Archive for History of Exact Sciences* **53**, 51–81 (1998).

[22] Blundell, S. *Magnetism in condensed matter.* Oxford master series in physics. Oxford Univ. Press, Oxford, 1. publ., repr. edition, (2010).

[23] Sethna, J. P. *Statistical mechanics.* Oxford master series in physics. Oxford Univ. Press, Oxford, repr. edition, (2011).

[24] Atkins, K. R. and Edwards, M. H. *Phys. Rev.* **97**, 1429–1434 Mar (1955).

[25] Nolting, W. *Spezielle Relativitätstheorie, Thermodynamik.* Springer, Berlin ; Heidelberg, 5. edition, (2003).

[26] Meingast, C., Karpinski, J., Jilek, E., and Kaldis, E. *Physica C: Superconductivity* **209**(4), 591 – 596 (1993).

[27] Barron, T., Collins, J., and White, G. *Advances in Physics* **29**(4), 609–730 (1980).

[28] Sokolov, D. A., Ritz, R., Pfleiderer, C., Keller, T., and Huxley, A. D. *Journal of Physics: Conference Series* **273**(1), 012085 (2011).

[29] Kabeya, N., Imura, K., Deguchi, K., and Sato, N. K. *Journal of the Physical Society of Japan* **80**(Supplement A), SA098 (2011).

[30] Kreyssig, A., Green, M. A., Lee, Y., Samolyuk, G. D., Zajdel, P., Lynn, J. W., Bud'ko, S. L., Torikachvili, M. S., Ni, N., Nandi, S., Leão, J. B., Poulton, S. J., Argyriou, D. N., Harmon, B. N., McQueeney, R. J., Canfield, P. C., and Goldman, A. I. *Phys. Rev. B* **78**, 184517 Nov (2008).

[31] Sakai, T., Kagayama, T., and Oomi, G. *Journal of Materials Processing Technology* **85**(1-3), 224 – 228 (1999).

[32] Taylor, R. E. *Thermal Expansion of Solids.* CINDAS Data Series on Material Properties. ASM International, Materials Park, USA, OH, (1998).

[33] Campbell, G. A. *Bell System Technical Journal* **1** July (1922).

[34] Schefzyk, R. *Thermische Ausdehnung von SeCu2Si2-Verbindungen.* Diploma thesis, University of Cologne, (1980).

[35] Andeen-Hagerling. *AH2550A 1KHz Ultra-Precision Capacitance Bridge Operation and Maintenance Manual*, (2002).

[36] Heerens, W. *Sensors and Actuators* **3**, 137–148 (1982/83).

[37] Kroeger, F. R. and Swenson, C. A. *Journal of Applied Physics* **48**(3), 853–864 (1977).

[38] Rotter, M., Müller, H., Gratz, E., Doerr, M., and Loewenhaupt, M. *Review of Scientific Instruments* **69**(7), 2742 (1998).

[39] Pott, R. and Schefzyk, R. *Journal of Physics E: Scientific Instruments* **444** (1983).

[40] Schmiedeshoff, G. M., Lounsbury, A. W., Luna, D. J., Tracy, S. J., Schramm, A. J., Tozer, S. W., Correa, V. F., Hannahs, S. T., Murphy, T. P., Palm, E. C., Lacerda, A. H., Bud'ko, S. L., Canfield, P. C., Smith, J. L., Lashley, J. C., and Cooley, J. C. *Review of Scientific Instruments* **77**(12), 123907 (2006).

[41] Auweiler, T. *Aufbau eines hochauflösenden Dilatometers und Messung der thermischen Ausdehnung von Hochtemperatur-Supraleitern in hohen Magnetfeldern.* PhD thesis, University of Cologne, (1995).

[42] Lang, M. *Thermische Ausdehnung von elektronisch hochkorrelierten Materialien.* PhD thesis, Technische Hochschule Darmstadt, (1990).

[43] Baier, J. *Magnetoelastische Kopplung in multiferroischem $GdMnO_3$ und metamagnetischem $Ca_{(2-x)}Sr_xRuO_4$.* PhD thesis, Köln University, (2006).

[44] Rohrkamp, J. *Aufbau eines kapazitiven Dilatometers zur Messung der thermischen Ausdehnung im Temperaturbereich von 2-300 K.* Diploma thesis, University of Cologne, (2007).

[45] Lortz, R. *Thermische Ausdehnung und Magnetostriktion von La1-xAxMnO3 (A= Sr, Ca).* Diploma thesis, Forschungszentrum Karlsruhe, Technik und Umwelt, (1998).

[46] Collins, G., Col, S. J., and Tainsh, R. J. *Australian Journal of Physics* **40**, 65–71 (1987).

[47] Swenson, C. a. *Review of Scientific Instruments* **68**(2), 1312 (1997).

[48] Brändli, G. and Griessen, R. *Cryogenics* (May), 299–302 (1973).

[49] Genossar, J. and Steinitz, M. *Review of Scientific Instruments* **61**(9), 2469–2471 (1990).

[50] Mehboob, N. *Magnetostriction of measured $GdAg_2$, $PrFe_4As_{12}$, and $GdVO_3$ with a Capacitance Dilatometer.* Diploma thesis, Vienna University of Technology, (2009).

[51] Barcza, A. *Magnetostriction in Rare Earth Elements Measured with Capacitance Dilatometry.* Diploma thesis, (2006).

[52] Touloukian, Y. *Thermal expansion: metallic elements and alloys.* Thermophysical properties of matter. IFI/Plenum, (1975).

[53] Rotter, M. private communication, (2012).

[54] Wang, L. *Thermal Expansion and Magnetostriction Studies on Iron Pnictides.* PhD thesis, Technische Universität Dresden, (2010).

[55] Voort, G. F. V. *SumMet–Ein Leitfaden zur Präparation von Werkstoffen und deren Auswertung.* 3 edition, (2011).

[56] Boyer, L., Houze, F., Tonck, A., Loubet, J. L., and Georges, J. M. *Journal of Physics D: Applied Physics* **27**(7), 1504 (1994).

[57] Hermes Schleifkörper GmbH, Lohrmannstraße 21, 01237 Dresden, Germany. *Hermes Bonded Abrasives (`http://www.hermes-schleifkoerper.de/fileadmin/datapool/Bonded_Deutschland/PDF/30-e_schleifkoerper.pdf`).*

[58] Petzow, G. *Metallographisches Ätzen.* Gebrüder Borntraeger, Berlin-Stuttgart, 5 edition, (1976).

[59] Brown, M. A. and Bulleid, C. E. *Journal of Physics E: Scientific Instruments* **11**(5), 429 (1978).

[60] Ekin, J. W. *Experimental techniques for low temperature measurements.* Oxford Univ. Press, Oxford, (2006).

[61] Harmsen, J. *Ein 4He-Verdampfer-Kryostat zur Entwicklung polarisierter Festkörpertargets.* Diploma thesis, Ruhr-Universität Bochum, (1997).

[62] Kistemaker, J. *Physica* **12**(5), 281 – 288 (1946).

[63] Oxford Instruments. *Superconducting Magnet System; Operator's Handbook*, (2011).

[64] Well Diamandrahtsägen GmbH. *Betriebsanleitung Präzisionsdrahtsäge Well Typ 3032-4.*

[65] Technical Report 614, Lake Shore Cryotronics, Inc.

[66] Tatsumoto, E. and Okamoto, T. *Journal of the Physical Society of Japan* **14**(11), 1588–1594 (1959).

[67] Brandt, B. L., Liu, D. W., and Rubin, L. G. *Review of Scientific Instruments* **70**(1), 104–110 (1999).

[68] Balshaw, N. *Practical Cryogencis, An Introduction to Laboratory Cryogenics.* Oxford Instruments, (2001).

[69] Clay, J. and Maesen, F. V. D. *Physica* **15**(5-6), 467 – 480 (1949).

[70] Feynman, R. P. *Elektromagnetismus und Struktur der Materie.* Oldenbourg, München ; Wien, 3., verb. aufl. edition, (2001).

[71] Itterbeek, A. V. and Spaepen, J. *Physica* **10**(3), 173 – 184 (1943).

[72] Maryott, A. A. and Smith, E. R. *Natl. Bur. Standards Circ.* **514**(46), 2357 (1952).

[73] McCarty, R. and Arp, V. *Adv. Cryog. Eng.* **35**, 1465–1475 (1990).

[74] Köckert, C. *Thermische Ausdehnung und Langzeit-Längenrelaxation der Systeme NbTi und NbTi-D im Tieftemperaturbereich.* PhD thesis, (2001).

[75] Ahnert, K. and Abel, M. *Computer Physics Communications* **177**(10), 764 – 774 (2007).

[76] Wöller, E. Diploma thesis, Technische Universität Dresden, (1993).

[77] Kirchhoff, G. *Monatsberichte der Akademie der Wissenschaften Berlin* (March), 144 (1877).

[78] Maxwell, J. C. *A Treatise on Electricity and Magnetism.* Clarendon, Oxford, (1873).

[79] Scott, A. and Curtis, H. *Journal of Research of the National Bureau of Standards* **22** (1939).

[80] Heerens, W. C. *Journal of Physics E: Scientific Instruments* **19**(11), 897 (1986).

[81] Moon, B. C. and Sparks, C. M. *Journal of Research of the National Bureau of Standards* **41**(November), 497–507 (1948).

[82] Johansen, T. H., Feder, J., and Jøssang, T. *Review of Scientific Instruments* **57**(6), 1168 (1986).

[83] Meingast, C., Blank, B., Bürkle, H., Obst, B., and Wolf, T. *Physical Review B* **41**(16), 299–304 (1990).

[84] Schottenhamel, W. *Weiterentwicklung und Kalibrierung eines höchstauflösenden Dilatometers zur Messung der Magnetostriktion.* Diploma thesis, Hochschule Mittweida, University of Applied Sciences, Dresden, (2010).

[85] Mate, C., McClelland, G., Erlandsson, R., and Chiang, S. *Physical Review Letters* **59**(17), 1942–1946 (1987).

[86] Müller, H. private communication, (2012).

[87] Meyberg, K. *Differentialgleichungen, Funktionentheorie, Fourier-Analysis, Variationsrechnung.* Springer, Berlin ; Heidelberg ; New York, 4 edition, (2006).

[88] Furukawa, G. T., Saba, W. G., and Reilly, M. L. Technical report, Institute for Basic Standards, National Bureau of Standards, Washington, DC, (1968). National Standard Reference Data Series- National Bureau of Standards 18, Category 5.

[89] Smith, D. and Fickett, F. *Journal of Research of the National Institute of Standards and Technology* **100**(2), 119 March (1995).

[90] Ho, C. Y., Powell, R. W., and Liley, P. E. *Journal of Physical and Chemical Reference Data* **1**(2), 279–421 (1972).

[91] Startsev, V. *Czechoslovak Journal of Physics B* **31**, 115–124 (1981).

[92] Reed, R., Simon, N., and Walsh, R. *Materials Science and Engineering: A* **147**(1), 23 – 32 (1991).

[93] Demtröder, W. *Experimentalphysik 2.* Springer-Lehrbuch. Springer-Verlag, Berlin, Heidelberg, 4 edition, (2006).

[94] Shoenberg, D. and Watts, B. R. *Philosophical Magazine* **15**(138), 1275–1288 (1967).

[95] Hahn, T. a. *Journal of Applied Physics* **41**(13), 5096 (1970).

[96] Tarascon, J. M. and Armand, M. *Nature* **414**(6861), 359–367 November (2001).

[97] Kornev, I., Bichurin, M., Rivera, J.-P., Gentil, S., Schmid, H., Jansen, A. G. M., and Wyder, P. *Phys. Rev. B* **62**, 12247–12253 Nov (2000).

[98] Zaghib, K., Mauger, a., and Julien, C. M. *Journal of Solid State Electrochemistry* **16**(3), 835–845 January (2012).

[99] Wang, D., Buqa, H., Crouzet, M., Deghenghi, G., Drezen, T., Exnar, I., Kwon, N.-H., Miners, J. H., Poletto, L., and Grätzel, M. *Journal of Power Sources* **189**(1), 624–628 April (2009).

[100] Nan, C.-W., Bichurin, M. I., Dong, S., Viehland, D., and Srinivasan, G. *Journal of Applied Physics* **103**(3), 031101 (2008).

[101] Wang, K., Maljuk, A., Blum, C., Kolb, T., Jähne, C., Meyer, H.-P., Wurmehl, S., and Klingeler, R. In Preparation, (2012).

[102] Li, J., Tian, W., Chen, Y., Zarestky, J., Lynn, J., and Vaknin, D. *Physical Review B* **79**(14), 144410 April (2009).

[103] Li, J., Garlea, V. O., Zarestky, J. L., and Vaknin, D. *Phys. Rev. B* **73**, 024410 Jan (2006).

[104] Vaknin, D., Zarestky, J. L., Rivera, J.-P., and Schmid, H. *Phys. Rev. Lett.* **92**, 207201 May (2004).

[105] Jensen, T., Christensen, N., Kenzelmann, M., Rø nnow, H., Niedermayer, C., Andersen, N., Lefmann, K., Schefer, J., v. Zimmermann, M., Li, J., Zarestky, J., and Vaknin, D. *Physical Review B* **79**(9), 092412 March (2009).

[106] Van Aken, B. B., Rivera, J.-P., Schmid, H., and Fiebig, M. *Nature* **449**(7163), 702–705 October (2007).

[107] Rabe, K. M. *Nature* **449**, 674–675 (2007).

[108] Li, J., Yao, W., Martin, S., and Vaknin, D. *Solid State Ionics* **179**(35-36), 2016 – 2019 (2008).

[109] Tian, W., Li, J., Lynn, J., Zarestky, J., and Vaknin, D. *Physical Review B* **78**(18), 184429 November (2008).

[110] Sazonov, A., Meven, M., Hutanu, V., Kaiser, V., Heger, G., Trots, D., and Merz, M. *Acta Crystallographica Section B* **64**(6), 661–668 Dec (2008).

[111] Fisher, M. E. *Philosophical Magazine* **7**(82), 1731–1743 (1962).

[112] Szewczyk, a., Gutowska, M., Wieckowski, J., Wisniewski, a., Puzniak, R., Diduszko, R., Kharchenko, Y., Kharchenko, M., and Schmid, H. *Physical Review B* **84**(10), 104419 September (2011).

[113] Onsager, L. *Phys. Rev.* **65**, 117–149 Feb (1944).

[114] Stanley, H. E. *Introduction to phase transitions and critical phenomena.* The international series of monographs on physics. Clarendon Press, Oxford, (1971).

[115] Kamihara, Y., Watanabe, T., Hirano, M., and Hosono, H. *Journal of the American Chemical Society* **130**(11), 3296–3297 (2008).

[116] Grant, P. M. *Nature* **453**(7198), 1000–1 June (2008).

[117] Wang, C., Li, L., Chi, S., Zhu, Z., Ren, Z., Li, Y., Wang, Y., Lin, X., Luo, Y., Jiang, S., Xu, X., Cao, G., and Xu, Z. *EPL (Europhysics Letters)* **83**(6), 67006 (2008).

[118] Johnston, D. C. *Advances in Physics* **59**(6), 803–1061 November (2010).

[119] Ishida, K., Nakai, Y., and Hosono, H. *Journal of the Physical Society of Japan* **78**(6), 062001 June (2009).

[120] Wen, H.-H. and Li, S. *Annual Review of Condensed Matter Physics* **2**, 121–140 March (2011).

[121] Luetkens, H., Klauss, H.-H., Kraken, M., Litterst, F. J., Dellmann, T., Klingeler, R., Hess, C., Khasanov, R., Amato, a., Baines, C., Kosmala, M., Schumann, O. J., Braden, M., Hamann-Borrero, J., Leps, N., Kondrat, a., Behr, G., Werner, J., and Büchner, B. *Nature materials* **8**(4), 305–9 April (2009).

[122] Paglione, J. and Greene, R. L. *Nature Physics* **6**(9), 645–658 August (2010).

[123] Chandra, P., Coleman, P., and Larkin, A. *Physical review letters* **64**(1), 88–91 (1990).

[124] Fernandes, R., VanBebber, L., Bhattacharya, S., Chandra, P., Keppens, V., Mandrus, D., McGuire, M., Sales, B., Sefat, a., and Schmalian, J. *Physical Review Letters* **105**(15), 1–4 October (2010).

[125] Han, M. J. and Savrasov, S. Y. *Phys. Rev. Lett.* **103**, 067001 Aug (2009).

[126] Alireza, P. L., Ko, Y. T. C., Gillett, J., Petrone, C. M., Cole, J. M., Lonzarich, G. G., and Sebastian, S. E. *Journal of Physics: Condensed Matter* **21**(1), 012208 (2009).

[127] Jiang, S., Xing, H., Xuan, G., Wang, C., Ren, Z., Feng, C., Dai, J., Xu, Z., and Cao, G. *Journal of Physics: Condensed Matter* **21**(38), 382203 (2009).

[128] Chen, H., Ren, Y., Qiu, Y., Bao, W., Liu, R. H., Wu, G., Wu, T., Xie, Y. L., Wang, X. F., Huang, Q., and Chen, X. H. *EPL (Europhysics Letters)* **85**(1), 17006 (2009).

[129] Park, J. T., Inosov, D. S., Niedermayer, C., Sun, G. L., Haug, D., Christensen, N. B., Dinnebier, R., Boris, a. V., Drew, a. J., Schulz, L., Shapoval, T., Wolff, U., Neu, V., Yang, X., Lin, C. T., Keimer, B., and Hinkov, V. *Physical Review Letters* **102**(11), 117006 March (2009).

[130] Li, Z., Zhou, R., Liu, Y., Sun, D. L., Yang, J., Lin, C. T., and Zheng, G.-q. *Phys. Rev. B* **86**, 180501 Nov (2012).

[131] Steglich, F., Aarts, J., Bredl, C. D., Lieke, W., Meschede, D., Franz, W., and Schäfer, H. *Phys. Rev. Lett.* **43**, 1892–1896 Dec (1979).

[132] Boeri, L., Calandra, M., Mazin, I. I., Dolgov, O. V., and Mauri, F. *Phys. Rev. B* **82**, 020506 Jul (2010).

[133] Liu, R. H., Wu, T., Wu, G., Chen, H., Wang, X. F., Xie, Y. L., Ying, J. J., Yan, Y. J., Li, Q. J., Shi, B. C., Chu, W. S., Wu, Z. Y., and Chen, X. H. *Nature* **459**(7243), 64–7 May (2009).

[134] Moriya, T. and Ueda, K. *Reports on Progress in Physics* **66**(8), 1299 (2003).

[135] Maeter, H., Borrero, J. E. H., Goltz, T., Spehling, J., Kwadrin, A., Kondrat, A., Veyrat, L., Lang, G., Grafe, H.-J., Hess, C., Behr, G., Büchner, B., Luetkens, H., Baines, C., Amato, A., Leps, N., Klingeler, R., Feyerherm, R., Argyriou, D., and Klauss, H.-H. *Arxiv preprint (`http://arxiv.org/abs/1210.6959`)* October (2012).

[136] Jesche, a., Krellner, C., de Souza, M., Lang, M., and Geibel, C. *New Journal of Physics* **11**(10), 103050 October (2009).

[137] Jesche, A., Krellner, C., de Souza, M., Lang, M., and Geibel, C. *Phys. Rev. B* **81**, 134525 Apr (2010).

[138] Zocco, D. A., Baumbach, R. E., Hamlin, J. J., Janoschek, M., Lum, I. K., McGuire, M. A., Sefat, A. S., Sales, B. C., Jin, R., Mandrus, D., Jeffries, J. R., Weir, S. T., Vohra, Y. K., and Maple, M. B. *Phys. Rev. B* **83**, 094528 Mar (2011).

[139] Maeter, H., (2012). private communication.

[140] Swenson, C., Roberts, R., and White, G. *Thermophysical Properties of Some Key Solids*. CODATA Bulletin 59. Oxford Pergamon Press, (1985).

[141] Corruccini, R. J. and Gniewek, J. J. *Thermal Expansion of technical Solids at Low Temperatures*. US Government Printing Office, Washington, DC, (1961).

10 Danksagung

≫Wissenschaft wird von Menschen gemacht. Dieser an sich selbstverständliche Sachverhalt gerät leicht in Vergessenheit[...]≪

— Werner Heisenberg, *Der Teil und das Ganze*

Hier möchte ich allen danken, die mich unterstützt haben und zum Gelingen dieser Arbeit beigetragen haben.

Vielen Dank an Prof. Rüdiger Klingeler für das Ermöglichen dieser Arbeit. Danke für die freundliche Aufnahme in die Arbeitsgruppe, die aktive Unterstützung während der Arbeit und die open-door-policy, immer für Fragen da zu sein.

Ebenfalls bedanke ich mich bei Prof. Christian Enss für die Zweitkorrektur.

Für die Unterstützung beim Start der Arbeit und die Versorgung mit Eis und Kaffee möchte ich mich bei Norman Leps bedanken.

Thanks to Changhyun Koo for lots of interesting discussions during helium refilling and for sharing his knowledge about cryogenics.

Ein ganz herzliches Danke an Herbert Müller für die vielen ausführlichen E-Mails, die engagierte Hilfe bei technischen Problemen und das unkomplizierte Ermöglichen des Aufenthalts an der TU Wien.

Ebenso möchte ich mich bei Wolf Schottenhamel, Wolfram Lorenz und Martin Rotter für die Unterstützung per Telefon und E-Mail bedanken.

Vielen Dank an Frau Schwöbel und Frau Müller für die Organisation von Dienstreisen und die freundliche Hilfe bei Verwaltungsdingen.

Dank geht auch an Herrn Wallenwein für die Hilfe beim Ausstatten der Labore. Ebenso danke ich auch Frau Brinkmann für das Besorgen diverser Utensilien für die Büros.

Danke an meine Bürokollegen Andreas Reifenberger und Patrick Vogt für die vielen interessanten physikalischen und nicht-physikalischen Diskussionen und die Unterstützung im gemeinsamen Kampf mit den Programmen Latex, Origin und Mathematica.

Für den reibungslosen Ablauf bei der Kryoflüssigkeitsversorgung, technische Unterstützung und das Bearbeiten von zeitweise doch sehr kurzfristigen Heliumbestellungen möchte ich mich bei Rudolf Eitel und Andreas Reiser bedanken.

Ohne die Präzision der Feinmechanikwerkstatt wäre diese Arbeit nicht möglich gewesen. Vielen Dank an das komplette Team für das Fertigen mehrerer Teile und das schnelle Bearbeiten von "Also es wäre nicht schlecht, wenn das heute noch ginge"-Aufträgen.

Ebenso hätte diese Arbeit ohne die IT-Infrastukur am KIP nicht gedruckt werden können. Vielen Dank an das EDV-Team für die technische Unterstützung.

Danke an die Elektronikwerkstatt für technischen Rat, präzises Löten und das Verkabeln der Vakuumpumpe.

Thanks to Geoffrey Tan for helping out during helium refilling and for psychological support in the late-night battle with the diamond saw wire.

Vielen Dank an die F25ler Carsten Jähne, Christoph Neef, Romeo Racz, Thomas Kolb und Kunpeng Wang für aufmunternde Worte, die Zusammenarbeit im Team und diverse kulinarische Höchstleistungen.

Ebenso geht ein Dank an Alexander Ottmann für die Unterstützung zu später Stunde während der gemeinsamen Schreibphase und das geduldige Erklären der Randeinstellungen von Latex.

Für die Unterstützung während der Arbeit und im Leben außerhalb des Neuenheimer Felds danke ich meinen Freunden Fabian Bock, Andrea Bergschneider, Simon Faller, Nadine Förster, Andreas Korzowski, Michael Lohse, Simon Murmann und Sarah Sackmann. Ein ganz besonderes Dankeschön an Thomas Nikodem für die Wochenendsessions, wenn mal ein Vortrag probegehört oder ein kniffliger Sachverhalt diskutiert werden musste. Danke für das Sicherstellen der Nahrungsversorgung per Auto am Wochenende.

Danke an meine Schwester Anna und meinen Bruder Jan-Philipp für unterstützende Worte während der Arbeit.

Vielen Dank an meine Eltern für das Wegweisen im Leben und das Senden von Versorgungspaketen, auch wenn die deutsche Post es uns nicht immer einfach machte.